Study of Differential Diffusion Effects in Lean, Premixed, Hydrogen-Enriched Low-Swirl Flames

Benjamin Francolini

Jeffrey Bergthorson

Gilles Bourque
Patrizio Vena

Master of Engineering
Department of Mechanical Engineering

McGill University

Montréal, Québec

April 2, 2023

This thesis is submitted to McGill University in partial fulfillment of the requirements for the degree of Masters of Science

Contents

List of Figures

List of Tables

I Contribution of Author

The work undertaken in this project is presented as a traditional monograph style thesis. The design and manufacture of a fully-controllable low-swirl burner complete with a turbulence generating plate, low-swirl injector and tangential feed block system is the contribution of the author. The design phase to generate low-swirl injector prototypes through additive manufacturing was undertaken with the use of a 3-D printer in plastic material, provided by Julien Lambert, a PhD colleague at the Alternative Fuels Laboratory at McGill University. The 3-D metal printing of the low-swirl injector was undertaken through correspondence with Satish Kumar Tumulu of Prof. Mathieu Brochu's research group at McGill University. All burner components were machined on-site through McGill's machine shop services. The "top-hat" burner mount depicted in Figure 6 and 10 was manufactured by the machine shop service located at the National Research Council of Canada.

MATLAB algorithms used to derive data from simultaneous OH/CH_2O-PLIF and stereo PIV techniques including, but not limited to: 1) CH_2O-OH image registration, 2) image correction by normalization of laser energy/profile, background signal, etc. and 3) autocorrelation function for estimation of integral length scale have been developed by Dr. Qiang An (now an assistant researcher at Beihang University in Beijing) and Dr. Patrizio Vena of the National Research Council of Canada. An additional MATLAB algorithm used to denoise background signal generated from camera reflection has also been provided to the author and has been developed by Dr. Luming Fan of the National Research Council of Canada.

MATLAB algorithms used to calculate instantaneous local flame statistics such as 1) instantaneous flame location from tracking of Mie scattering tomographic images, 2) the local flame displacement speed encompassing both S_{u} and S_{F} components and 3) local flame stretch rate have been developed by Dr. Ehsan Abbasi-Atibeh (former PhD student at McGill University now professor at University of Alberta), and have been provided to the author.

Experimental work from McGill and the National Research Council of Canada including the design of experiments, the laboratory setup to employ high-speed 2-D PIV techniques (including burner assembly and flow schematic for fuel-air delivery from mass flow controllers), the diagnostics calibration, testing, initial and final results analyses & uncertainty quantification presented in this thesis are the contribution of the author. All written work has been completed by the author and revised by the author's supervisors: Prof. Jeffrey Bergthorson of McGill University, Dr. Gilles Bourque, combustion key expert of Siemens Energy and Dr. Patrizio Vena, research officer at the National Research Council of Canada.

II Acknowledgments

The work in this thesis would not have been possible without the guidance (and patience) of my supervisors throughout every step of this project.

I extend my deepest gratitude to Prof. Jeffrey Bergthorson for giving me the opportunity to study combustion within the AFL group, where I not only developed the skills required of a graduate student, but also developed an appreciation for the resilience required for research. Your insightful feedback and instruction has been instrumental to the success of this project and I am thankful I had the chance to work under your tutelage.

I am also indebted to Dr. Patrizio Vena for his mentorship during my stage at the National Research Council of Canada. It was a big step to move to Ottawa (even if only for a few months), but your support along with the rest of the NRC team has helped immensely in fostering a positive work environment.

A special thank you goes to Dr. Gilles Bourque for continuously highlighting important topics and advances made in the field of combustion that broadened my general knowledge and whose considerable expertise helped guide my thesis research progress.

Furthermore, I would like to extend my gratitude to my Alternative Fuels Laboratory colleagues, particularly to Antoine Durocher and Marie Meulemans who inspire me by their level of critical thinking, to Julien Lambert whose no-quit attitude in spite of challenges prompted me early on to do the same and to Ehsan Abbasi-Atibeh, who encouraged me in my research objectives from the start.

Lastly, a heartfelt thank you goes to my best friends, Stanley and Adamo, my sister, Sabrina, my parents, Peter and Maria and my wonderful girlfriend, Emily for their unwavering support and encouragement throughout this project, for which I will always cherish.

I would also like to acknowledge the financial support provided by the Réseau Québécois sur l'Énergie Intelligente, the Fonds de Recherche du Québec and by stipend through the Natural Sciences and Engineering Research Council of Canada Alliance grant in supplementing this thesis project.

III Abstract

Climate change is and will continue being the largest problem affecting humanity if our reliance on fossil fuel combustion is not significantly curbed by 2050. Currently, our global energy framework still depends greatly on finite resources such as coal, natural gas and oil throughout the transport, residential and industrial sectors. Nevertheless, fossil fuel combustion is the primary contributor of greenhouse gas emissions (GHGs) such as carbon dioxide (CO_2) largely responsible for the unsustainable warming of our planet. Therefore, the primary goal is to invest in greener fuels capable of meeting global energy demand and to investigate green solutions feasible with our current technological capabilities.

Hydrogen combustion is a promising solution in reducing our carbon footprint because its combustion produces zero carbon emissions. Hydrogen fuel also has a larger specific energy than conventional fossil fuels and is realizable in industrial sectors dedicated to power generation such as gas turbine power plants. Although the substitution of natural gas for hydrogen in existing gas turbines is gaining traction in the context of fuel flexibility, the main challenges are that hydrogen fuel is highly reactive and highly diffusive, which largely influences flame behaviour and flame stability. At fuel-lean conditions, hydrogen's mass diffusivity is larger than its thermal diffusivity, which means such flames are susceptible to differential diffusion effects largely responsible for the thermodiffusive instabilities that pose risks to gas turbines. Therefore, it is necessary to characterize how differential diffusion influences hydrogen flames in the hopes of mitigating combustion instabilities further.

This thesis investigates hydrogen-enrichment in lean, premixed methane flames to study the onset of differential diffusion. In order to isolate differential diffusion effects from turbulent-flame interactions, the bulk velocity ($\overline{U}$) and the laminar flame speed (S_{L}) were held constant at $\overline{U} = 13$ m/s and $S_{\mathrm{L}} = 0.267$ m/s respectively for each evaluated fuel blend of methane and hydrogen between 0% - 80% H_2 volume fraction (% vol.). Furthermore, this study was conducted in a swirl burner comparable to existing gas turbine configurations in order to utilize the low-swirl flame's aerodynamics in maintaining a constant turbulent flow field for each condition. The additive manufacturing of 3-D printed, swirl injector prototypes was also undertaken to rapidly validate burner geometries to the conditions needing to be evaluated. For each condition, an analysis on the local instantaneous flame statistics was conducted using high-speed particle image velocimetry (PIV) to highlight trends explained by differential diffusion from time-resolved images of turbulent flames. Furthermore, a subsequent analysis on flame topology was performed for the same conditions using simultaneous stereoscopic PIV and OH/CH_2O planar laser-induced fluorescence (PLIF) to assess the stability mechanisms behind differential diffusion in mixtures with high hydrogen

content. The results from both experimental campaigns in this thesis complement each other well with low-swirl flame theory such that increase in flame displacement observed is effectively correlated to an increase in the turbulent flame speed. Therefore, differential diffusion is a considerable phenomenon influencing the turbulent burning rate in swirling flames, becoming most apparent for Le < 0.73 (i.e., $> 40\%$ vol. H_2). The findings in this thesis are important for hydrogen flame characterization for two reasons: 1) to develop reliable, fuel-flexible industrial burners and 2) to improve the existing hydrogen-based thermochemical models used to design them.

IV Résumé

Le changement climatique restera le plus grand problème de l'humanité si notre dépendance sur les combustibles fossiles n'est pas considérablement réduite d'ici 2050. Présentement, notre cadre énergétique mondial dépend encore largement de ressources finies telles que le charbon, le gaz naturel et le pétrole dans les secteurs du transport, du résidentiel et de l'industrie. Néanmoins, la combustion de combustibles fossiles est le principal responsable des émissions de gaz à effet de serre (GES), comme le dioxyde de carbone (CO_2), liés au réchauffement insoutenable de notre planète. Par conséquent, l'objectif premier est d'investir dans des combustibles plus verts capables de répondre à la demande énergétique mondiale et d'étudier des solutions vertes réalisables avec nos capacités technologiques actuelles.

L'hydrogène est une solution prometteuse pour réduire notre empreinte carbone, car sa combustion produit n'émet pas d'émissions de carbone. L'hydrogène a également une énergie spécifique supérieure à celle des combustibles fossiles et peut être utilisé dans les secteurs industriels dédiés à la production d'électricité, comme les centrales à turbine à gaz. Bien que le remplacement du gaz naturel par l'hydrogène gagne du terrain dans le contexte des carburants durables, les principaux défis sont que le carburant hydrogène est très réactif et très diffus, ce qui influence largement le comportement et la stabilité de la flamme. Avec les conditions à mélange pauvre, la diffusivité de masse de l'hydrogène est plus grande que sa diffusivité thermique, dont ces flammes sont plus sensibles aux effets de la diffusion différentielle responsables pour les instabilités de combustion. Donc, il est nécessaire de caractériser comment la diffusion différentielle influence les flammes d'hydrogène dans l'espoir d'atténuer davantage les instabilités de combustion.

Cette thèse étudie l'enrichissement en hydrogène dans des flammes de méthane pauvres et prémélangées afin d'étudier le début de la diffusion différentielle. Afin d'isoler les effets de la diffusion différentielle contre les interactions turbulentes de la flamme, la vitesse globale et la vitesse de la flamme laminaire ont été maintenues constantes pour chaque mélange de méthane et d'hydrogène évalué entre 0% - 80% de fraction volumique de H_2 (% vol.). En plus, cette étude a été menée dans un brûleur à tourbillon comparable aux configurations existantes des turbines à gaz afin d'utiliser l'aérodynamisme de la flamme à faible tourbillon pour maintenir un niveau de turbulence constant pour chaque condition. La fabrication additive de prototypes d'injecteurs a également été entreprise pour valider rapidement les géométries des brûleurs en fonction des conditions à évaluer. Pour chaque condition, une analyse des statistiques locales instantanées de la flamme a été réalisée à l'aide de la vélocimétrie par image de particules (PIV) afin de mettre en évidence les tendances expliquées par la diffusion différentielle. En outre, une analyse ultérieure a été réalisée pour les mêmes conditions

en utilisant simultanément la PIV stéréoscopique et la fluorescence planaire induite par laser (PLIF) pour évaluer les mécanismes de stabilité derrière la diffusion différentielle. Les résultats de cette thèse se complètent bien avec la théorie des flammes à faible tourbillonnement de sorte que l'augmentation du déplacement de la flamme observée est effectivement corrélée à une augmentation de la vitesse turbulente de la flamme. Les résultats de cette thèse sont importants pour la caractérisation des flammes d'hydrogène pour deux raisons : 1) pour développer des brûleurs fiables envers des carburants durables et 2) pour améliorer les modèles thermochimiques utilisés pour les concevoir.

V Nomenclature

Notation

a_z	Normalized axial divergence rate	mm^{-1}
A_a	Area of annular channel in LSB	m^2
A_c	Area of central channel in LSB	m^2
A_L	Laminar flame surface area	m^2
A_T	Turbulent flame surface area	m^2
c_R	Reaction progress variable	
$\overline{c}_\mathrm{R}$	Mean reaction progress variable	
c_T	Temperature progress variable	
$\overline{c}_\mathrm{T}$	Mean temperature progress variable	
c_p	Specific heat capacity at constant pressure	$\mathrm{kJ/(kg{\cdot}K)}$
C	PIV spatial resolution	mm/pixel
$\mathrm{C_{KW}}$	Knudsen-Weber slip-correction factor	
C_d	Drag coefficient	
D	Diameter	mm
$\mathcal{D}$	Diffusivity of the deficient reactant	m^2/s
$\mathrm{Da_T}$	Turbulent Damköhler number	
E	Oil droplet evaporation constant	
F	Force	N
G_ang	Axial component of angular momentum in swirling flow	$\mathrm{kg{\cdot}m}^2/\mathrm{s}$
G_x	Axial component of linear momentum in swirling flow	$\mathrm{kg{\cdot}m}^2/\mathrm{s}$
h_v	Specific enthalpy of vaporization	kJ/kg
k	Azimuthal coordinate (out-of-plane)	
K	Flame stretch rate	s^{-1}
$\langle K \rangle$	Mean flame stretch rate	s^{-1}
K_s	Hydrodynamic strain rate	s^{-1}
$K_\mathrm{s,a}$	Local hydrodynamic axial strain rate	s^{-1}
$\langle K_\mathrm{s,a} \rangle$	Mean hydrodynamic axial strain rate	s^{-1}
$K_\mathrm{s,t}$	Local hydrodynamic tangential strain rate	s^{-1}
$\langle K_\mathrm{s,t} \rangle$	Mean hydrodynamic tangential strain rate	s^{-1}
$\mathrm{Ka_T}$	Turbulent Karlovitz number	
l_evap	Uncertainty in flamefront tracking due to droplet evaporation	mm
$l_\mathrm{Filt.}$	Uncertainty in flamefront tracking due to post-processing	mm
l_I	Uncertainty in flamefront tracking due to oversaturation	mm

l_{p}	Uncertainty in flamefront tracking due to mean tracer particle distance	mm
l_{Tot}.	Total uncertainty in flamefront tracking	
$\mathcal{L}$	Markstein length	m
Le	Lewis number	
$\mathrm{Le}_{\mathrm{eff}}$	Volume-based effective Lewis number	
m	Mass flux ratio	
MW	Molecular weight	kg/kmol
n	Normal direction to flame surface	
P	Pressure	kPa
r	Radial coordinate	
R	Radius	mm
R_{mix}	Specific gas constant of mixture	J/kg·K
R_{b}	Swirl burner radius	mm
R_{c}	Swirl burner centerbody radius	mm
Re_{T}	Turbulent Reynolds number	
$R_{\mathrm{uu}}(r)$	Transverse autocorrelation function in the radial direction	
S	Swirl number	
S_{crit}	Critical swirl number between low- and high-swirling flow	
St	Stokes number	
S_{F}	Local flamelet velocity in the flow coordinate system	m/s
S_{L}	Stretched laminar flame speed	m/s
S_{L}^{o}	Unstretched laminar flame speed	m/s
S_{u}	Convective velocity of the flow upstream of the flamefront	m/s
S_{T}	Local flame displacement velocity, or turbulent flame speed	m/s
$\langle S_{\mathrm{T}} \rangle$	Mean flame displacement velocity	m/s
$S_{\mathrm{T,LC}}$	Turbulent burning rate or local consumption velocity	m/s
$\langle S_{\mathrm{T,LC}} \rangle$	Mean turbulent burning rate	m/s
$S_{\mathrm{T-LE}}$	Local flame displacement velocity at leading point	m/s
t	Time coordinate	
T_{amb}	Ambient room temperature	K
T_{ad}	Adiabatic flame temperature	K
T_{b}	Flame temperature	K
T_{s}	Flash-point temperature of seeding oil	K
T_{u}	Unburned reactant temperature	K
u	Instantaneous velocity in the axial direction	m/s

u_{a}	Axial velocity through outer plenum of LSB	m/s
u_{c}	Axial velocity through inner plenum of LSB	m/s
u_{f}	Fluid velocity	m/s
u_{p}	Particle velocity	m/s
u'	Instantaneous velocity fluctuation in the axial direction	m/s
$u_{\mathrm{RMS}}/\overline{U}$	Turbulence intensity normalized by local mean axial velocity	
$u_{\mathrm{RMS}}/S_{\mathrm{L}}$	Turbulence intensity normalized by laminar flame speed	
$\overline{U}$	Mean flow velocity in axial direction	m/s
U_{av}	Bulk velocity	m/s
u_{RMS}	RMS velocity	m/s
$u_{\mathrm{RMS\text{-}3C}}$	Three-component RMS velocity	m/s
v	Instantaneous velocity in the radial direction	m/s
$\overline{V}$	Mean velocity in the radial direction	m/s
v'	Instantaneous velocity fluctuation in the radial direction	m/s
w	Instantaneous velocity in the azimuthal direction	m/s
w'	Instantaneous velocity fluctuation in the normal direction	m/s
$\overline{W}$	Mean flow velocity in the azimuthal direction	m/s
X	Mole fraction	
z	Axial coordinate	
Z_{f}	Local flame front location	mm
$\langle Z_{\mathrm{f}} \rangle$	Mean flame front location	mm
α	Thermal diffusivity	m^2/s
δ_{L}	Diffusive laminar flame thickness	mm
δ_{T}	Turbulent flame thickness	mm
ϵ	Energy dissipation rate per unit mass	$\mathrm{m}^2/\mathrm{s}^3$
η	Kolmogorov length scale	mm
θ	Vane angle	$^{\mathrm{o}}$
κ	Flame front curvature	mm^{-1}
$\langle \kappa \rangle$	Mean flame front curvature	mm^{-1}
$\langle \lvert\kappa\rvert \rangle$	Mean absolute flame front curvature	mm^{-1}
λ	Thermal conductivity	W/(m·K)
Λ	Integral length scale	mm
μ	Dynamic viscosity	kg/(m·s)
ν	Kinematic viscosity	m^2/s
ω	Angular velocity	rad/s

ρ	Density	$\mathrm{kg/m^3}$
σ	Uniform velocity gradient	$\mathrm{s^{-1}}$
Σ	Flame surface area enhancement $A_\mathrm{T}/A_\mathrm{L}$	
$\langle\Sigma\rangle$	Mean flame surface area enhancement	
τ_chem	Chemical time scale	ms
$\tau_\mathrm{evap.}$	Evaporation time scale	ms
τ_η	Kolmogorov time scale	ms
τ_res	Combustion residence time scale	ms
τ_s	Stokes time scale	ms
ϕ	Equivalence ratio	

Acronyms

2D	Two-dimensional
3D	Three-dimensional
3C	Three-component
AFL	The Alternative Fuels Laboratory
BPTRZ	Broadened preheat thin reaction zone
CDZ	Central divergence zone
CFD	Computational fluid dynamics
CMOS	Complementary metal-oxide semiconductor
CRZ	Central recirculation zone
DL	Darrieus-Landau
DLE	Dry, low-emission combustion
DNS	Direct numerical simulations
FOV	Field-of-view
FSA	Flame surface area
FSD	Flame surface density
GHG	Greenhouse gases
HRR	Heat release rate
ICCD	Intensified charged-couple device
LCOE	Levelized cost of electricity
LES	Large-eddy simulation
LSB	Low-swirl burner
LSI	Low-swirl injector
MFC	Mass flow controller
Nd:YAG	Neodymium-doped yttrium aluminum garnet
Nd:YLF	Neodymium-doped ytrrium lithium fluoride
NRC	National Research Council of Canada
PD	Normalized probability distribution
PIV	Particle image velocimetry
PLIF	Planar laser-induced fluorescence
PTU	Programmable timing unit
RMS	Root-mean-square
RQL	Rich-quench-lean combustion
S-PIV	Stereoscopic particle image velocimetry
TGP	Turbulence generating plate

1 Introduction & Background

1.1 Transition to green fuels

Anthropogenic-driven climate change remains the largest problem facing humanity today and the primary reason is due to our continual dependence on fossil fuel combustion. Currently, fossil fuels (i.e. coal, gas and petroleum) remain the energy resources dominating how we live and how we move [1][2]. Nevertheless, fossil fuels are also hydrocarbons whose combustion emits carbon dioxide (CO_2) to the Earth's atmosphere among other harmful products, all of which pose significant risks to human health and Earth's ecosystems. The accelerated global warming from increasing CO_2 levels continues to prompt countries worldwide towards mitigating climate change under the Paris agreement, in an effort to reduce the long-term impacts from fossil fuel combustion on the planet's ecosystems. As such, targets have been legislated across many countries to reduce emissions levels in order to keep global warming within 1.5 - 2 ^{o}C from pre-industrial revolution through to 2050 [3]. Nevertheless, one of the most significant challenges is transitioning away from fossil fuels for greener, sustainable solutions while simultaneously meeting global energy demand.

One reason explaining why fossil fuels have persisted in supplying energy globally is that they are energy dense. Nearly all hydrocarbons, including gasoline, diesel and natural gas have an energy density (i.e. energy per unit volume) nearly an order of magnitude higher than non-conventional energy sources such as lithium batteries and compressed air storage while also having a considerably higher specific energy (i.e. energy per unit mass) [4]. Practically, this means hydrocarbons are equipped to provide the same amount of power as batteries at a fraction of the volume and weight due to their larger chemical energy potential. For instance, the investigation of metal fuels such as iron and aluminum is gaining traction since their energy density is able to rival hydrocarbons [5] while their potential recyclability [6] presents an attractive solution to the climate crisis problem. Nevertheless, there remain several technological hurdles subject to continuing research before metal fuels can be implemented industrially and scaled globally. Another reason fossil fuels currently dominate the energy market is because the resources themselves are convenient energy carriers, as they are easily transportable and easy to use in existing applications. While the increasing development of renewable energy grids dedicated to wind, solar and hydropower are viable alternatives to fossil fuels for zero-carbon power, these resources are limited by two factors: 1) inconsistent power delivery due to intermittency and 2) inaccessibility, which has highlighted a growing need to advance energy storage techniques [7]. Even if the development of renewable energy grids globally has led to declines in their levelized cost of electricity (LCOE), such resources

still need to contend with infrastructure capital costs and operating and maintenance costs (O&M) at a reduced capacity availability compared to fossil fuels [8][9]. Therefore, fossil fuel combustion will continue to remain relevant in the near future throughout the industrial, transportation and power generation sectors.

The challenges associated with continued fossil fuel combustion are that reserves are becoming increasingly finite and more importantly, their combustion is non-recyclable. As such, there is a mounting pressure to quickly transition towards a sustainable economy dependent on clean energy as a means to maintain a high standard of living [10]. The negatives that come with fossil fuel combustion in the near future provide an opportunity to support intermediate energy solutions which can be realized in practical applications. One of the more popular intermediate solutions trending in the power generation sector is hydrogen combustion in gas turbine power plants [11][12][13]. Hydrogen (H_2) is an attractive fuel since its combustion with oxygen in air produces water vapour instead of carbon emissions. Hydrogen fuel has already been implemented in fuel cells for stationary and mobile power [14] and its large specific energy is sufficient enough to meet our energy demands while being realizable for retrofit in existing applications such as power plant gas turbines. Hydrogen's potential to reduce our carbon footprint has also paved the way for fuel blends such as syngas (H_2 and carbon monoxide, CO) to become a viable alternative fuel to natural gas conventionally used in gas turbines [15][16]. Although hydrogen fuel provides realistic avenues to establish a net-zero carbon economy, it is necessary to put it into context against other energy solutions. Currently, the primary method for producing hydrogen comes from the gasification of fossil fuels, a largely carbon-intensive process for which the product is known as "grey hydrogen" [17]. Furthermore, hydrogen gas is closer in energy density to lithium-ion batteries than it is to biofuels such as ethanol and even less so to hydrocarbons. Compression and liquefaction are some of the existing methods for increasing its energy density, but the additional energy inputs required to store hydrogen for industrial applications remains a great challenge and an active area of research [18]. One option undergoing current investigation is hydrogen production from the reaction of aluminum with water at supercritical conditions [19]. Similarly to metal fuel combustion, if the aluminum oxide product can be recycled, the hydrogen gas by-product can be captured, stored and utilized on-demand in a greener manner. Hydrogen can also be produced more cleanly through water electrolysis than gasification (termed "green hydrogen"), but the energy required to do so would need to come from renewable grids to truly be considered a green process. However, given the higher cost and environmental footprint of renewable power, hydrogen production from renewable energy sources is bound to be more challenging than traditional gasification methods [20][21]. Until such renewable energy grids can be more cost competitive, there is still significant need to study

hydrogen's flame characteristics from an engineering perspective, particularly if hydrogen is to serve as a viable alternative fuel.

1.2 Fuel flexibility and combustion instabilities

Presently, there is an increasing investment towards developing and retrofitting combustors capable of handling hydrogen, particularly in stationary gas turbines. However, the challenge with tuning gas turbines to higher hydrogen-content fuel blends comes from an enhanced reactivity and diffusivity [22][23] compared to conventional fossil fuels, particularly given the nonlinear propagation behaviour exhibited in flames with hydrogen enrichment [24]. Gas turbines, which are currently tuned to natural gas ($\geq$ 90% vol. CH_4 in most regions) operate in a premixed combustion mode for several reasons: 1) to reduce soot emissions most commonly produced in non-premixed combustion as a result of poor reactant mixedness and 2) to reduce the flame temperature by lowering the equivalence ratio ϕ of the mixture (see Equation 1). As opposed to a non-premixed combustion reaction where fuel diffuses to the ambient air and burns stoichiometrically ($\phi = 1$), a premixed combustion reaction produces a flame reaction zone which propagates as a diffusion-reaction wave. This propagating wave consumes mixed fuel and oxidizer at a characteristic burning velocity known as the laminar flame speed (S_{L}), which is a function of the equivalence ratio of the mixture:

$$\phi = \frac{(F/A)_{\mathrm{actual}}}{(F/A)_{\mathrm{stoich}}} \tag{1}$$

Here, the stoichiometric fuel-to-air ratio in the denominator will be different depending on the fuel in the reaction (e.g. 0.042 for propane C_3H_8, 0.105 for methane CH_4 and 0.42 for hydrogen H_2). Essentially, premixed combustion enables gas turbine power plants to curb GHG and NO_x emissions, particularly when flames are operated in a fuel-lean mode ($\phi < 1$, excess oxidizer) compared to a fuel-rich mode ($\phi > 1$, excess fuel). Depending on the emissions reduction strategy, dry low emissions (DLE) combustors operate at fuel-lean conditions [25][26][27] while other gas turbines with multiple stages operate in a rich-quench-lean (RQL) mode [28]. Ultimately, there is benefit of operating in a fuel-lean mode considering combustion temperatures fall drastically with decreasing equivalence ratio [29], which is favourable towards reducing NO_x emissions which are highly dependent upon the flame temperature [30]. However, the laminar flame speed of a mixture also decreases with decreasing equivalence ratio on account of less fuel being available for reaction, which lowers the flame's burning rate and the power output generated by a gas turbine. In general, the range of laminar flame speeds, and by extension the turbulent flame speeds (S_{T}) which can be sustained in a combustor for a given mixture composition, is known as a fuel's flammability

limits and is of great interest to gas turbine engineers. For instance, the limitation on achieving lower NO_x targets is the lower flammability limit of natural gas flames before extinction occurs. In this regard, hydrogen addition is promising because a blend with natural gas can push the flammability limits lower towards achieving reasonable emissions levels without compromising power requirements [31]. In the context of fuel-flexibility, it is an advantage to expand the flammability range in the transition to low-carbon/high-hydrogen fuel blends, but there are also challenges in the form of combustion instabilities, both static and dynamic.

The challenge of operating flames at ultra-lean conditions means they are susceptible to the phenomenon which characterizes their lower flammability limit, known as flame blowoff or blowout. Flame blowoff occurs when a flame becomes unstable to the point of detaching from its anchored point, thereby extinguishing by action of "blowing out". Fundamentally, this phenomenon is observed when the chemical reaction time of a flame is longer than the combustion zone residence time, resulting in the flow velocity exceeding the flame velocity. The Damkhöler number, for instance relates these flow and flame time scales and is an important non-dimensional parameter used to depict lean blowoff limit trends in both laminar and turbulent combustion reactions:

$$\mathrm{Da} = \frac{\tau_{\mathrm{res}}}{\tau_{\mathrm{chem}}} = \frac{S_{\mathrm{L}}^2 d}{\alpha U_{\mathrm{ref}}} \tag{2}$$

Here, τ_{res} refers to the combustion zone residence time, defined by the ratio between the characteristic length and velocity scales. τ_{chem} refers to chemical kinetic time and is defined by the ratio between thermal diffusivity α and the square of the laminar flame speed S_{L}. Therefore, flame extinction will most likely occur where the Damkhöler number is low. Conversely, hydrogen addition can increase the Damkhöler number of a reacting mixture because its laminar flame speed is roughly one order of magnitude larger than most conventional fossil fuels [32], which means it can be used to stave off typical blowout trends in natural gas flames. Nevertheless, flames at fuel-lean conditions, particularly high-hydrogen content flames, can also be subjected to flashback, a result of the flame propagating upstream towards the premixed mixture where combustor components are not designed for high flame temperatures. The flame propagates upstream when the flame speed exceeds the local flow velocity, which often occurs along streamlines where velocities are lowest, most commonly along a boundary layer. Flashback may also be induced if there is an adverse pressure gradient downstream of the flame, which would slow down the flow enough to inhibit it from balancing against the flame propagation speed. Implementing hydrogen in existing combustors tuned for natural gas poses a significant challenge to combustion

engineers because hydrogen burns much faster, which means mitigating against such *static* flame instabilities becomes much more unpredictable. In the case of flashback, there is additional risk that the combustor and other related components may be damaged past the point of consistent and reliable power generation.

Practically, *dynamic* flame instabilities are also common in lean, premixed combustion systems [33]. In a confined combustor, acoustic oscillations can perturb the combustion flow field and significantly influence the stoichiometry of the combustion reaction enough to generate unsteady heat release rates [34]. According to Rayleigh's criterion [35], the in-phase coupling of unsteady heat release rates and pressure oscillations can create a positive feedback of acoustic instabilities in flames enough to cause combustor fatigue and turbine wear. Furthermore, vortex shedding is an additional concern linked to a rapid expansion in the flow between the nozzle and the combustor, causing the heat release rate to fluctuate and flame behaviour to become unpredictable. For the purpose of this thesis on hydrogen study, flames are evaluated in an unconfined configuration to reduce acoustic/vortex shedding perturbations which might induce unwanted instabilities in experiments.

Lastly, all flames, both laminar and turbulent need to contend with *hydrodynamic* instabilities. According to general fluid dynamics theory, the conservation of mass must hold such that the flow of the unburned reactants must balance the flow of burned products as the flow traverses the flame reaction zone. However, due to the rapid increase in thermal energy, the density of the burned products decreases according to the Ideal Gas Law ($P = \rho RT$), causing flow acceleration downstream of the flame. As a consequence, the density drop across the flame reaction zone produces a hydrodynamic instability known as the Darrieus-Landau (DL) mechanism. From this mechanism, a continuous, perturbed flame segment propagating at a characteristic S_{L} will cause the approach flow of unburned reactants to diverge and converge at convex and concave regions of the flame, respectively. Since the flow widens in a convex region, it ultimately slows down by conservation of mass [29]. However, the characteristic S_{L}, which is a product of the mixture's composition and boundary conditions remains unchanged, causing the convex region to propagate further into the unburned reactant mixture. Similarly, the reverse phenomenon occurs for concave regions such that the flame recedes away from the unburned mixture. However, experimental studies in turbulent premixed flames [36] have shown that normalized turbulence intensities $u'/S_L > 4$ generally shadow DL effects, which is the case from the evaluated conditions in this study. In addition, given the density of the unburned mixture is ultimately larger than the burned mixture, the flame experiences a body force driven by buoyancy if the flame is propagating upwards, known as the Rayleigh-Taylor instability [29]. However, the Rayleigh-Taylor hydrodynamic effects are negligible in this thesis given the configuration evaluated involves

flames propagating downward against an incoming flow.

1.3 Turbulent combustion and turbulent burning rate

The influence of turbulence in reacting flows adds an additional complexity towards predicting the combustion behaviour of hydrogen flames. In recent years, significant research involving computational fluid dynamics (CFD) has been undertaken to study burning rates and flame topology under turbulence while direct numerical simulations (DNS) and large-eddy simulations (LES) methods have widely been used [37][38][39] to resolve the various length and time scales of turbulence in reacting flows. Turbulence is defined by the chaotic and random nature of a flow field, producing unsteady fluctuations in velocity as a result of the formation of vortical structures known as eddies. As opposed to laminar flows which are generally orderly and predictable, the eddies present in turbulent flows are chaotic and random. As a result, the effect of turbulence play a significant role in enhancing mass, momentum and heat transport, which has significant implications on combustion phenomena. The Reynolds number is a dimensionless parameter which provides a rudimentary boundary between laminar and turbulent flows by relating the inertial forces to the viscous forces in a moving fluid:

$$\mathrm{Re} = \frac{U_{\mathrm{ref}} L}{\nu} \tag{3}$$

In the above equation, U_{ref} represents the characteristic (reference) velocity of the fluid, L represents the characteristic length scale and $\nu{=}\mu/\rho$ represents the kinematic viscosity of the fluid. Nevertheless, flow properties such as velocity, temperature and pressure are difficult to resolve in an entire turbulent flow field given that it is computationally expensive to derive solutions from the governing Navier-Stokes and energy conservation equations. A customary strategy to simplify analysis of turbulence is through a statistical approach of time-averaging the variable of interest [40]. For simplicity, velocity is chosen in the following example:

$$u(\mathbf{x}) = \overline{U}(\mathbf{x}) + u'(\mathbf{x}) \tag{4}$$

Also known as Reynold's decomposition, Eq. 4 characterizes the instantaneous velocity u as the summation of the random fluctuation of the velocity u' about the mean velocity $\overline{U}$ at any given position in 3-D space, $\mathbf{x}$. Although the average random fluctuation is equal to zero ($\overline{u'} = 0$) from a probabilistic viewpoint, the same cannot be said of the variance $\overline{u'^2}$. In the literature, the standard deviation, or root-mean-square (RMS) of the turbulent fluctuations (u_{RMS}) is an important variable in dictating the turbulence intensity for a given flow field.

Therefore, the characteristic velocity scale of the largest eddies, u'_{o} is synonymous with the square root of the variance $\overline{u'^2}$, and is important in defining the turbulent Reynolds number, $\mathrm{Re_T}$:

$$\mathrm{Re_T} = \frac{u'_{\mathrm{o}}\Lambda}{\nu} \tag{5}$$

In Eq.5, the integral length scale Λ represents the scale of the largest, energy-carrying eddies present in a flow. A transverse autocorrelation is derived between two spatial points radially in a 2-D flow:

$$R_{\mathrm{uu}}(r) = \frac{\overline{u'(z,t)u'(z+r,t)}}{\overline{u'^2}} \tag{6}$$

Here, the transverse correlation relates the radial direction r to the perpendicular component of the velocity fluctuation of a turbulent flow (i.e. the axial velocity component u). Essentially, the transverse autocorrelation is a measure of how correlated the turbulent axial velocity is with itself up to finite radial distance. From the literature, the integral of the transverse autocorrelation curve up to the first zero crossing is generally a good estimate of the integral length scale of turbulent eddies and should be comparable to the characteristic geometry of the application inducing turbulence [41]:

$$\Lambda \approx \int_0^{R_{\mathrm{uu}}(r)=0} R_{\mathrm{uu}}(r)\, du \tag{7}$$

The largest eddies are also those which carry the greatest amount of turbulent kinetic energy in a system. According to conservation of energy, the kinetic energy in the largest eddies is transferred to successively smaller eddies in an energy cascade at an energy dissipation rate ϵ proportional to $(u')^3/\Lambda$. This cascade continues until the eddies reach their smallest scale before being dissipated as heat through viscosity. The smallest scale attainable by turbulent eddies is known as the Kolmogorov scale, also known as the microscale of turbulence:

$$\tau_{\mathrm{K}} \approx \left(\frac{\nu}{\epsilon}\right)^{1/2} \tag{8}$$

Since viscous dissipation dominates at this scale, the Kolmogorov time scale becomes a function of the viscosity ν and energy dissipation rate ϵ. The disparity between the integral and Kolmogorov scales can subsequently be related through the turbulent Reynolds number such that $\Lambda/l_{\mathrm{k}} \approx \mathrm{Re_T^{3/4}}$ and $\tau_\Lambda/\tau_{\mathrm{k}} \approx \mathrm{Re_T^{1/2}}$. From this dimensional analysis, more turbulent kinetic energy (i.e. producing a larger turbulent Reynolds number) in a system will result in a longer energy cascade leading to smaller Kolmogorov eddies. In the context of turbulent

combustion, the Kolmogorov time scale along with the chemical time scale τ_{chem} become important in defining the turbulent Karlovitz number:

$$\text{Ka}_{\text{T}} = \frac{\tau_{\text{chem}}}{\tau_{\text{K}}} = \frac{1}{\text{Da}} \tag{9}$$

The Karlovitz number provides an indication of the tendency for eddies to penetrate the preheat zone layer of a turbulent flame [29]. If the Karlovitz number is large, then this signifies that Kolmogorov eddies are comparable, if not smaller than the flame's preheat and reaction zones. The Borghi diagram, refined by Peters [42] delineates the most common turbulent flame regimes bounded by the turbulent Karlovitz number (Ka_{T}) and the turbulent Reynolds number (Re_{T}) (see Figure 1). The region enclosed by the red rectangle corresponds to the flame regimes most common in gas turbines [43]. For instance, the larger turbulence intensities present in practical combustors means turbulent flames behave similarly to the Broadened Preheat Thin Reaction Zone (BPTRZ) regime, such that eddies are able to penetrate the preheat zone and enhance heat and mass transport.

In general, combustion in a turbulent flow field results in the flame front being wrinkled, which increases the flame surface area (FSA) and consequently, increases the turbulent burning rate of a mixture. The burning rate, which is strongly correlated to the turbulent flame speed S_{T} is primarily a function of the laminar flame speed S_{L} and the turbulence intensity $u_{\text{RMS}}/\overline{U}$. However, S_{L}, while largely dependent on the equivalence ratio, is also susceptible to flame stretch effects that arise from flow geometry and fuel composition. The flame stretch rate, also known as strain rate has several definitions [29]:

$$K = \frac{1}{A}\frac{dA}{dt} = \kappa S_{\text{T}} + K_{\text{s,t}} \tag{10}$$

Essentially, the flame stretch rate (s^{-1}) is the normalized differential change in FSA. The components responsible for increasing or decreasing FSA due to flame stretch can be further broken down to the following: 1) the local flame velocity S_{T}, 2) the local curvature κ and 3) the hydrodynamic tangential strain, $K_{\text{s,t}}$. Therefore, given the nature of turbulence to corrugate a flame, the rapid increase and decrease of FSA means it is very difficult to predict how fast flames burn for a given fuel, particularly hydrogen. For instance, Damkhöler's hypothesis attempts to characterize turbulent burning rate enhancement ($S_{\text{T-LC}}/S_{\text{L}}$) as proportional to the $A_{\text{T}}/A_{\text{L}}$ that comes from enhanced FSA generation. However, this theory does not leave room to interpret the effect of flame stretch on enhanced turbulent burning rates, as will be introduced in the following section. Some studies have adopted different models to better characterize the turbulent burning rate based on conditional mass flux and flame surface density [44]. In this regard, it is important to distinguish how turbulent

velocity is defined. In the literature, the displacement speed S_{T} refers to the flame velocity in a laboratory reference frame and the consumption speed $S_{\mathrm{T-LC}}$ refers to the velocity at which reactants are consumed and will be defined as such throughout this thesis. Given hydrogen's larger diffusivity compared to conventional hydrocarbons, flame stretch plays a significant role in how fast burning occurs due to differential diffusion.

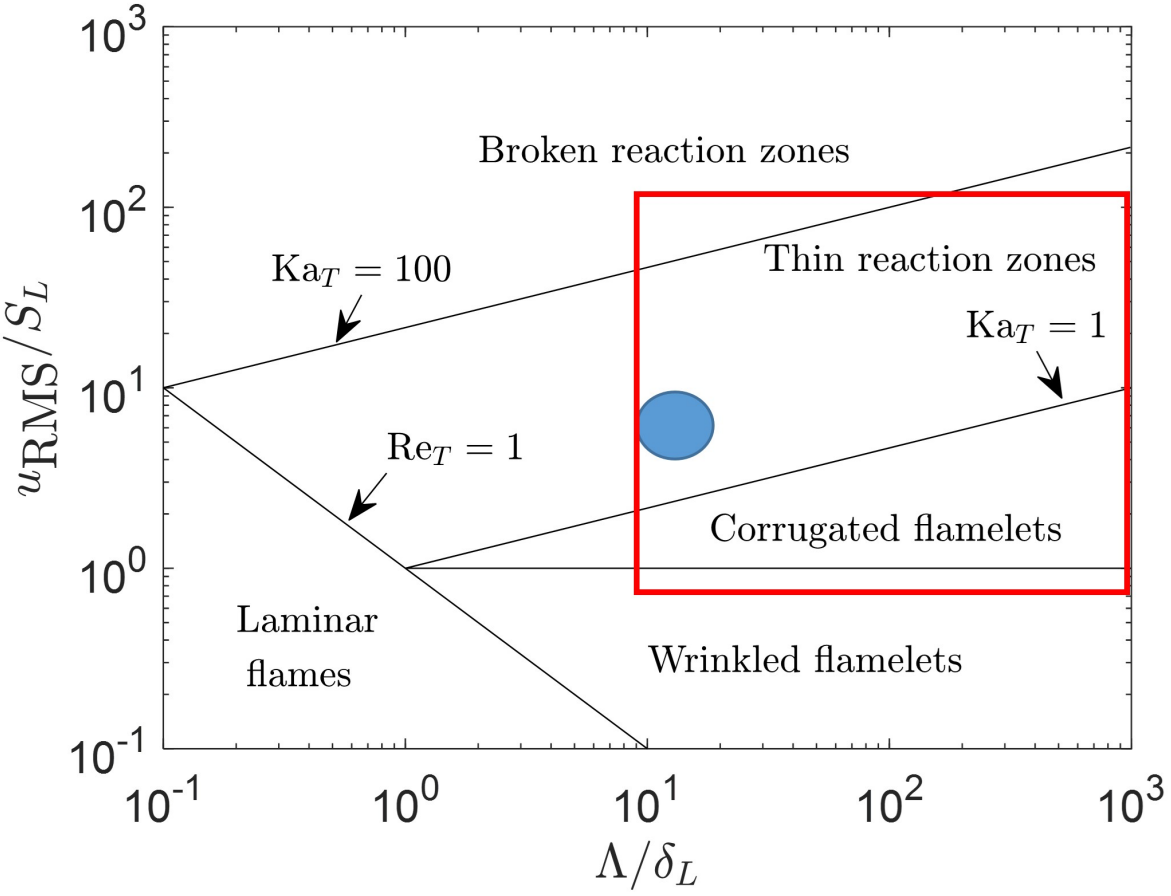

Figure 1: Borghi Diagram relating laminar and turbulent flame regimes to normalized turbulence intensity $u_{\mathrm{RMS}}/S_{\mathrm{L}}$ and normalized integral length scale $\Lambda/\delta_{\mathrm{L}}$ along with turbulent Reynolds number $\mathrm{Re_T}$ and turbulent Karlovitz number $\mathrm{Ka_T}$. Ellipse shaded in blue represents flame regime of evaluated conditions in this study.

1.4 Lewis number effects and differential diffusion

There is a challenge in developing fuel-flexible gas turbines because fuel blends with different reactivities and diffusivities greatly influence flame structure, and by extension, the turbulent burning rate. Hydrogen enrichment, which is sought after for fuel-flexibility development, is distinct from other hydrocarbons by the Lewis number [45]:

$$\mathrm{Le} = \frac{\alpha}{\mathcal{D}} \tag{11}$$

Here, α is the thermal diffusivity of the mixture ($\lambda/\rho c_\mathrm{p}$) and $\mathcal{D}$ is the diffusivity of the deficient reactant (i.e. fuel for fuel-lean combustion, oxidizer for fuel-rich combustion). The Lewis number for some common fuels in a fuel-lean condition are Le ≈ 1 for CH_4, ≈ 1.8 for C_3H_8 and ≈ 0.35 for H_2. In this case, the Lewis number is significantly less for hydrogen because it is a smaller and lighter molecule than methane/propane diffusing in the bulk gas (i.e. air). The imbalance between the thermal and mass diffusivities results in a preferential diffusion of heat over mass (or vice versa), which results in a phenomenon known as *differential diffusion*. This occurs when the Lewis number of a mixture differs from unity (Le $\neq 1$). In mixtures where Le > 1 such as fuel-lean C_3H_8-air, the mixture's larger thermal diffusivity causes the local temperature to increase in approaching reactants. For a wrinkled flame perturbed by turbulence, unburned reactants diffusing towards the negatively-curved regions of the flame (i.e. concave curvature) will exhibit larger preheat temperatures than reactants diffusing to the positively-curved regions of the flame (i.e. convex curvature). The increase in local temperature causes a burning rate enhancement in negative curvatures compared to positive curvatures, producing an inherent stabilizing effect which dampens turbulent flame wrinkling. Another perspective of high Lewis number mixtures is heat diffusing faster than reactant species diffusing into the flame, which leads the flame temperature to be lower than the flame adiabatic temperature and causes the flame to slow down. Such conditions are termed thermodiffusively-stable. Conversely, in mixtures where Le $<< 1$ such as fuel-lean H_2-air, the increased mass diffusivity produces cellular instabilities, resulting in the condition termed thermodiffusively-unstable.

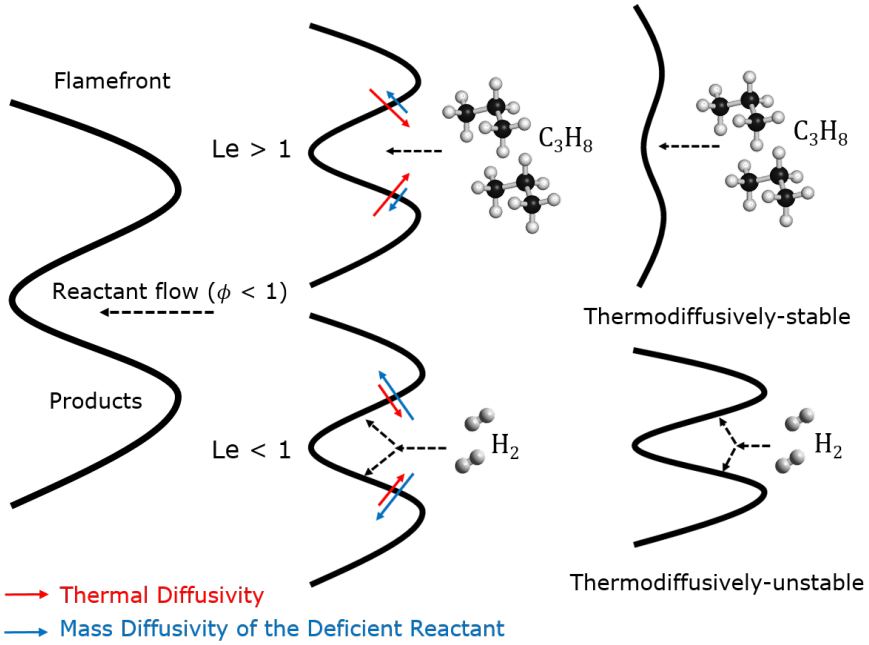

Figure 2: Differential diffusion effects for non-unity Lewis number mixtures (Top: fuel-lean C_3H_8-air, bottom: fuel-lean H_2-air).

The mechanism behind such instabilities is a result of hydrogen's preferential diffusion upon approaching a flame. Generally, hydrogen has a tendency to diffuse more towards the positively-curved regions of the flame front, leading such regions to have a higher local stoichiometry (i.e. local ϕ) than its negatively-curved regions downstream. As a result, there is a larger chemical gain leading the local burning rate in these regions to increase such that the positively-curved flamelets propagate fastest. In terms of temperature, the increase in stoichiometry at the positively-curved regions increases the flame temperature past the adiabatic flame temperature to the point where the flame speeds up. This instability, which arises from preferential diffusion of H_2, leads to a positive feedback loop where flames become increasingly stretched and propagate faster. One common theory to explain this propagation phenomenon is the leading points concept (i.e. the points of highest curvature along a flamefront most extended forward towards unburned reactants) becoming the primary control on the flame consumption speed, thereby controlling the overall turbulent burning rate [46][47]. Nevertheless, this feedback mechanism contrasts Damkhöler's first hypothesis [48], where he proposes that the turbulent flame speed is proportional to flame surface wrinkling due to turbulence such that $S_T \sim A_T/A_L$. This notion can be deemed equivalent to a proportionality between S_T and u_{RMS} (i.e. $S_T \propto u_{RMS}$), since the degree of flame surface wrinkling by FSA enhancement is effectively a measure of the turbulence intensity. Experimental studies with syngas mixtures (H_2 and CO) in a turbulent Bunsen burner have demonstrated that for

low-Lewis number mixtures, the turbulent flame speed is sensitive to flame stretch effects as a result of mixture composition, even for increasing $u_{\mathrm{RMS}}/S_{\mathrm{L}}$ [49]. Damkhöler's formulation for the turbulent burning rate has since been modified to reflect flame stretch sensitivity:

$$S_{\text{T-LC}} = I_{\mathrm{o}} S_{\mathrm{L}}^{\mathrm{o}} \frac{A_{\mathrm{T}}}{A_{\mathrm{L}}} \tag{12}$$

This formulation proposes the turbulent burning rate depends on three parameters: 1) the unstretched laminar flame speed $S_{\mathrm{L}}^{\mathrm{o}}$ due to mixture composition, 2) the increase in FSA $A_{\mathrm{T}}/A_{\mathrm{L}}$ due to turbulence, or Σ and 3) the local stretch factor I_{o} which can be represented as an enhancement on the local flame speed ($S_{\mathrm{T}}/S_{\mathrm{L}}^{\mathrm{o}}$). Similarly in laminar-flame experiments, flame stretch affects the laminar flame speed according to well-established theory:

$$S_{\mathrm{L}} = S_{\mathrm{L}}^{\mathrm{o}} - \mathcal{L}K \tag{13}$$

The stretched laminar flame speed is a function of the unstretched laminar flame speed $S_{\mathrm{L}}^{\mathrm{o}}$ and the flame stretch rate K, where $\mathcal{L}$ is the Markstein length representing how much influence flame stretch has on perturbing the burning velocity. Considering the Markstein length is found to be negative in low-Lewis number mixtures (i.e. hydrogen-enriched flames) [50], the local stretch factor I_{o} is expected to be the parameter most affected by differential diffusion in influencing the turbulent flame speed S_{T} and by extension, the turbulent burning rate. Models characterizing the increase in turbulent burning rate through the stretch factor I_{o} demonstrate a dependence on the turbulent Markstein length (and number Ma_{T}) along with the turbulent Karlovitz number, Ka_{T} [51]. According to these models, thermodiffusively-stable flames, also referred to as "weakly-stretched" where the Markstein number is low, assume $I_{\mathrm{o}} \approx 1$ in which case mixtures with high-Lewis number behave similarly to Damkhöler's first hypothesis. In thermodiffusively-unstable flames where flame stretch is expected to be more considerable, I_{o} becomes strongly coupled to Σ since any increase in local propagation speed will stretch the flame further upstream and ultimately enhance FSA. While many studies have highlighted the importance of stretch sensitivity on turbulent burning rate enhancement empirically [52][53], it still remains difficult to correlate hydrogen addition effects to flame stretch alone. Abbasi et al. attempted to probe this correlation in counterflow flames between flame stretch and hydrogen addition through the Lewis number such that a relative contribution was determined to be 76% and 24% between I_{o} and Σ respectively, having kept bulk flow properties and unstretched laminar flame speed constant [54]. However, there still remains a general controversy as to how much influence differential diffusion has on flames exposed to high turbulence intensities (i.e. $\mathrm{Ka}_{\mathrm{T}} > 1$), and if there is a dampening effect from turbulence on flame stretch phenomena. Therefore,

a similar approach to decouple flame stretch is necessary in order to study the correlation between enhanced turbulent burning rates and the onset of differential diffusion that arises from hydrogen-enrichment.

1.5 Swirling flames

A useful way to decouple flame stretch effects from hydrogen addition can be done from an analysis of swirling flames. Swirling flames provide a useful configuration to investigate the influence of flame stretch similarly to counterflow flames because of the similarity in their propagation against an opposed flow. In principle, the swirling flow velocity at the burner exit can be divided into two components: the axial velocity, u and the azimuthal velocity, w. The swirl number is a non-dimensional parameter which relates the axial components of their angular (G_{ang}) and linear (G_{x}) momentum fluxes, which provides an indication on the swirl strength in a flow [55]:

$$S = \frac{G_{\text{ang}}}{R_b G_{\text{x}}} = \frac{\int_0^\infty \rho u w r^2 dr}{R_b \int_0^\infty \rho (u^2 - \frac{1}{2}w^2) r dr} \tag{14}$$

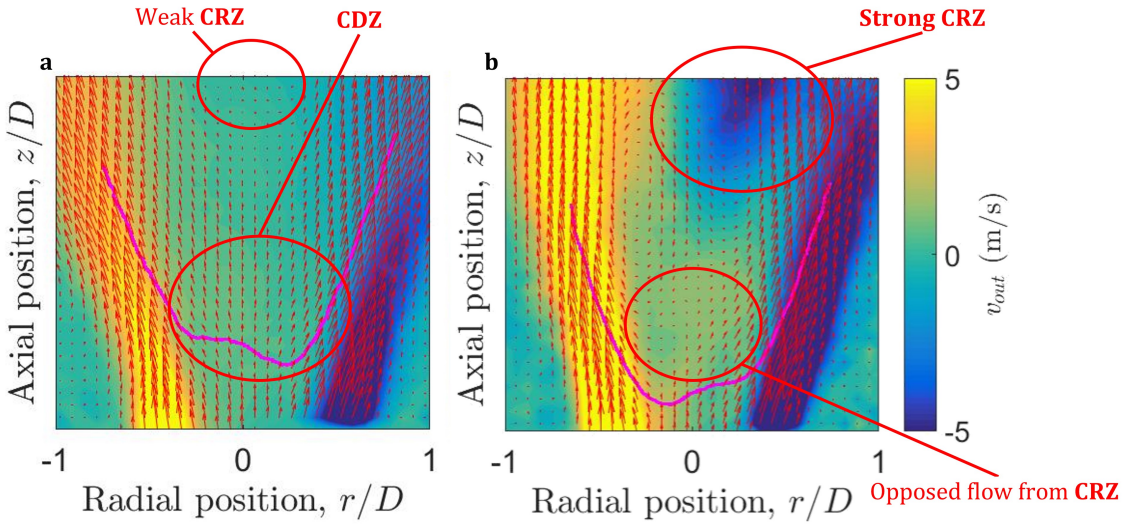

Figure 3: Example of a) low-swirl flowfield at $S = 0.6$ and $U_{\text{av}} = 13$ m/s and b) high-swirl flowfield at $S = 0.63$ and $U_{\text{av}} = 20$ m/s, both overlaid with typical, time-averaged flame surface (purple).

The swirl number is a commonly used parameter to distinguish swirling flames in two categories: 1) high-swirl and 2) low-swirl flames. High-swirl flames stabilize in a turbulent flow due to the onset of vortex breakdown, which causes flow downstream to stagnate and reverse due to an adverse pressure gradient [56]. This breakdown produces a highly-intense

central recirculation zone (CRZ) favourable for flame stabilization due to enhanced mixing of incoming unburned reactants with hot combustion products. As a result, high-swirl flame configurations are widely adopted in existing practical combustors because the intense recirculation means flames can stabilize at lower velocities. However, the enhanced mixedness of reactants and products also results in larger combustion zone residence times strongly correlated to larger amounts of NO_x emissions, which can only be mitigated up to a critical swirl number S_{crit} [57], which describes the transition between low-swirl and high-swirl stabilization dynamics.

Conversely, in a low-swirl regime, the CRZ is replaced by a central divergence zone (CDZ) considering the flow will not stagnate and reverse, but simply diverge [58]. Instead, the low-swirl flame anchors wherever the local axial flow velocity balances the local flame displacement velocity (S_{T}). As a result, the propagating flame becomes "stationary" and in most cases, lifted. Although a lifted U-shape is common in a low-swirl flame, extensive studies are still examining the transitional modes which define flame shape and flame liftoff behaviour [59]. Furthermore, the burner geometry also heavily influences the swirling flow's aerodynamics, which dictates the likelihood for flame liftoff. As a result, the advantage of lifted low-swirl flames means the burner is subjected to lower heat fluxes, and therefore lower thermal stress, which is attractive to gas turbine manufacturers looking to substitute high-swirl flame configurations. On a macroscopic scale, this allows existing combustors to avoid excessive material deterioration leading to engine damage ultimately prolonging their useful lifespan. In the context of fuel-flexibility, the development of low-swirl injectors can be readily adaptable in existing gas turbines to adhere to a larger range of turbulent flame speeds for hydrogen- and low-carbon fuel blends. As such, they provide an opportunity to produce flames capable of stabilizing at lower lean-blowout limits, which means low-swirl injectors can replace high-swirl configurations to achieve lower NO_x emissions.

The difference between a low- and high-swirl flowfield characteristics is further illustrated in Figure 3. In the $S = 0.6$ flowfield, whose mean location is approximated by the purple contour, involves a flame typically stabilizing in the shear layers of the swirling flow and suspends the flame such that it propagates similarly to a counterflow flame. The flame stabilization dynamics change greatly if it were exposed to a higher-swirl flowfield, such as $S = 0.63$. As highlighted by the red ellipses in the high-swirl flow, the downstream CRZ influences the flow upstream enough such that negative velocities would arise where the flame would nominally stabilize. This effect is not as prevalent in the $S = 0.6$ flowfield even if the geometric swirl number describes a swirl intensity near the theoretical limit between low- and high-swirl. Therefore, the influence of the CRZ downstream on flame stabilization is considered negligible. For simplicity, the hydrogen-enriched mixtures evaluated at $S = 0.6$

are deemed low-swirl due to the development of a CDZ rather than a dominating CRZ.

The momentum balance present in low-swirl flame stabilization leads all low-swirl flames to be "self-similar" such that they can be described by the following equation:

$$1 - \frac{d\overline{U}}{dx}\frac{(x_\mathrm{f} - x_\mathrm{o})}{\overline{U}} = \frac{S_\mathrm{T}}{\overline{U}} = \frac{S_\mathrm{L}(1 + Ku')}{\overline{U}} \tag{15}$$

The normalized axial divergence rate $d\overline{U}/dx/\overline{U}$ characterizes the axial flow acceleration upstream of the flame (i.e. a_z) and is similar for various mixtures [60], further implying the self-similarity trait of low-swirl flames. Furthermore, it was assumed in this study that the turbulence generation system similar to other designs in axisymmetric burners [61][62] would provide near-isotropic turbulence such that the normalized turbulence intensity $u_\mathrm{RMS}/\overline{U}$ scales linearly with bulk velocity. Therefore, any displacement of the low-swirl flame's brush position x_f from its virtual origin x_o is dictated by increases or decreases in its local flame displacement speed, S_T. Essentially, the momentum balance in Equation 15 characterizing low-swirl flames provides a better benchmark than high-swirl flames to understand the effect of hydrogen enrichment on combustion behaviour. In a laboratory setting, the flame displacement is readily observable in low-swirl configurations and can be correlated with changes in the local flame displacement speed S_T. Furthermore, experiments involving low-swirl flames can be designed to isolate the dependence of S_T to stretch effects K alone as a means for characterizing the influence of differential diffusion with hydrogen enrichment.

1.6 Project objectives

This thesis aims to investigate hydrogen enrichment in fuel-lean, premixed, low-swirl CH_4 flames in an effort to characterize their flammability and their topology as a function of differential diffusion effects. This thesis work is largely stemming from similar analyses done for premixed, turbulent counter-flow flames in an effort to broaden understanding of differential diffusion phenomena in premixed, turbulent combustion. The project objectives are to address the following questions:

1) What is the impact of hydrogen enrichment on turbulent, low-swirl CH_4 flames and can it be correlated to differential diffusion effects?

2) What are the leading mechanisms attributed to differential diffusion on the turbulent burning rate of hydrogen-enriched, low-swirl flames?

In order to answer these research questions, the design and manufacture of an unconfined, low-swirl burner apparatus capable of sustaining lifted flames was carried out at McGill University. The primary design challenge associated with the low-swirl burner was in finding a

suitable sweep of experimental conditions to correlate differential diffusion effects to hydrogen enrichment without risk of flashback. The flame behaviour for all mixture conditions are analyzed through the use of laser diagnostics and processing techniques developed at McGill and the National Research Council of Canada.

In this study, unconfined flames are the focus over confined flames in order to eliminate the influence of recirculation in the outer shear layers induced by a combustion chamber. Such recirculation may be favourable for flame stability, but the objective is to isolate the influence of flame stretch on flammability as much as possible. Furthermore, the lack of confinement is also favourable for improved optical access of the burner. In general, conditions which produced lifted low-swirl flames were preferred over attached flames for two reasons: 1) the mean flame brush position provides a good feedback mechanism for determining likelihood of flashback with increasing hydrogen enrichment and 2) local flame phenomena can be studied similarly to a counter-flow configuration.

In this thesis, time-resolving turbulent flames will be necessary to understand the local flame phenomena influenced by differential diffusion such as curvature and total flame stretch as well as propagation phenomena influencing the turbulent flame speed and the turbulent burning rate. Furthermore, the two-color PLIF diagnostics will provide additional insight on turbulent-flame interactions at higher turbulence intensities for hydrogen-enriched flames.

2 Experimental Methodology

2.1 Apparatus design

Low-swirl burners can be designed from a variety of geometries such as a fixed-vane, movable-vane block or tangential swirl configuration [63]. Since swirling velocity data is not always consistently available, it is favourable to represent the swirl number as a function of geometry (see Appendix for derivation):

$$S = \frac{2}{3}\tan\theta \frac{1-R^3}{1-R^2+[m^2(\frac{1}{R^2}-1)^2]R^2} \tag{16}$$

In this formulation for a fixed-vane configuration, the vane angle θ, the ratio of the centerbody radius to the burner radius $R = R_c/R_b$ and the mass flux ratio m (i.e. mass flow split) become new design variables for the approximate determination of the swirl number.

A fully-controllable swirl burner has been designed from this geometry at McGill University to study lifted, unconfined swirling flames and their flame structure. The burner is comprised of a feeding block with four tangential inserts allowing premixed reactants to flow from the burner's inner and outer plena to the nozzle exit. Upstream of each plenum, a metallic mesh sits atop a bed of ceramic beads each 1 mm in diameter to: 1) ensure sufficient premixing of reactants 2) establish radial uniformity in the flow and 3) serve as flame arrestor in case of flashback. Reactants flowing through the inner plenum pass through a turbulence screen 10.8 mm in diameter with a hole diameter of 1.5 mm (i.e. blockage ratio of $\approx 59\%$) and produce a turbulent, *inner axial flow*. In conventional low-swirl burners with one plenum, the flow passing through the swirl injector gets redirected partly through the swirl annulus, with the remainder passing through the turbulence generating plate. This flow split is dictated by the pressure drop across the swirl injector and can be represented by the following formula:

$$C_d = \frac{2\Delta P}{\rho U^2} \tag{17}$$

It stands to reason that turbulence plates with larger blockage ratios will not only produce larger turbulence intensities, but also increase pressure drop across the swirl injector. As a result of a larger drag coefficient, C_d, more flow is forced through the annular vane section, increasing the swirl intensity and therefore, the theoretical swirl number. However, the inclusion of two independent plena allows control of the flow split in order to independently control the swirl number and the turbulence intensity from flow passing through the TGP. In this manner, flow passing through the turbulence plate in the inner plenum can be controlled

to provide different turbulence intensity conditions. This feature was inspired from a two-plenum design by Ballachey et al. [64] where the fuel-air mixture composition is equivalent in both the inner and outer plena.

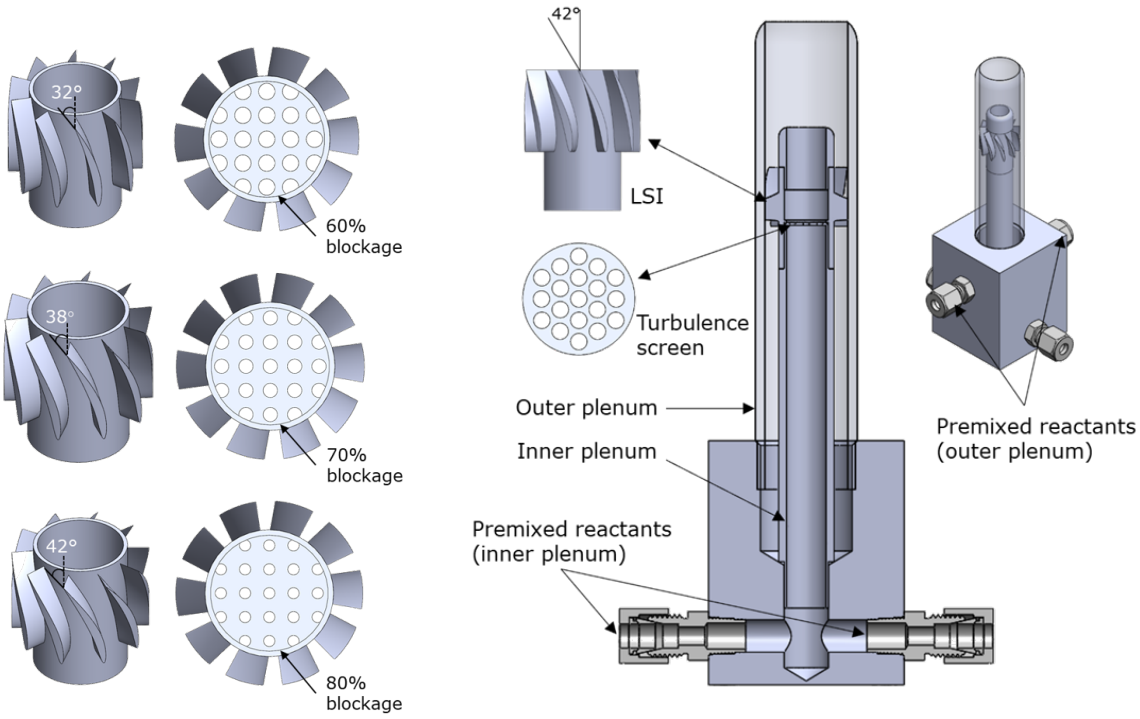

Figure 4: Design iterations of low-swirl injector by varying vane angle θ and blockage ratio (%) by varying hole diameter D_{hole}. R value was kept constant in LSI prototype testing (i.e. $R = 0.67$) (left). Cross sectional side view of low-swirl burner (LSB) final design with labelled components (right).

Reactants flowing through the outer plenum pass through an annular swirl injector and produce an *outer swirling flow*. The swirl injector is composed of 10 vanes each angled at 42°, with an outer diameter of 21.6 mm and an inner diameter of 10.4 mm. The inner plenum's nozzle exit is recessed 31.6 mm from the exit nozzle of the burner. As illustrated by Feyz et al. [65], the recess length is an important design parameter which influences whether the flame is lifted or attached for a specified equivalence ratio and swirl number. From Figure 4, it is used to describe the distance between the trailing edge of the vanes and the nozzle exit. For increasing recess length, the turbulence of the outer swirling flow decays, producing larger axial momentum than angular momentum. This increased axial momentum is sufficient enough to induce a lifted stability mode as the flow is less divergent. Conversely, for smaller recess lengths, the angular momentum is larger at the nozzle exit, leading to larger flow divergence. At this point, the flame will anchor to the nozzle rim where

velocities are lowest, producing an attached flame.

Nine swirl injector designs were prototyped using a 3-D printer, producing different iterations of θ (32^o-42^o) and blockage ratios ($\approx$ 60%-80%) for a fixed R. Once a sufficient liftoff was achieved in sweeping between 100% CH_4 and 100% H_2 flame, the swirl injector was 3-D printed in metal using an aluminum alloy powder (Al-Si7-Mg, named F357) and was machined on-site to smooth surface roughness from printing (see Figure 4).

2.2 Experimental conditions

In order to isolate differential diffusion phenomena as much as possible with increasing hydrogen enrichment, the laminar flame speed and the bulk velocity were kept constant to maintain the same *reactivity* and same *turbulence intensity* across each condition. The laminar flame speed is kept constant because hydrogen addition will result in a flame propagating faster than a methane-air mixture, even for the same fuel-air ratio. In this respect, the equivalence ratio ϕ needs to be decreased with hydrogen enrichment to compensate for hydrogen's enhanced reactivity (see Figure 5). Furthermore, the bulk velocity is kept constant to ensure turbulence uniformity in the flowfield across each condition. By this token, each hydrogen-enriched mixture with an equivalent propagation behaviour in a laminar flowfield experiencing the same turbulent flowfield serves to highlight the role of molecular diffusion on combustion behaviour.

The experimental conditions evaluated in this study of differential diffusion considers hydrogen enrichment in lean, premixed methane-air low-swirl flames, according to the fuel-lean combustion reaction equation:

$$X_{H_2}H_2 + (1 - X_{H_2})CH_4 + \frac{4 - 3X_{H_2}}{2\phi}(O_2 + 3.76N_2) \rightarrow \text{Products} + \text{Heat} \tag{18}$$

From Eq. 18, the term X_{H_2} characterizes the blend between CH_4 and H_2 as a volumetric fuel fraction, where a pure CH_4-air reaction corresponds to $X_{H_2} = 0$ % and a pure H_2-air reaction corresponds to $X_{H_2} = 100$ %. The conditions evaluated in this study are listed in Table 1 below:

Table 1: Conditions evaluated at constant $S_{\mathrm{L}} = 0.267$ m/s, constant $U_{\mathrm{av}} = 13$ m/s and constant $S = 0.6$ (i.e. flow split between outer and inner plenum is 82.5%-to-17.5%) at NRC and McGill University. $X_{\mathrm{H_2}} = 100$ % achieved in laboratory, but not listed here.

$X_{\mathrm{H_2}}$ (%)	ϕ	$\mathrm{Le_{eff}}$	$\Lambda/\delta_{\mathrm{L}}$	$u_{\mathrm{RMS\text{-}3C}}/S_{\mathrm{L}}$	T_{ad} (K)
0	0.8	0.999	12.04	5.89	1938
20	0.75	0.858	12.12	5.69	1892
40	0.70	0.722	12.16	5.79	1832
60	0.64	0.587	12.26	5.84	1757
80	0.56	0.451	12.29	6.11	1657

Since fuel-lean H_2-air mixtures propagate faster than fuel-lean CH_4-air mixtures for the same equivalence ratio, ϕ must vary with increasing hydrogen enrichment to maintain S_L constant. Although there are several ways to define the effective Lewis number in the sweep towards high-hydrogen content [66], a volume-based effective Lewis number is used in this study and is defined by: $\mathrm{Le_{eff}} = (1 - X_{\mathrm{H_2}})\mathrm{Le_{CH_4}} + X_{\mathrm{H_2}}\mathrm{Le_{H_2}}$, where Lewis numbers for both fuels are evaluated at an equivalent equivalence ratio for each mixture. The diffusive flame thickness δ_{L} is defined by: $\delta_{\mathrm{L}} = \lambda/\rho_{\mathrm{u}} c_{\mathrm{p}} S_{\mathrm{L}}$, where λ is the thermal conductivity, c_{p} is the specific heat capacity and ρ_{u} is the density of the unburned reactants. The integral length scale is approximated in a 2-D rectangular region whose width corresponds to half the diameter of the inner plenum (i.e. from -0.25D to 0.25D) and whose height corresponds to the mean flame location. An average integral length scale in this region was assumed to be $\Lambda = 3.76$ mm, which is comparable to the radius of the inner plenum (≈ 5 mm). The three-component (3C) RMS velocity ($u_{\mathrm{RMS\text{-}3C}}$) was also approximated in this region for each experimental condition as measure for calculating the average turbulence intensity of each condition:

$$u_{\mathrm{RMS\text{-}3C}} = \sqrt{\frac{1}{3}(u_{\mathrm{RMS}}^2 + v_{\mathrm{RMS}}^2 + w_{\mathrm{RMS}}^2)} \tag{19}$$

The similarity in $u_{\mathrm{RMS\text{-}3C}}/S_{\mathrm{L}}$ demonstrates a valid assumption that the swirl burner's TGP provides a near-equivalent turbulent flowfield on the flame. The parameters dictating normalized integral length scale and normalized turbulence intensity means that the flame conditions evaluated are expected to lie in the BPTRZ regime of the Borghi diagram. These approximations were made from the two dimensional-three component (2D-3C) velocity data obtained at the NRC. All mixture and thermodynamic properties were computed in Cantera using the GRI-Mech 3.0 thermochemical reaction mechanism over a 3 mm domain width using $P_{\mathrm{in.}} = 1$ atm (101.3 kPa) and $T_{\mathrm{in.}} = 298$ K as inlet references, coupled to a multi-component transport model while enabling Soret effect [67].

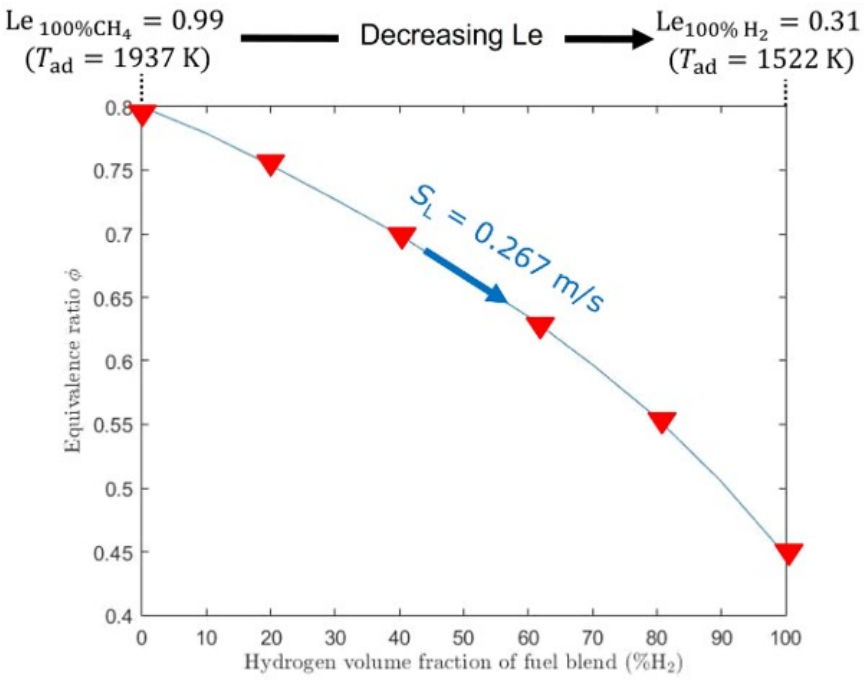

Figure 5: Experimental sweep of equivalence ratio and effective Lewis number $\mathrm{Le}_{\mathrm{eff}}$ from $X_{\mathrm{H_2}} = 0$ % to $X_{\mathrm{H_2}} = 100\%$ in maintaining S_{L} constant.

2.3 Laser Diagnostic Techniques

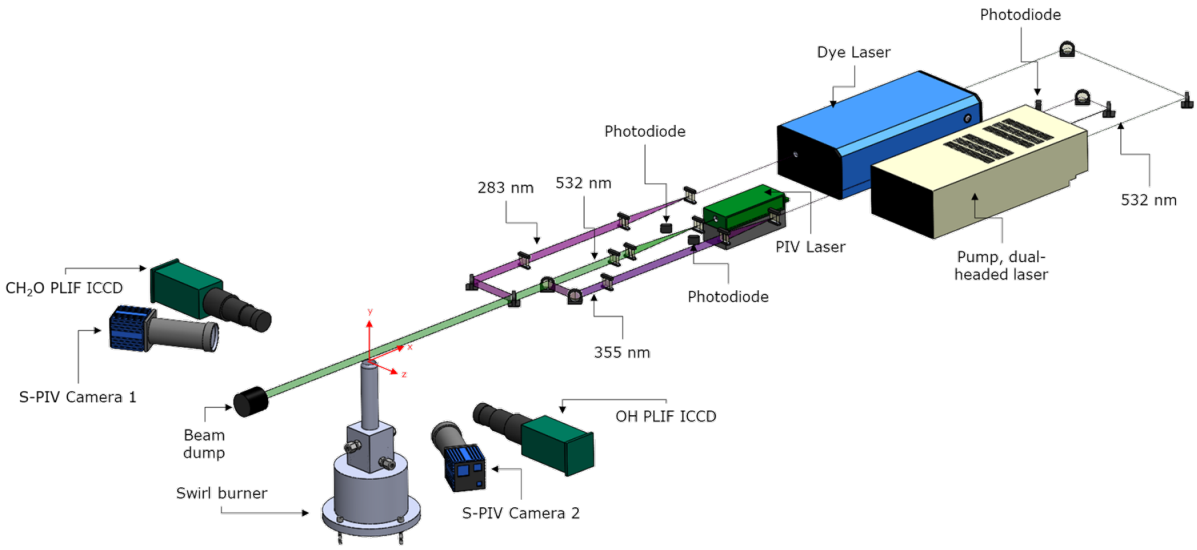

Figure 6: Simultaneous planar laser-induced fluorescence (PLIF) & stereoscopic particle image velocimetry (S-PIV) setup at the National Research Council of Canada

2.3.1 Planar laser-induced fluorescence

Planar (2-D) laser-induced fluorescence (PLIF) is a laser diagnostics technique that has also been employed in many studies to qualitatively and quantitatively observe flame topology such as curvature and concentration of flame radicals such as methylidyne (CH), hydroxyl (OH) and formaldehyde (CH_2O). To induce fluorescence, the flame's target species are excited by a laser emitting in the ultraviolet range (100-400 nm), allowing the molecule to experience an electronic-vibrational-rotational transition. After energy from the incident laser is absorbed, the excited molecule loses excess vibrational energy until the molecule relaxes back to the lowest vibrational level from the excited state. Throughout this relaxation, the process by which it emits a photon at a wavelength larger than the incident laser wavelength is termed "fluorescence", producing a fluorescent signal which can be captured by an ICCD camera.

Planar laser-induced fluorescence was used to calculate the heat release rate of each experimental condition from the pixel-to-pixel multiplication of the formaldehyde [CH_2O] and hydroxyl [OH] species concentration in the flame [68]. The PLIF setup incorporates a dual-headed, Nd:YAG pump laser (Spectra Physics) and dye laser (Sirah PrecisionScan). The pump laser delivers two laser beams, one of which is frequency-doubled (532 nm) and the other being frequency-tripled (355 nm), both of which have a pulse repetition frequency of 10 Hz. The 532 nm beam passes through the dye laser (whose dye medium is Rhodamine 6G) and is frequency-doubled to 283 nm in order to excite the A←X (v'=1,v"=0) transition of OH. The average laser energy is maintained near 5 mJ/pulse to remain within the linear regime of laser irradiance to OH fluorescence [69]. Similarly, the 355 nm beam excites the $A^1A_2 \leftarrow X^1A_1$ electronic transition of CH_2O and operates at an average energy of 205 mJ/pulse due to the relatively lower signal-to-noise ratio (SNR) of CH_2O fluorescence. The OH and CH_2O laser beams were formed into laser sheets where the OH beam was pulsing 400 ns before the CH_2O beam to isolate fluorescence signals from both species. The energy per pulse of the 283 nm beam is kept low to ensure that OH fluorescence scales linearly with laser power, or the irradiance of the laser sheet. The shot-to-shot laser energy was recorded in real-time via photodiodes (ThorLabs) and was consolidated using a LeCroy oscilloscope (Wavesurfer 510). The OH and CH_2O fluorescence are detected by a pair of intensified CCD cameras (Princeton Instruments) at an imaging frequency of 2 fps in frame straddling mode with an average projected spatial resolution of 92 μm/pixel (see Figure 7).

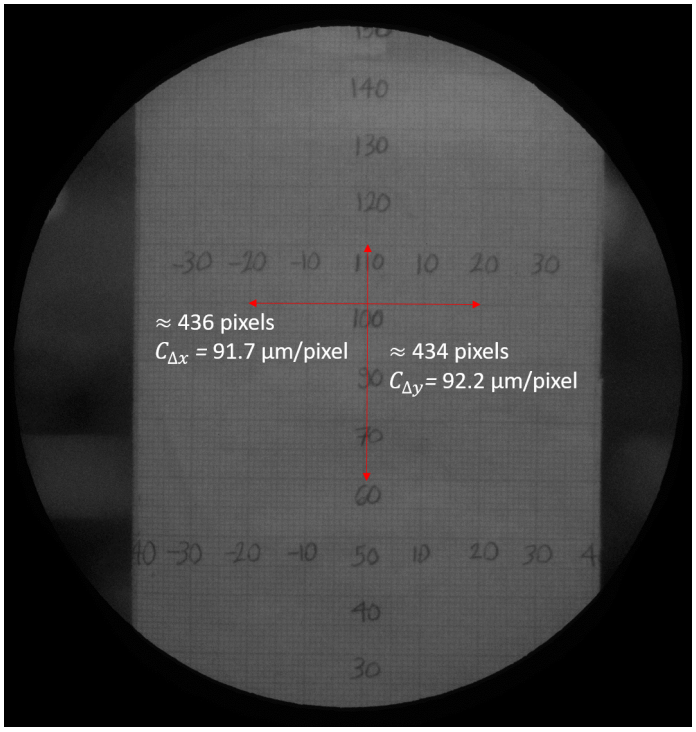

Figure 7: Full-chip ICCD image of Cartesian grid used to image PLIF field-of-view in physical coordinates.

Each camera was fixed with a UV lenses having a focal distance of $f = 105$ mm and $f\# = 4.5$ and $f\# = 4$, respectively. The OH camera was equipped with a bandpass filter (center wavelength 320 $\pm$ 20 nm) and the CH_2O camera was equipped with a longpass (cut-on wavelength 395 nm) and shortpass filter (cut-off wavelength 500 nm) to improve the signal-to-noise ratio (SNR), which becomes significantly weaker with increasing hydrogen enrichment. Raw OH and CH_2O images (see Figure 8) were spatially registered in post-processing using a perforated plate target to correlate pixels captured from both ICCD cameras to the same physical space. A total of 520 instantaneous frames were collected for OH, CH_2O, background intensity and laser profiles for 283 nm/355 nm while the shot-to-shot laser energy was collected simultaneously.

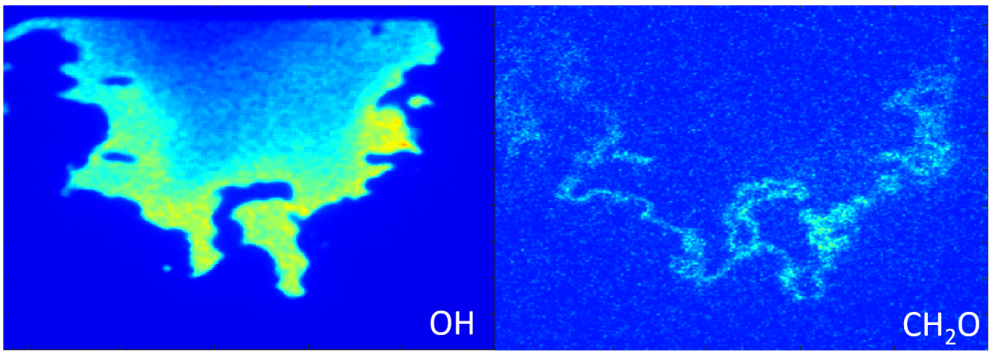

Figure 8: Raw OH (left) and CH_2O (right) signals from simultaneous PLIF.

The laser profile and shot-to-shot laser energy were normalized by their average intensity per dataset. Furthermore, the raw signals for both OH and CH_2O were normalized by the shot-to-shot variations in laser energy and the laser profile (i.e. $L(x,y)$) according to standard methods for image correction [70]:

$$S_e(x,y) = \frac{S_{tot}(x,y,t_i) - [w(x,y)S_{back}(x,y,t_i) + S_{dark}(x,y,t)]}{w(x,y)L(x,y)} \tag{20}$$

Raw images were also corrected for mean background intensity (i.e. S_{back}) to filter any reflection from the opposing camera lenses as well as well as general background noise (i.e. S_{dark}). Corrected OH and CH_2O images were median filtered (7x7 and 12x12 respectively), while CH_2O images were further de-noised according to the procedure developed by An et al. [59].

2.3.2 Stereoscopic particle image velocimetry

Stereoscopic particle image velocimetry (S-PIV) involves the capture of Mie scattering from a flow seeded with tracer particles. However, in a stereoscopic configuration, two cameras are arranged at an angle such that the image plane, the lens plane and the object plane intersect at a common point to satisfy the Scheimpflug condition, which means the object plane can be a plane of focus even if it is not parallel to the image plane. The cameras are arranged at an angle to capture particle images simultaneously at the same region of interest. However, while the interrogation windows from the left and right camera record Δx and Δy displacements in the same physical space, the calibration parameters mapping displacements onto the image plane enable an out-of-plane velocity component to be resolved using a trigonometric least squares method [71].

Stereoscopic PIV was used for the second experimental campaign to calculate the two-dimensional, three component (2D-3C) velocity field of each flame condition. The S-PIV

setup incorporates a double-pulse, Nd:YAG laser (Twins CFR PIV200), delivering a pair of laser beams at 532 nm which straddle the PLIF pulses and are time delayed between 5-30 μs depending on the bulk velocity of the condition. The 532 nm laser beam was formed into a 38 mm tall, rectangular sheet, coincident with the PLIF laser sheets. Solid Al_2O_3 particles ($\sim 1\mu$m diameter) were seeded in the inner axial and outer swirling flows, where each plena was equipped with particle seeders manufactured in house. Two CMOS cameras (LaVision S-PIV) calibrated with a dot target (Type 106-10) were used to capture the Mie scattering signals from the solid particles and were arranged at an angle of 120° to satisfy the Scheimpflug condition. The cameras imaged a field-of-view (FOV) approximately 76 mm x 64 mm with a projected spatial resolution 34.1 μm/pixel. Velocity field vectors were calculated in DaVis 8.4 (LaVision software) from the spatial cross-correlation of consecutive PIV images, where a final interrogation window pass 32 x 32 pixels in size was used at an overlap of 50%. This led to a vector resolution of 0.55 mm/vector and vector spatial resolution of 1.1 mm. The PLIF and S-PIV laser systems were triggered using a LaVision timing unit (PTU) and a delay generator (DG645) such that the 283 nm laser beam fired 2 μs after the first PIV pulse. The timing of each laser pulse was monitored using the oscilloscope to ensure Mie signals would not conflict with fluorescence signals. Any axial adjustments to the burner were controlled via LabVIEW using a three-axis traverse to ensure the flame was appropriately imaged in the PLIF/PIV FOV. An example of the simultaneous PLIF/S-PIV measurement is illustrated in Figure 9.

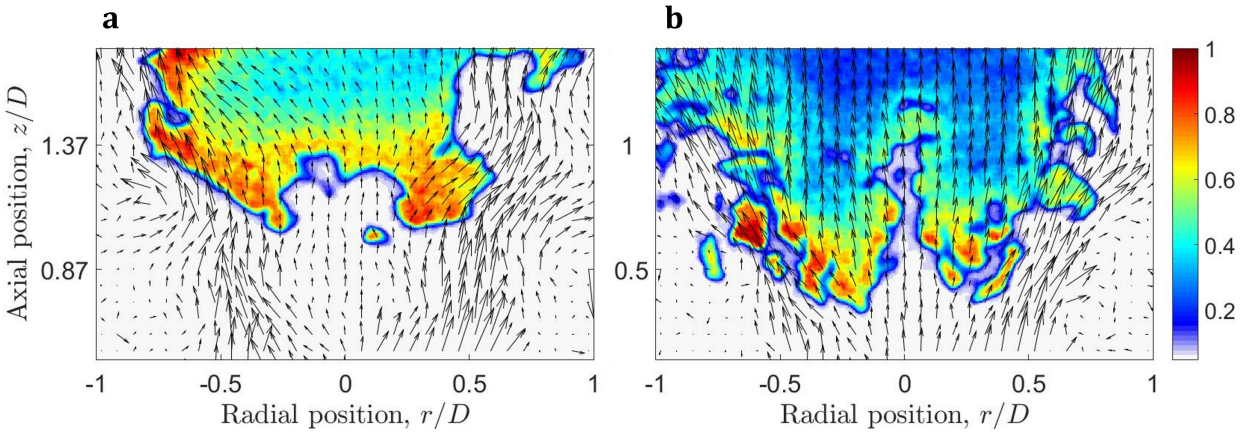

Figure 9: Instantaneous OH-PLIF signal overlaid with instantaneous velocity vector field obtained from S-PIV technique for a) $X_{H_2} = 0\%$ and b) $X_{H_2} = 80\%$ H_2 conditions. Color map depicts PLIF signal normalized by maximum intensity within frame.

2.3.3 High speed particle image velocimetry

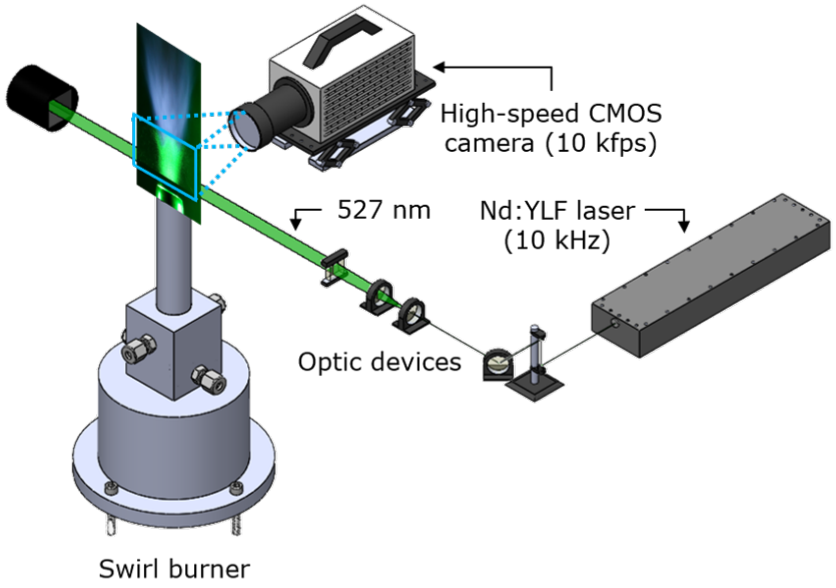

Figure 10: High-speed particle image velocimetry (PIV) setup at McGill University.

Similarly to S-PIV, high-speed, 2-D particle image velocimetry (PIV) is a laser diagnostics technique that has been widely used by the combustion community to obtain time-resolved velocity measurements of turbulent flow fields in both reacting and non-reacting cases. Typically, a dual-headed laser emits a pair of beams at a set repetition frequency with pulses separated by some exposure time Δt. The collimated beams are then formed into a thin, 2-D laser sheet (using an appropriate set of optical devices) to illuminate an area of interest in the flow field. For experiments conducted in this thesis, the area of interest is a transversal cross section of the flame located above the burner nozzle exit. The imaged flow of combustion reactants is seeded with tracer particles, which the laser sheet illuminates and induces an elastic "Mie" scattering of light subsequently captured by a high-speed CMOS camera. The camera captures particle images consecutively, a software tool converts these into interrogation windows, which are then cross-correlated and processed to determine the displacement of the particles over the exposure time Δt, generating velocity data for the flow field [72].

High-speed PIV was used in the second experimental campaign to calculate the two-dimensional velocity field at a high laser repetition rate in order to resolve turbulence length and time scales. The high-speed PIV setup incorporates a single-head, diode-pumped Nd:YLF laser (Photonics DM20-527), delivering a laser beam at 527 nm at a repetition rate

of 10 kHz. The laser beam is formed into a 40 mm, 30 mm and 20 mm tall rectangular sheet in evaluating conditions with higher H_2 content. Atomized oil droplets are seeded in the inner axial flow from an oil droplet generator (TSI 9307-6) approximately 1μm diameter in size. Air flow passing through the inner plenum is redirected to the atomizer by means of a micrometer-controlled bypass, which allows a set amount of air to flow through an array of Laskin nozzles which bubble the seed liquid (i.e. canola oil). The oil droplets are aspirated through the system and simultaneously mixed with the bypassed air in a mixing tank downstream of the atomizer.

A high-speed CMOS camera (Photron Fastcam SA5) was used to record particle Mie scattering in a viewer software at 10 kfps. The high-speed camera was equipped with a 105 mm lens (AF Micro Nikkor) and focused to a spatial resolution of 29.5μm/pixel (33.9 pixel/mm). The camera's spatial resolution was calculated from the negative image of a Thorlabs 0.5 mm spacing (R2L2S3P3) distortion grid target. The resolution was computed by normalizing the actual 0.5 mm grid spacing by the imaged radial and axial pixel separation between grid dots. The FOV of the flame was adjusted manually using a 2-axis stage to radially align the center of the CMOS camera to the center of a Thorlabs graduated card placed atop the nozzle exit. The centerline of the graduated card was aligned with the centerline of the burner (see Figure 11).

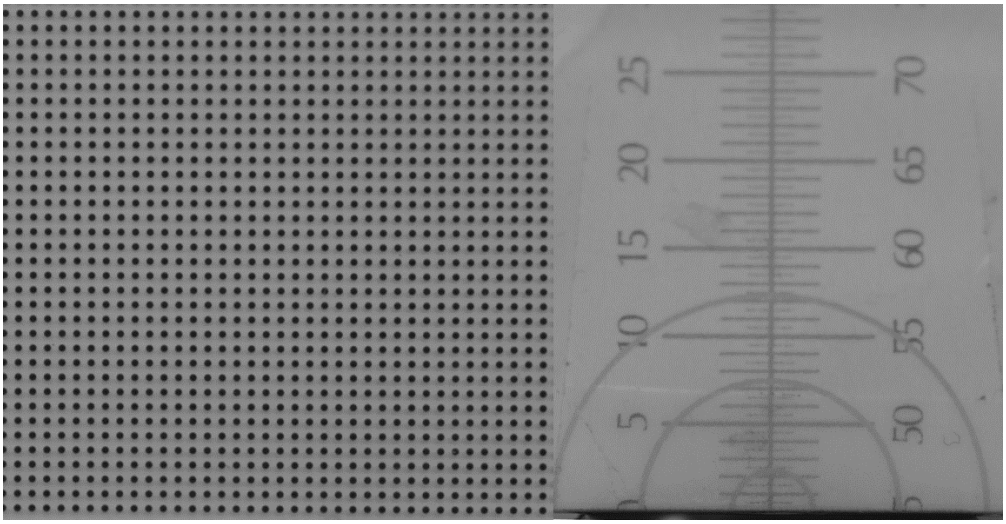

Figure 11: Thorlabs 0.5 mm spacing calibration target used to calculate CMOS spatial resolution (left). Thorlabs graduated card used to image flame FOV (right). Images are not to scale.

All high-speed PIV images were processed in Lavision software (DaVis 8.2.1) and were organized in an (n-1) multi-frame buffer scheme (i.e. first frame paired with second frame, second frame paired with third frame, etc.) in order to correlate the velocity flow field from

an image pair. For all conditions evaluated using high-speed PIV, only one atomizer was used in the current experimental configuration. As a result, the inner axial flow originating from the inner plenum was chosen to be seeded with atomized oil droplets instead of the swirling flow originating from the outer plenum. Given the manner with which low-swirl flames stabilize, seeding in the inner flow was deemed more appropriate. However, the outer swirling flow was still imaged in the FOV of the camera, but the seeding density in the swirling flow's shear layers was sparse. Therefore, only the velocity field pertaining to the center core flow was considered in post-processing (see Figure 12). For each image pair, a multi-pass, decreasing window, sequential cross correlation scheme was used to compute the pixel displacement field with a resolution down to a 32×32 pixel interrogation window size with 75% overlap. This scheme resulted in an interrogation window spatial resolution of $944\mu\text{m} \times 944\mu\text{m}$ in physical coordinates, enough to resolve the smallest eddies in the flow (given the $D_{\text{hole}} = 1.5$ mm). The raw displacement data was then exported to MATLAB where velocities were inferred using a finite differencing scheme. The main limitation in this setup was the use of a single-head laser instead of a dual-headed laser, which meant that the maximum Δt used to calculate the velocity field was effectively the time delay between laser pulses at 10 kHz (i.e. $\approx 10^{-4}$ s). Within a 32×32 interrogation window, and given the current spatial resolution, PIV computation was only able to resolve convective flow velocities up to ≈ 9.15 m/s. From DaVis, 10,000 image pairs were processed for all experimental conditions.

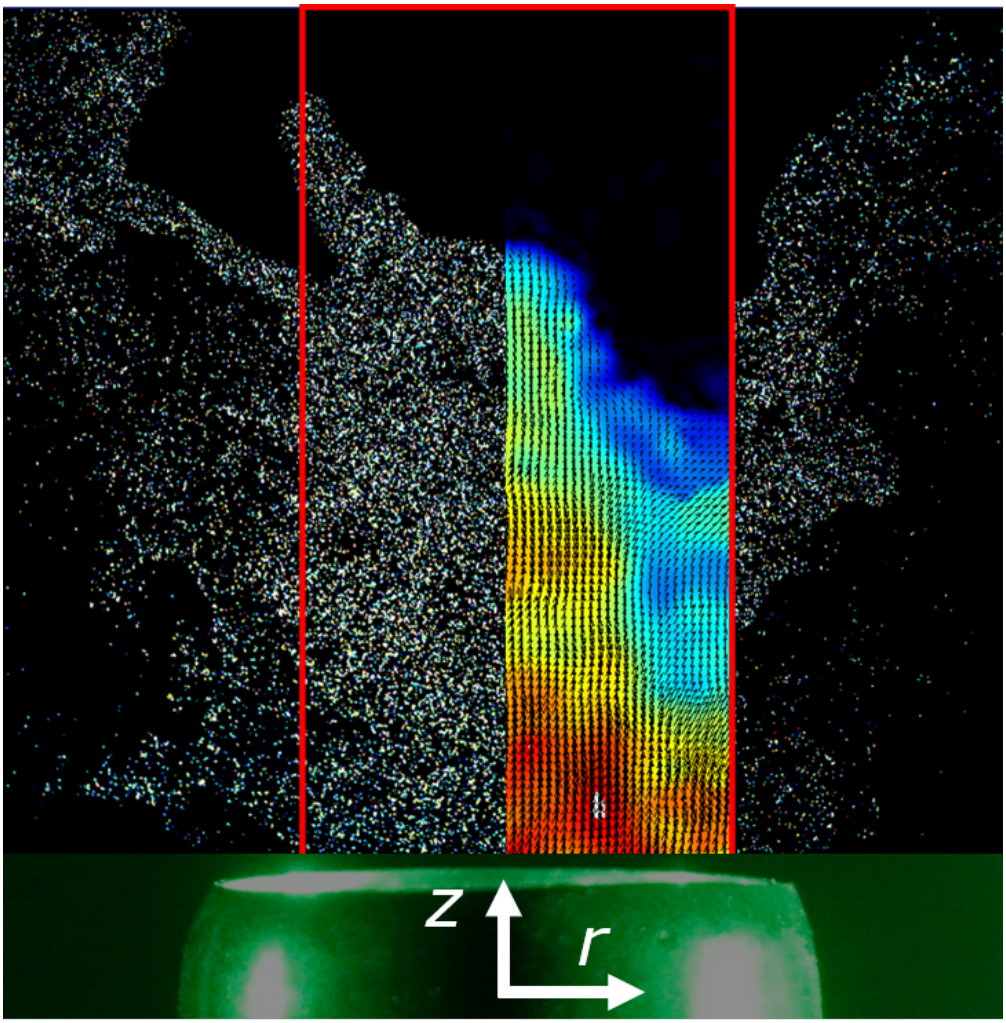

Figure 12: Mie scattering tomography of CH_4-air condition seeded with atomized oil droplets (left) with corresponding post-processed instantaneous velocity vector field (right). Processed velocity field only in delineated region in red corresponding to seeded center core flow.

2.4 Processing techniques

2.4.1 Measurement of instantaneous flame location and local flame curvature

Mie scattering tomography of micron-sized atomized canola oil droplets are dual-purposed: 1) to serve as adequate tracking of the flow for PIV processing and 2) to track the flame surface by delineating regions between burned products and unburned reactants. The vaporization of the atomized oil droplets marks the approximate preheat layer of the flame reaction zone due to canola oil's vaporization point at $T_s \approx 576$ K (see Appendix for uncertainty in flame surface tracking). Each frame is Gaussian filtered with a 2-D Gaussian smoothing ker-

nel 9-10 pixels in size, binarized with an edge threshold of 0.075 and 5x5 median filtered (see Figure 13). The result is a white and dark region depicting burnt products and unburned reactants from which the Laplacian of Gaussian filter can be applied in detecting the edge between these regions. The edge contour produced is subsequently tracked in a chronological manner from the top of the frame using the Pavlidis contour tracking algorithm [73]. For each grid point along the flame contour, a total of 13 adjacent grid points (i.e. 6 on the left, 6 on the right of the grid point of interest) are considered for the calculation of the instantaneous slope dy/dx in absolute coordinates (x,y) and the local curvature κ. In this calculation, a 4^{th} order polynomial is fitted through the 13 grid points in MATLAB. The curvature with respect to flame coordinates (r,z) is calculated from the following formula, where r depicts the radial direction and z depicts the axial direction:

$$\kappa = \frac{r'z'' - z'r''}{(r'^2 + z'^2)^{3/2}} \tag{21}$$

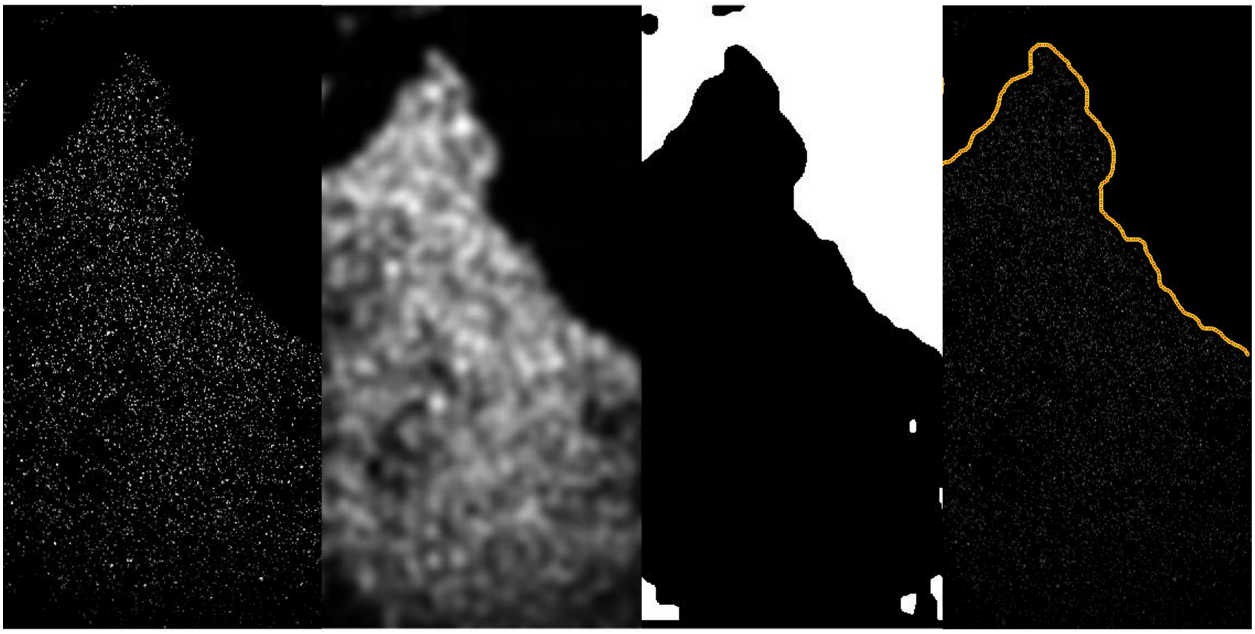

Figure 13: Edge detecting algorithm used to track flame front surface comprised of Gaussian and median filtering, binarizing resultant image and subsequently pixel tracking (left to right).

2.4.2 Measurement of flame surface area, FSD and mean progress variable

In this study, the increase in turbulent flame surface area Σ normalized by the equivalent laminar condition (A_T/A_L) is estimated from a 2-D transversal cross-section of the flame. Since PLIF and Mie scattering tomography cannot resolve the out-of-plane flame surface

area, the estimated flame surface area can be thought of as the length of the flame contour multiplied by the thickness of the laser sheet. Considering the laser sheet thickness remains equivalent throughout testing means that the increase in flame surface area can be further simplified to an analysis on the normalized flame length. However, the flame surface area enhancement will continue being expressed as a ratio of areas for simplicity. In order to calculate the flame length, the flame contour can be extracted from the OH signal, which has been shown to be a good marker for the flame reaction zone, and from the tracked flame contours processed from the Mie scattered images.

The mean flame surface area (FSA), A_{L} is extracted from the mean progress variable field along the $\overline{c} = 0.5$ isoline, which can be expressed by the following equation:

$$c = \frac{T - T_u}{T_b - T_u} \tag{22}$$

Here, the progress variable, also known as the temperature progress variable c_{T} is defined as the actual temperature difference between the unburned reactants (room temperature at 293 K) and the flame contour normalized by the temperature difference between burnt and unburned reactants. From OH PLIF, the mean progress variable $\overline{c} = 0.5$ corresponds to an actual temperature range between 900-1100 K depending on the hydrogen fuel-blend evaluated. From Mie scattering tomography, the tracked flame surface only marks a maximum temperature of 576 K due to the vaporization and disappearance of the seeded oil droplets. Therefore, the mean flame surface (i.e. $\overline{c} = 0.5$) from Mie scattering occurs at a temperature of $\approx$ 435 K.

The OH PLIF signals were binarized with a threshold between 0.001-0.003 depending on the % H_2 condition to ensure sharper curvatures were not smoothed in the filtering process. The binarized OH signals were then Sobel gradient-filtered to produce a 1-pixel thick, 2-D contour of the flame front. Given the spatial resolution of the OH PLIF camera (i.e. 92 μm/pixel), the flame length can be calculated by the total number of non-zero pixels in the image and subsequently converted to a physical length. Notably, the gradient filter of the binarized OH image ensures that the flame front length is not being underestimated by counting diagonal portions of the flame as 1 pixel. From Mie scattering tomography, the flamefront having been tracked using the Pavlidis algorithm means that a gradient function in MATLAB can be applied to all coordinates along the flame contour, expressed as a matrix instead of a binarized image. The gradient magnitude is computed and summed across the entirety of the flame contour to get an approximation of the flame length, which is then calibrated to physical coordinates by the spatial resolution of the CMOS camera (i.e. 0.0295 mm/pixel).

2.4.3 Measurement of local flame displacement velocity

Using high-speed laser diagnostics, the local flame displacement velocity (S_T) can be determined at each flame grid point of the tracked flame surface and is calculated as the summation of the local convective velocity of the flow, S_u and the local flamelet velocity in the flow coordinate system, S_F normal to the flame front:

$$S_{\mathrm{T}} = (S_{\mathrm{u}} + S_{\mathrm{F}}) \cdot \mathbf{n} \tag{23}$$

In a stabilized laminar flame, the local flame displacement velocity would be equal to the convective velocity of the flow ($S_{\mathrm{u}} = S_{\mathrm{u,ref}}$) considering $S_{\mathrm{F}} = 0$. However, in turbulent flames, the motion of the flame is much more considerable and is non-negligible in the determination of S_{T}. The 2-D S_{u} and S_{F} velocities were measured using a MATLAB algorithm developed at McGill [54].

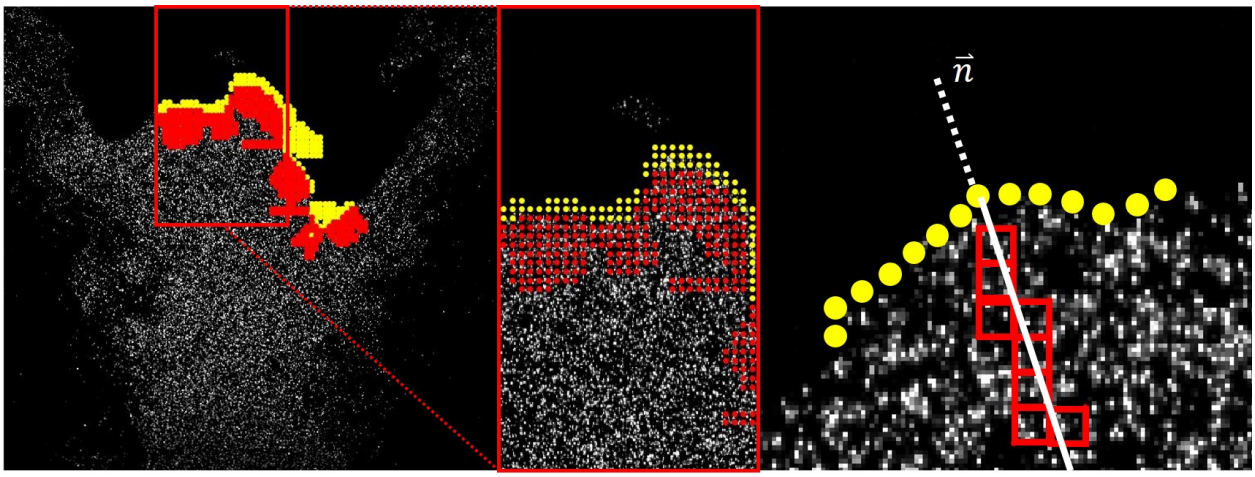

Figure 14: Measurement technique of S_{u} component of the local flame displacement speed (left) further zoomed-in (middle) to illustrate sampling rate of calculation. Schematic for the calculation of S_{u} at one flame grid point illustrated (right).

The convective velocity of the flow (i.e. S_{u} velocity component) is calculated from the velocity field data computed in DaVis 8.2.1 for each frame in a dataset. The S_{u} velocity is the unburned gas velocity upstream and normal to the flamefront. It is calculated from the projection of velocity vectors located at the corner of neighbouring interrogation windows onto the normal line (i.e. $S_{\mathrm{u}} = S_{\mathrm{PIV}} \cdot \mathbf{n}$) passing through the flame grid point of interest (see Figure 14). The algorithm evaluates velocities one interrogation window at a time up to a distance of 2 mm upstream of the flame. This distance is chosen to ensure only velocities in the vicinity of the flamefront are considered. Since the interrogation window corners are not normally equidistant to the normal line, projected velocity data at those corners are

weighted depending on their relative position from the normal line. In each interrogation window, a velocity vector with magnitude and relative position to the flame contour is calculated. This process is repeated for the 9 interrogation windows (i.e. equivalent to 2 mm distance) evaluated upstream of the flame grid point of interest and sampled across the flame contour in increments of 8 pixels where velocity data exists. In laminar flames, the final velocity associated with the S_{u} component at the flame grid point is theoretically the minimum velocity. However, this algorithm considers the average of the two nearest weighted velocities to the flame contour to account for flamefront wrinkling due to the turbulence. The convective velocity is assigned a positive value if the incoming reactant velocity is pointed towards the flame and a negative value if pointed away from the flame.

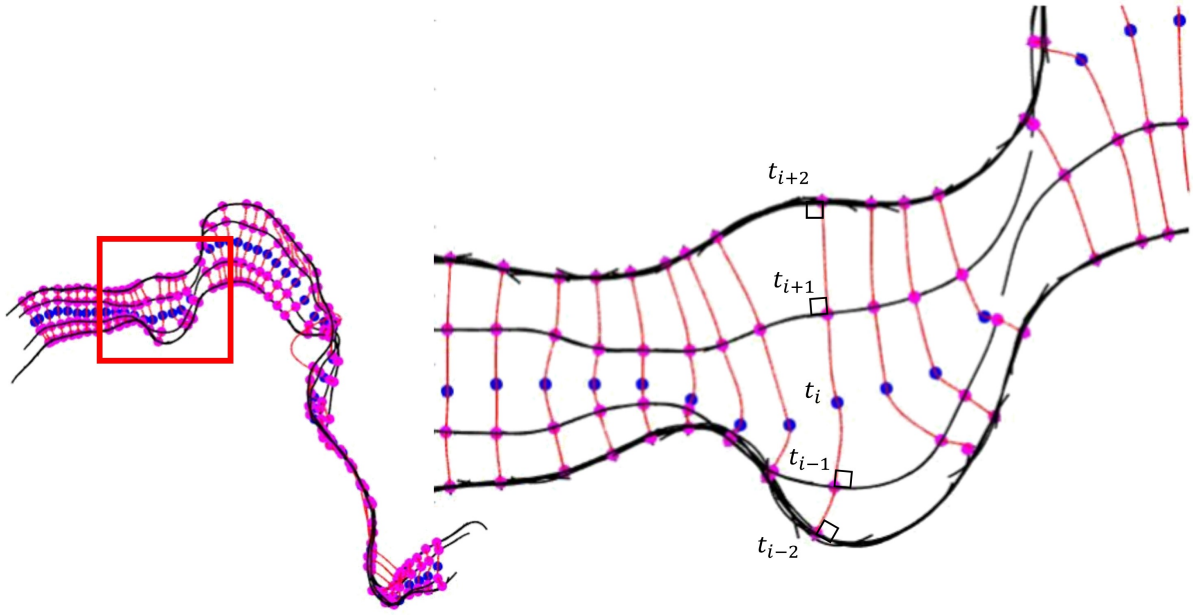

Figure 15: Schematic of measurement technique of S_{F} component of local flame displacement speed.

The S_{F} velocity component at time t_i considers the motion of the tracked flame surface through five successive flame fronts: two upstream of t_{i} at time $t_{\mathrm{i\text{-}1}}$ and $t_{\mathrm{i\text{-}2}}$, and two downstream of t_{i} at time $t_{\mathrm{i+1}}$ and $t_{\mathrm{i+2}}$ (see Figure 15). In this schematic, the blue dots represent the present flamefront coordinates while the purple dots represent the coordinates of the successive flamefronts. The flamelet velocity at one grid point is correlated to the successive flame fronts by an optimization of the minimum distanced between them. Once correlated grid points are identified between flame fronts, their motion is tracked along a continuous, third-order polynomial whose motion is normal to each successive flame front. Knowing the

relative distance z travelled, the velocity is calculated using a fourth-order finite-differencing scheme [74]:

$$S_{\mathrm{F}} = \left(\frac{\partial z}{\partial t}\right)_{t_{\mathrm{i}}} \approx \frac{8(z_{t_{\mathrm{i+1}}} - z_{t_{\mathrm{i-1}}}) - (z_{t_{\mathrm{i+2}}} - z_{t_{\mathrm{i-2}}})}{12\Delta t} \tag{24}$$

The S_{F} velocity component is considered positive if the flamelet propagates towards the incoming reactant flow and negative if propagating away from the reactant flow. There are several factors which render successive flamefront tracking complex such as: flamefront wrinkling due to turbulence, disappearance of flame grid points in and out of the imaged FOV and spurious velocities as a result of the flamelet moving too fast, resulting in erroneous tracking. As a result, not all 10,000 instantaneous frames were processed effectively. To improve the efficiency of the algorithm, only a shortened region of the tracked flamefront was considered ($-0.23D_{\mathrm{nozzle}} \leq r \leq 0.23D_{\mathrm{nozzle}}$) while S_{F} velocities exceeding the bulk velocity $U_{\mathrm{av}} = 13$ m/s were neglected as non-physical.

2.4.4 Measurement of local hydrodynamic strain rate

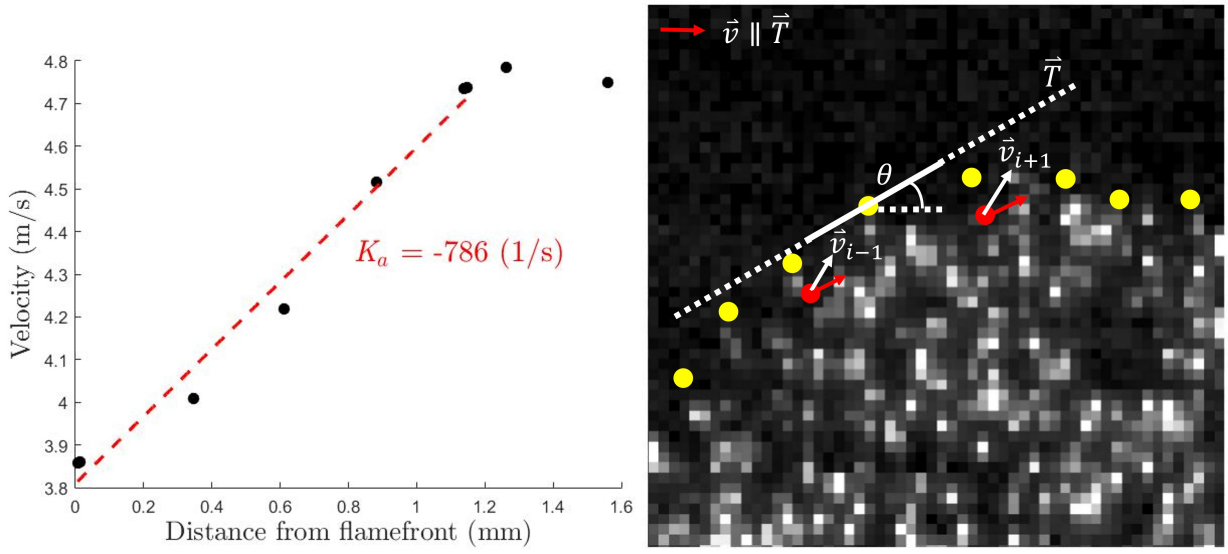

Figure 16: Example calculation of the S_{u} component at an arbitrary flame grid point where K_{a} represents the hydrodynamic axial strain (left). Schematic for the calculation of the hydrodynamic tangential strain $K_{\mathrm{s,t}}$, which is a component of the flame stretch rate K, for an arbitrary flame grid point (right).

The hydrodynamic tangential strain rate (s^{-1}) is defined by the change in tangential flow velocity nearest the flame, and is a component of the total flame stretch rate, K. In the same way that S_{u} considers projection of velocity vectors onto the normal line passing through

each flame grid point, the tangential strain rate considers the projection of velocity vectors onto its tangent line. The hydrodynamic tangential strain is calculated by considering the tangent slope at the flame grid point of interest P_{i}, which is obtained from flame surface tracking techniques. Knowing the angle of inclination of the tangent line (θ), the adjacent velocities near the flame grid point (at $P_{\mathrm{i+1}}$) and $P_{\mathrm{i\text{-}1}}$) along the axial (z) and radial (r) directions are projected onto the tangent line vector by computing the inner product (see Figure 16). The difference in projected velocities at $P_{\mathrm{i\text{-}1}}$ and $P_{\mathrm{i+1}}$ normalized by the distance between them results in the tangential strain at P_{i} in units of (1/s). This algorithm for computing the tangential component of S_{u} is sampled at every 8 pixels along the flame contour, corresponding to the interrogation window overlap from PIV processing where velocity data exists.

3 Results

The effect of hydrogen enrichment on fuel-lean, premixed, CH_4-air low-swirl flames is evaluated to observe the influence of differential diffusion in mixtures with a decreasing effective Lewis number Le_{eff}. By time-resolving turbulence for a large dataset using high-speed PIV, the statistics for flame location, flame surface density, flame displacement speed and flame stretch components such as curvature and tangential strain can be extracted locally to characterize flame behaviour with hydrogen enrichment. Further characterization of the low-swirl flowfield and differential diffusion effects are accomplished from simultaneous S-PIV/OH PLIF techniques as a means to confirm the similarity of the low-swirl flowfield and to provide further insight on the evolution of the estimated flame surface area in hydrogen-enriched mixtures.

3.1 Similarity of low-swirl flames

The similarity in flowfield of the low-swirl flame is examined for all evaluated conditions by comparing the mean velocity fields, the turbulence intensity $u_{\mathrm{RMS}}/\overline{U}$ and the normalized axial divergence rate $d\overline{U}/dx/\overline{U}$ for a constant bulk velocity U_{av}. From the mean 2-D 3C velocity field obtained at the NRC (see examples in Figures 17-18), the radial profiles of the mean axial (z direction), radial (r direction) and azimuthal (k direction) velocity normalized by the bulk velocity U_{av} are plotted in Figures 19-21. Similar velocity profiles have also been obtained from Cheng et al.'s work on flow field characteristics of low-swirl flames [75][76], highlighting self-similarity upstream of the flame is consistent for reacting and non-reacting flows. However, in the figures below, it is important to note that the radial profiles of velocity for compositions $X_{\mathrm{H_2}} = 0\%$ to $X_{\mathrm{H_2}} = 80\%$ are capturing the flow at different axial locations downstream relative to the nozzle exit. This is because different levels of H_2 enrichment lead to different flame liftoff heights (further detailed in section 3.2). As a result, the burner datum needs to be adjusted to ensure the flame is captured within the FOV of the diagnostics laser sheet. Effectively, the increase in mean axial velocity at locations further downstream of the nozzle exit are evident that the radial profiles are capturing velocities upstream and downstream the flame. While the bulk velocity is kept constant for each condition, the jump in axial velocity is evident of the gas acceleration due to thermal expansion by the flame. Ultimately, the flow acceleration decays leading to a slight drop in mean axial velocity, as illustrated in Figures 20-21 at the $z/D = 1.34$ and $z/D = 1.16$ locations respectively. The radial profiles of the mean radial and mean azimuthal velocity also demonstrates a continuously diverging flame downstream consistent with the stabilization mechanism understood with low-swirl flames.

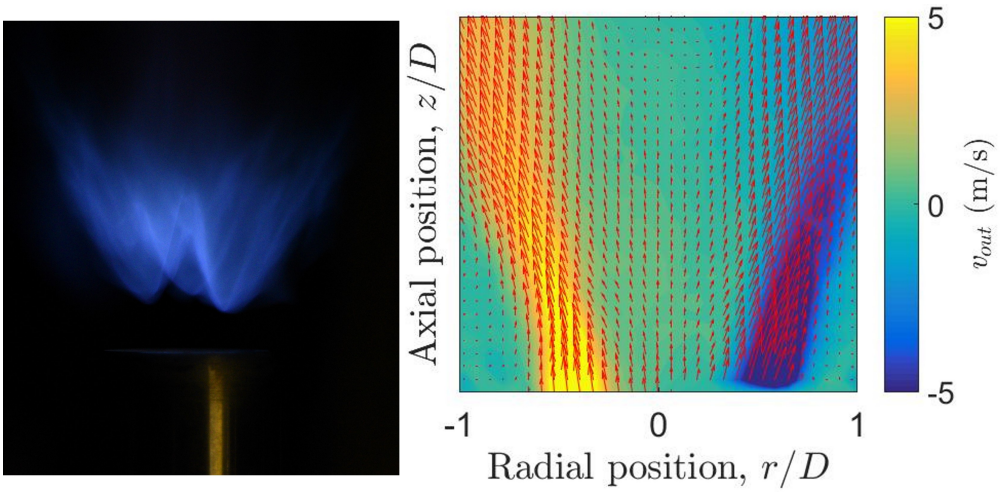

Figure 17: CH_4-air low-swirl flame (left) and average 2D-3C velocity vector field obtained from S-PIV for CH_4-air mixture at $\phi = 0.8$, $U_{\text{av}} = 13$ m/s (right). Color map depicts value of azimuthal, out-of-plane velocity component.

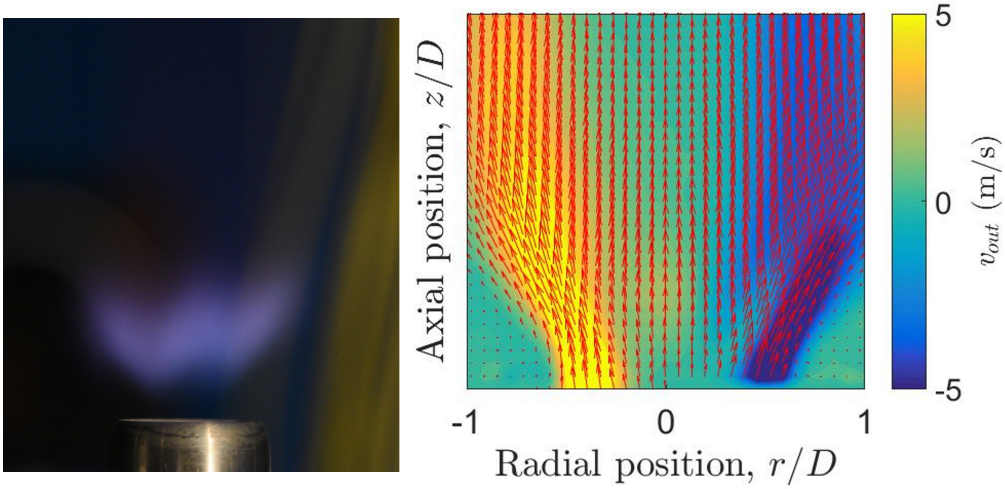

Figure 18: H_2-air low-swirl flame (left) and average 2D-3C velocity vector field obtained from S-PIV for H_2-air mixture at $\phi = 0.45$, $U_{\text{av}} = 13$ m/s (right). Color map depicts value of azimuthal, out-of-plane velocity component.

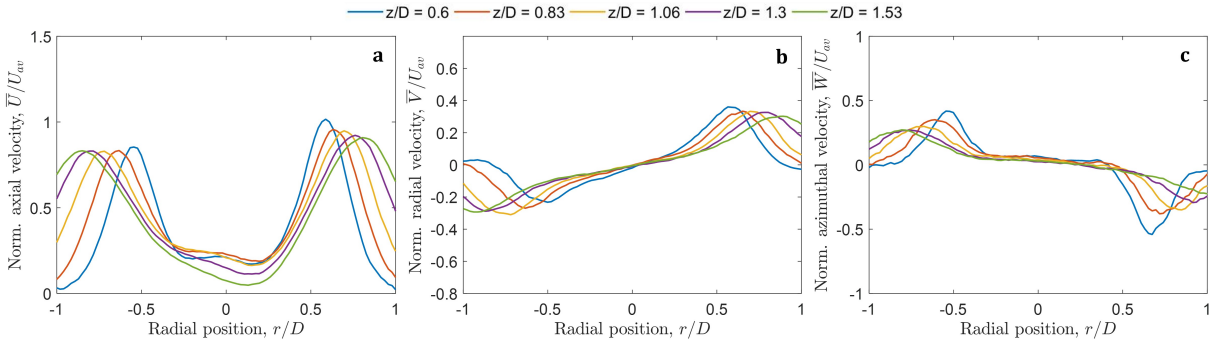

Figure 19: Radial profiles of mean velocity normalized by bulk velocity U_{av} for $X_{\text{H}_2} = 0\%$ in a) axial b) radial and c) azimuthal directions at different z/D locations downstream relative to nozzle exit (see legend).

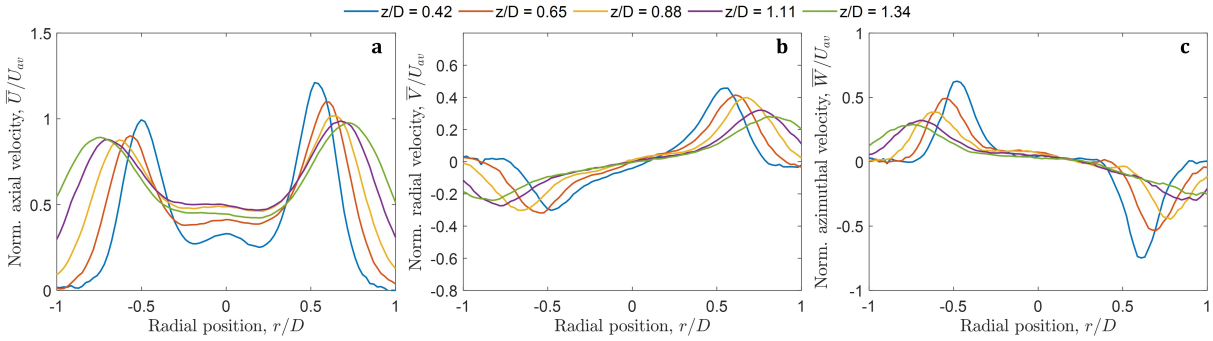

Figure 20: Radial profiles of mean velocity normalized by bulk velocity U_{av} for $X_{\text{H}_2} = 40\%$ in a) axial b) radial and c) azimuthal directions at different z/D locations downstream relative to nozzle exit (see legend).

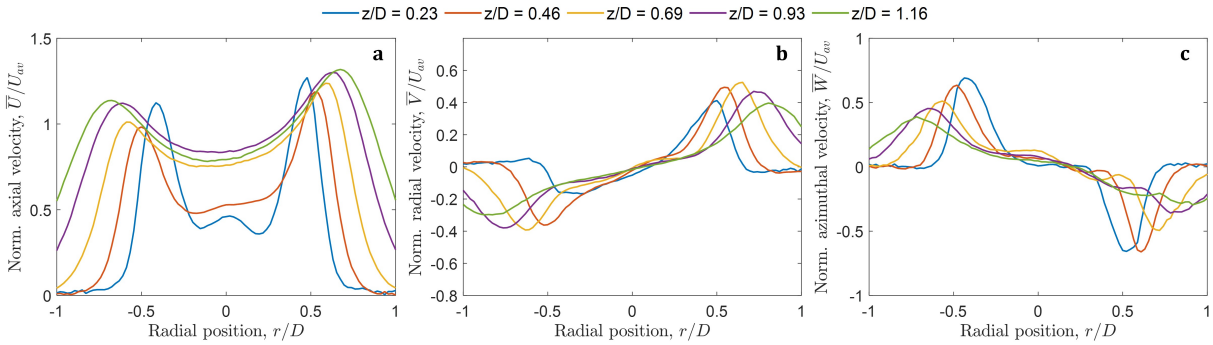

Figure 21: Radial profiles of mean velocity normalized by bulk velocity U_{av} for $X_{\text{H}_2} = 80\%$ in a) axial b) radial and c) azimuthal directions at different z/D locations downstream relative to nozzle exit (see legend).

The similarity in flow field is also evaluated by examining the axial turbulence intensity (i.e. $u_{\text{RMS}}/\overline{U}$) in Figure 22 and the RMS velocity normalized by the bulk velocity (i.e.

$u_{\mathrm{RMS}}/U_{\mathrm{av}}$) in Figure 23. As expected from both figures, the turbulent energy decay is evident the further the flow traverses downstream of the nozzle exit. Nevertheless, the radial profiles of axial turbulence intensity are larger for the $X_{\mathrm{H_2}} = 0\%$ condition than the $X_{\mathrm{H_2}} = 80\%$. From the analysis on the mean velocity fields for different levels of H_2 enrichment, a smaller flow acceleration is to be expected for the CH_4-air mixture than that with a larger hydrogen content. Therefore, the larger turbulence intensity for $X_{\mathrm{H_2}} = 0\%$ may be attributed to a normalization by a smaller mean axial velocity field. However, if the RMS velocities are to be normalized by the bulk velocity U_{av} instead, the profiles collapse between roughly $10\% \leq u_{\mathrm{RMS}}/U_{\mathrm{av}} \leq 20\%$. This suggests the RMS velocities scale with bulk velocity as a result of turbulence generated by a perforated plate. Furthermore, this suggests keeping a constant bulk velocity across each condition is a valid approach towards maintaining a near-constant turbulence effect on the flame for each condition. Similar profiles of RMS velocity normalized by bulk velocity have also been achieved by Cheng et al. in their low-swirl apparatus [76].

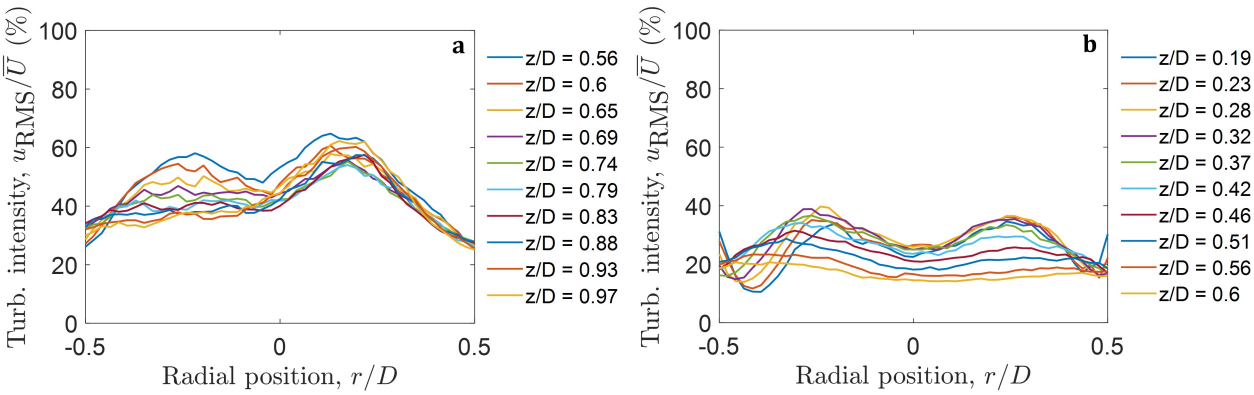

Figure 22: Radial profiles of turbulence intensity $u_{\mathrm{RMS}}/\overline{U}$ expressed as a percentage for: a) $X_{\mathrm{H_2}} = 0\%$ and b) $X_{\mathrm{H_2}} = 80\%$ at different locations z/D downstream relative to nozzle exit. Each plot has its corresponding legend situated to the right.

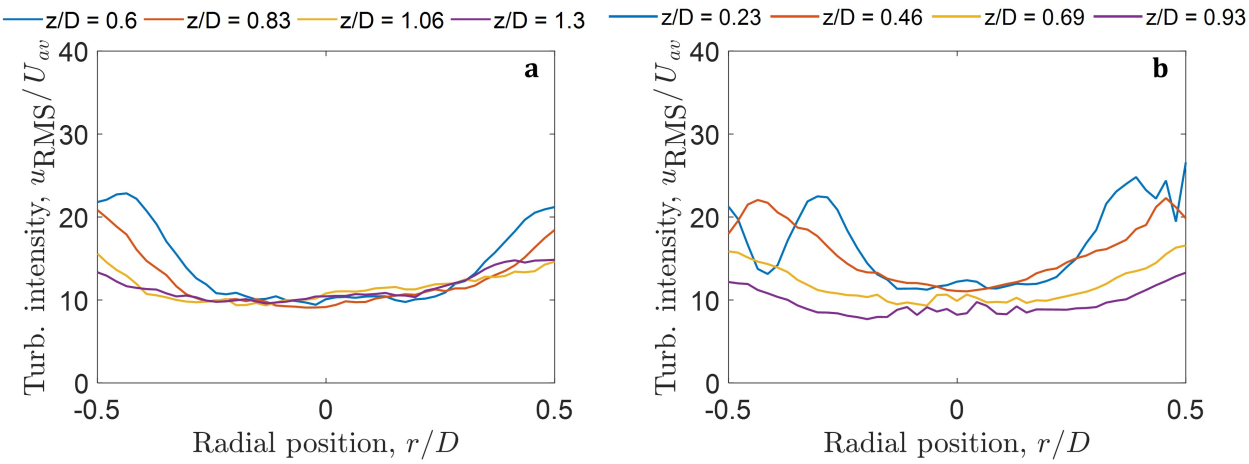

Figure 23: Radial profiles of RMS velocity normalized by bulk velocity u_{RMS}/U_{av} expressed as a percentage for: a) $X_{\mathrm{H_2}} = 0\%$ and b) $X_{\mathrm{H_2}} = 80\%$ at different locations z/D downstream relative to nozzle exit. Each plot has its corresponding legend situated on top.

The normalized axial divergence rate $d\overline{U}/dx/\overline{U}$ characterizes the axial flow deceleration upstream of the swirling flame (i.e.a_{z}) normalized by the bulk velocity of the condition. Typically, the deceleration in flow velocity is synonymous with the axial flame stretch rate K_{a} expressed in units of (1/s), but the normalization by the bulk velocity means the axial divergence rate is expressed instead in units of (1/mm). Therkelsen et al. have demonstrated that this parameter is nearly constant in a reacting flow at $\phi = 0.7$ for various Reynolds numbers and tends towards a_{z} = -0.017 (1/mm) [60].

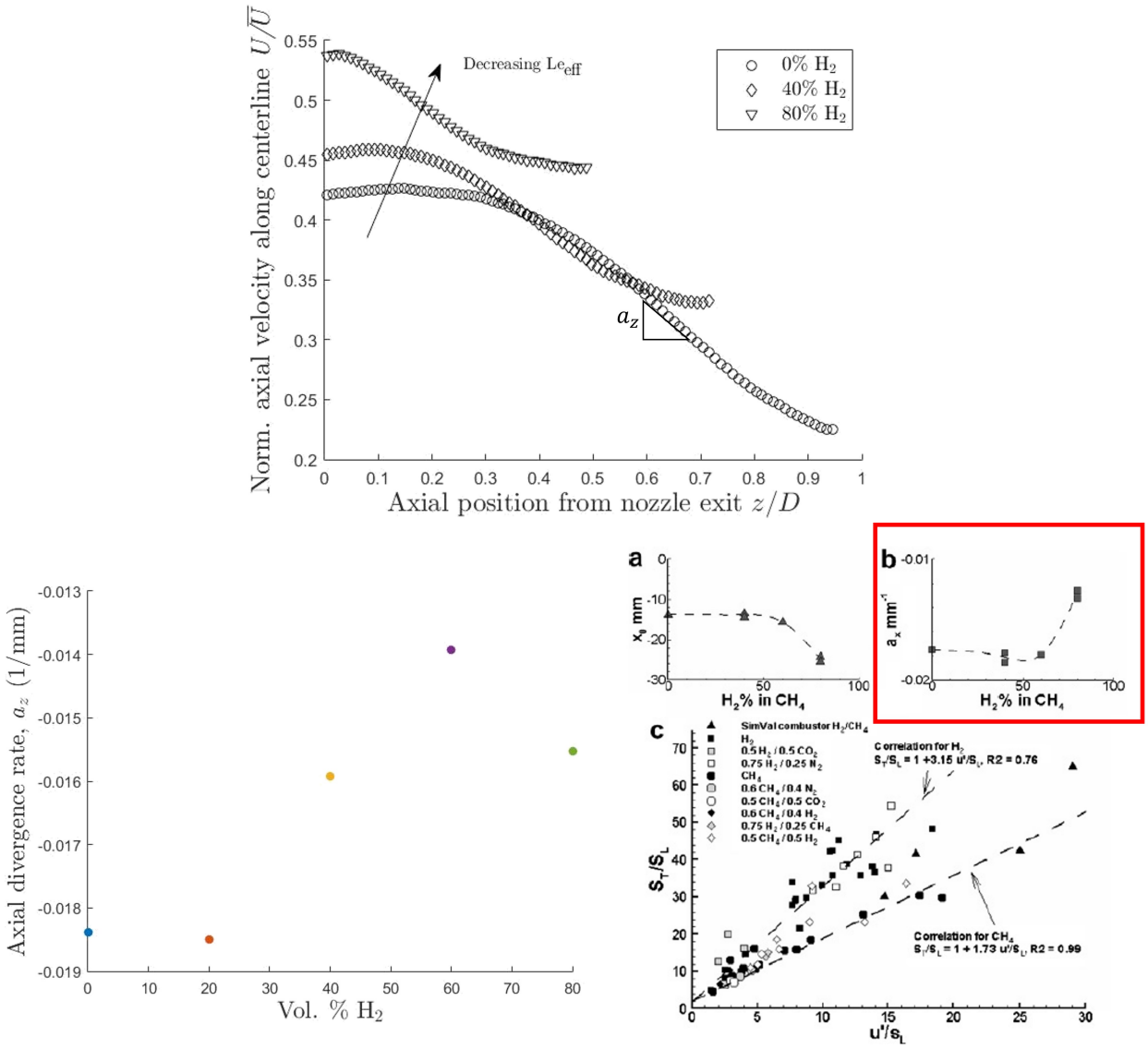

Figure 24: Normalized mean axial velocity profile for select X_{H_2} mixtures evaluated along centerline of burner (top). Estimation of axial divergence rate a_z along centerline for all hydrogen-enriched mixtures in low-swirl flames at McGill (left) and those reported for hydrogen-enriched conditions at STP from Cheng et al., highlighted in red (right).

From Figure 24, the mean axial velocity profiles along the centerline of the burner are plotted against axial position relative to the nozzle exit as a means for determining the axial divergence rate in the conditions evaluated. It is important to note that only the flow deceleration upstream of the flame can be captured due to the vaporization of the PIV seeding particles. The non-dimensional normalized axial divergence rate from the X_{H_2} = 0%, 40% and 80% conditions are -0.397, -0.344 and -0.335 respectively. Since the x-axis is normalized by the nozzle diameter $D = 21.6$ mm, the axial divergence rate can be converted

to a (1/mm) basis by dividing each normalized axial divergence rate by the corresponding diameter. This results in a_z of -0.0184, -0.0159 and -0.0155 (1/mm) divergence rates for X_{H_2} = 0%, 40% and 80% respectively. The increase in axial divergence rate with an increase in hydrogen enrichment is attributed to the response of the flame in closer proximity to faster flows exiting the nozzle. Cheng et al. have reported similar changes in axial divergence rate from their laboratory investigation of hydrogen-enriched mixtures [77]. These findings suggest that even transitioning from low- to high-hydrogen content conditions will lead to similar axial divergence rates and is indicative that low-swirl flames exhibit similar flow behaviour even with different mixture compositions.

3.2 Instantaneous flame location statistics

The axial position of the tracked flame coordinates are recorded relative to the bottom of the imaged frame corresponding to the nozzle exit. As a result, the instantaneous flame location for the 10,000 tracked flame surfaces are plotted in a normalized probability distribution (PD) with a bin size of 0.02 ($\approx 0.5/D_{\text{nozzle}}$). The PDs of instantaneous flame location are calculated for conditions X_{H_2} = 0% - 80% H_2, where the y-axis depicts the normalized probability and the x-axis depicts the normalized axial position of the flame, z/D_{nozzle} (see Figure 25). The PDs of the $X_{H_2} = 0\%$ and $X_{H_2} = 20\%$ conditions are not captured in its entirety due to the instantaneous flame front leaving the FOV of the imaged plane. This was a compromise to ensure the camera had sufficient spatial resolution to resolve the turbulent structures of the flame. The PDs for the instantaneous flame location are also nearly symmetrical such that the mean axial position coincides with the highest probable flame location, or *expected* flame location. As such, the PDs illustrate a consistent horizontal shift to the left denoting lower axial positions with increasing hydrogen enrichment. Essentially, this shift demonstrates that hydrogen-enriched flames will stabilize closer to the nozzle exit. The same phenomenon can also be observed from displacement of the mean flame location from Figures 26-27.

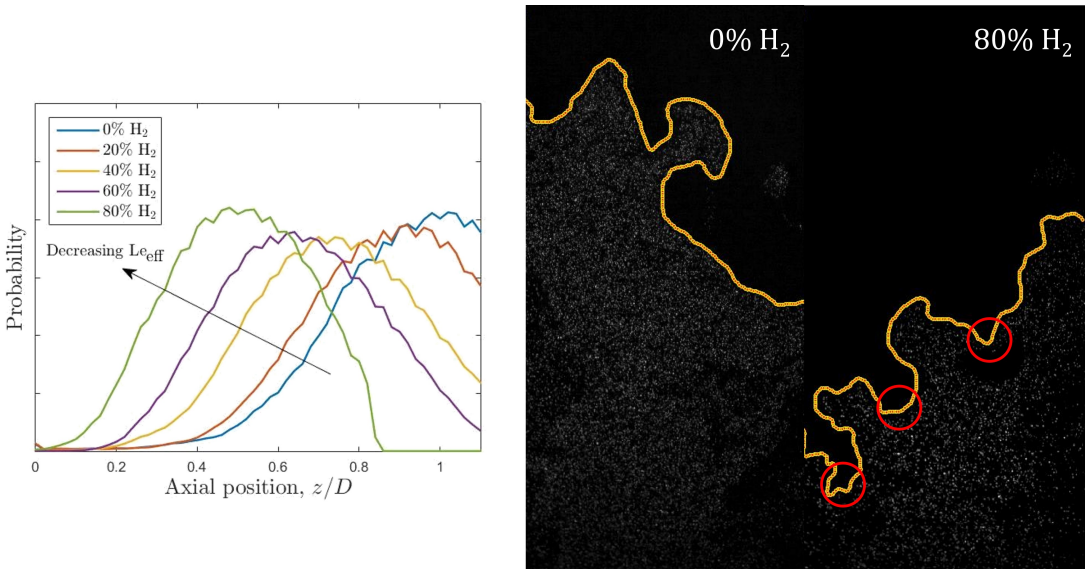

Figure 25: PDs of the instantaneous flame location z/D_{nozzle} relative to nozzle exit for increasing hydrogen enrichment from Mie scattered images (left). Instantaneous flame location for $X_{H_2} = 0\%$ and $X_{H_2} = 80\%$ H_2 condition. Appearance of corrugated, tongue-like structures appear in high-hydrogen mixtures (circled in red).

Cheng et al. have also reported low-swirl flames shifting closer to the nozzle exit with an increase in hydrogen fuel fraction from $X_{H_2} = 40\%$ to $X_{H_2} = 80\%$ [77]. However, the equivalence ratio ϕ is kept constant in their experiments with increasing hydrogen enrichment and so the exhibited shift of the flame's anchoring point closer the nozzle exit is attributed to an increased reactivity. Therefore, it is important to note that while the same effect is observed in this study, the baseline reactivity is kept constant (i.e. S_L constant) with an increase in hydrogen concentration. Salusbury and Abbasi have observed the same effect in a counterflow configuration with hydrogen-enriched propane at fuel-lean conditions at constant reactivity [78][79]. The shift in flame position axially is also quasi-linear with hydrogen enrichment, which not only provides a good feedback mechanism for detecting flashback propensity with hydrogen enrichment, but is also consistent with the momentum balance describing low-swirl flame combustion (see Equation 15). According to this momentum balance, the increase in flame displacement correlates to an increase in the flame displacement speed S_T. However, the bulk velocity U_{av} is also kept constant through each evaluated condition. Since the swirl burner delivers near-equivalent turbulence along the mean flame surface, then the axial velocity fluctuation u' and by extension, the normalized turbulence intensity u_{RMS}/S_L remains nearly constant as well. By isolating against reactivity and turbulence intensity, the dominating parameter responsible for increasing S_T with hydrogen enrichment is the flame stretch rate K, demonstrating the non-negligible influence of differential diffusion.

3.3 Flame surface area and flame surface density statistics

The effect of flame stretch K as a result of differential diffusion contributes to enhanced wrinkling of the turbulent flame surface, even at a constant turbulence intensity, as shown in Figure 25. In this manner, the evolution of the turbulent FSA (i.e. A_{T}) is analyzed in response to hydrogen enrichment and normalized by the mean "laminar" FSA (i.e. A_{L}). The mean FSA contours are obtained by binarizing the mean temperature progress variable field with an edge threshold of 0.5. The resultant image is then Sobel-gradient filtered to delineate the edge of the FSA corresponding to $\overline{c}_{\mathrm{T}} = 0.5$. The number of non-zero pixels comprised in the gradient-filtered image are counted to estimate the approximate laminar flame length A_{L} for each $\%\mathrm{H}_2$ dataset. The mean progress variable fields obtained from Mie scattering are depicted in Figure 26 along with the smoothed, mean flame surface area while those obtained from OH PLIF are depicted in Figure 27. The unsmoothed region near the nozzle exit is due to the filtering effect of Mie scattered images with lower seeding densities. The computed mean FSA lengths are reported from both laser diagnostics techniques in Table 2.

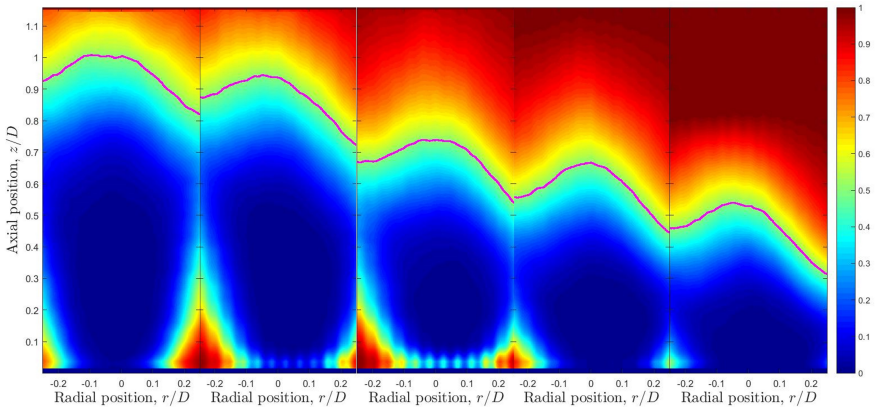

Figure 26: Mean temperature progress variable for $X_{\mathrm{H_2}} = 0$ - 80% (left to right). The $\overline{c}_T = 0.5$ isoline illustrates the mean FSA used to approximate the laminar flame surface area A_{L}.

Table 2: Flame length approximation of the 2-D mean FSA obtained Mie scattering tomography and OH PLIF at a mean progress variable of $\overline{c}_{\mathrm{T}} = 0.5$

$X_{\mathrm{H_2}}$	A_L (from Mie scattering) (mm)	A_L (from OH) (mm)
0	20.296	17.546
20	20.625	16.909
40	20.355	17.727
60	20.975	16.364
80	20.06	15.636

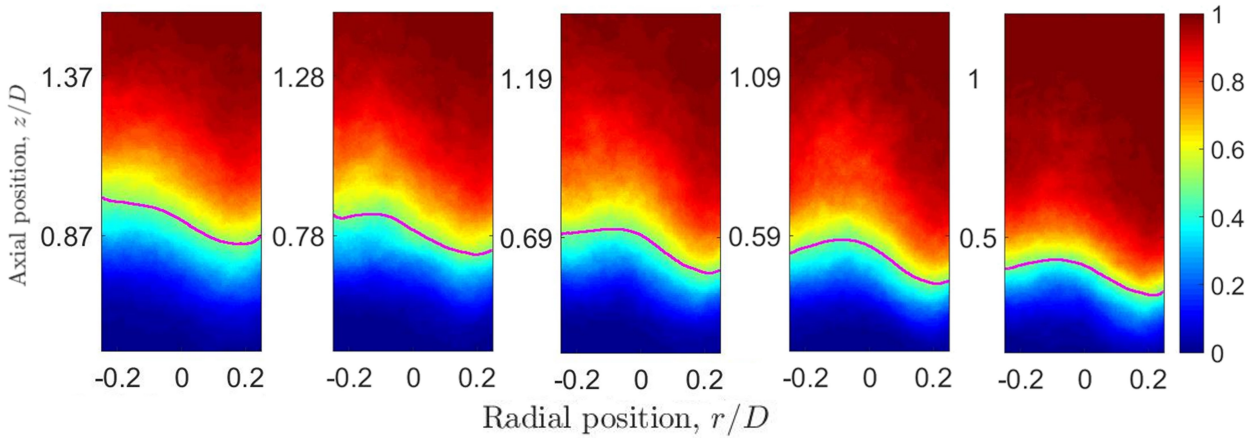

Figure 27: Mean reaction progress variable for X_{H_2} = 0 - 80% (left to right). The $\overline{c}_R$ = 0.5 isoline illustrates the mean FSA used to approximate the laminar flame surface area A_L. Note axial position relative to the nozzle exit decreases

The flame surface area enhancement ($\Sigma = A_T/A_L$) has an important contribution on S_T and can be tracked from frame to frame. The FSA enhancement with hydrogen enrichment can be observed qualitatively from the increasing corrugation and emergence of tongue-like structures from Mie scattering as well as the instantaneous flamefronts extracted from OH PLIF, illustrated in Figure 28. This evolution can also be captured quantitatively by measuring A_T from each frame in their respective dataset. In Figure 29, the PDs of Σ are plotted for both Mie scattering and OH PLIF techniques by considering an equivalent FOV of the flame, -0.25$D_{nozzle} \leq r \leq 0.25D_{nozzle}$.

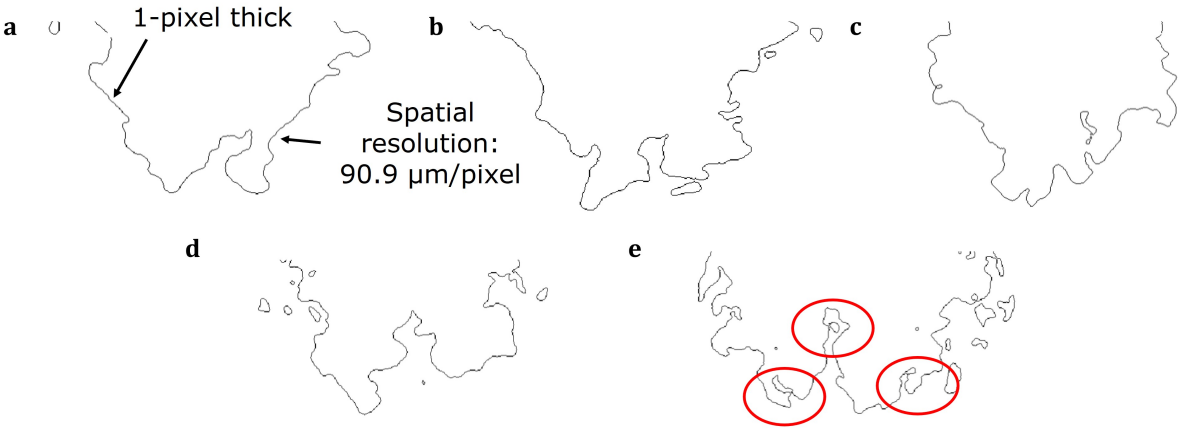

Figure 28: Instantaneous flame images extracted from OH PLIF technique for a) X_{H_2} = 0%, b) X_{H_2} = 20%, c) X_{H_2} = 40%, d) X_{H_2} = 60% and e) X_{H_2} = 80%. The emergence of increasing corrugation at X_{H_2} = 80% is highlighted in red.

The FSA enhancement observed with hydrogen enrichment is evidenced by the linear shift of the PDs towards larger Σ values. Although the scalar value of the mean flame surface areas A_L reported in Table 2 are not equivalent for both experimental campaigns, the peak expected value of Σ for each H_2 dataset remains comparable across both laser diagnostics techniques. However, from OH PLIF, the PDs on FSA enhancement also demonstrate a larger standard deviation, illustrating a higher probability for larger flame surface area with hydrogen enrichment. The reason for higher probabilities of Σ between 3-6 may be due to the ability for the binarized OH image to resolve higher curvatures. Conversely, the lower standard deviations of Σ from binarized Mie scattering images are a result of sharper curvatures being smoothed by Gaussian and median filtering (see Appendix A.4 on uncertainty in flamefront tracking). From the FSA PDs of Mie scattered images in Figure 29, this filtering procedure can only resolve up to $\Sigma \approx 4$. Nevertheless, the increase in Σ demonstrates an enhancement of the flame surface area even if the turbulence intensity and turbulent kinetic energy is kept nearly equivalent across each evaluated condition.

The flame surface density (FSD), defined as the amount of flame surface area generation per unit volume (1/m) also gives an indication of the increased FSA generation with hydrogen enrichment. According to Shepherd's definition [80] of the turbulent burning rate, a larger FSD/Σ is proportional to an increase in the turbulent burning rate. The ensemble-averaged FSD is obtained from the binarized and gradient-filtered OH PLIF images to produce a mean FSD field illustrated in Figure 30. Here, a reduced FOV roughly ≈16 mm from bottom of image plane is considered for each hydrogen-enriched mixture to illustrate the enhancement in FSD primarily at the forefront of the flame.

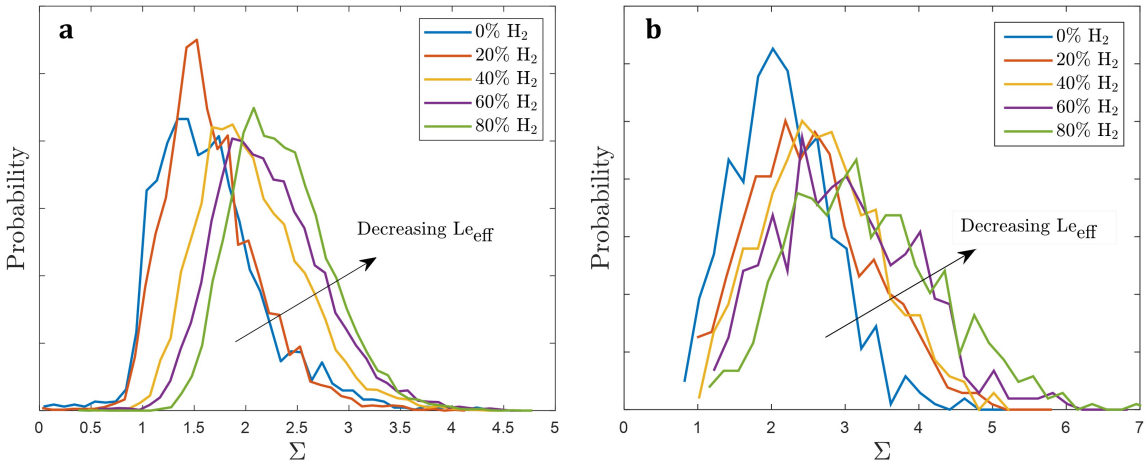

Figure 29: PDs of flame surface area enhancement Σ for increasing hydrogen enrichment from Mie scattered images (left) and OH images (right).

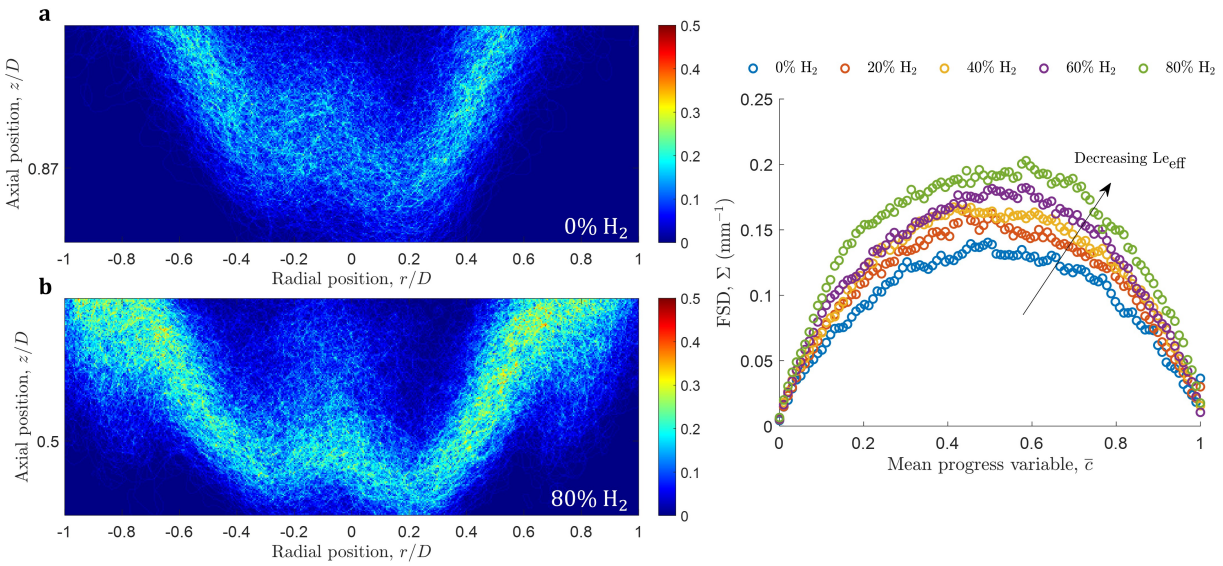

Figure 30: Ensemble-averaged (mean) FSD for a) $X_{H_2} = 0\%$ and b) $X_{H_2} = 80\%$, normalized by its maximum, where color map shows FSD as pixel intensity. Legend situated above plot (right).

From Figure 30, the mean FSD of the flame is correlated against mean progress variable $\bar{c}$. Considering the measured progress variable ranges from $\bar{c} = 0$ (unburned reactants) to $\bar{c} = 1$ (burnt reactants), the average FSD is calculated incrementally with a bin size corresponding to $\bar{c} = 0.01$. Similar plots of FSD to $\bar{c}$ are reported by Hult et al. [81] in their 2D and 3D DNS studies in lean, turbulent hydrogen-air mixtures. As illustrated, hydrogen enrichment leads to an increase in overall FSD along with a skewness of the peak FSD towards a slightly larger mean progress variable $\bar{c}$. The increasing skewness of the FSD profile with decreasing Lewis number can be explained by the formation of cusps towards the products side of the flame ($\bar{c} > 0.5$), a phenomenon which has been reported in V-flames [82] and is also consistent with findings from Trouvé et al. [83] and most recently by Chakraborty [84]. This phenomenon showcases that the increasing effect of differential diffusion plays a considerable role in not only stretching and elongating the flame, but also altering its structure. Ultimately, the enhanced FSA and the trend of larger FSD with hydrogen-enriched mixtures is expected to increase S_T and by extension, the turbulent burning rate $S_{T,LC}$.

3.4 Local flamelet displacement velocity statistics

The local stretch factor I_o, corresponding to an increase in the local flame displacement speed S_T, is hypothesized to be largely influenced by differential diffusion effects as a result of hydrogen's preferential diffusion at the leading points of the flame. The PDs of the S_u velocity component key to calculating S_T is plotted in Figure 31.

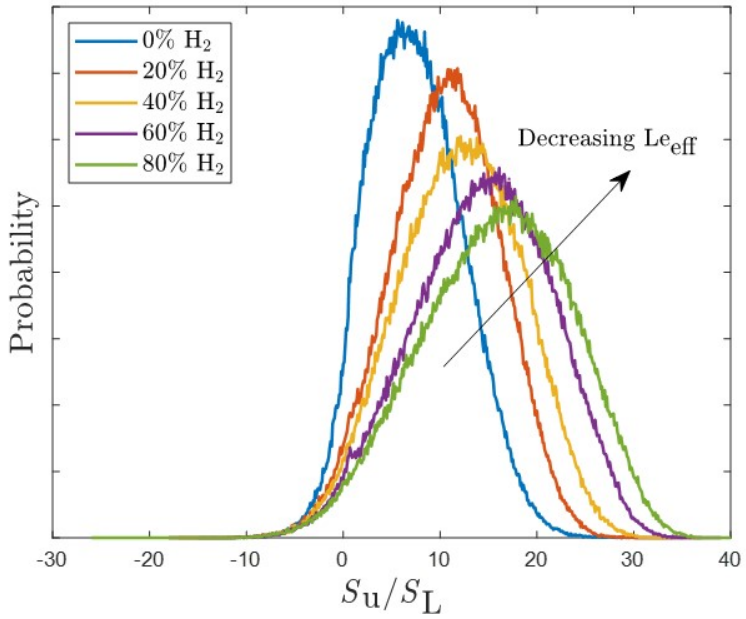

Figure 31: PDs of the convective velocity of the flow (S_u component) with increasing hydrogen enrichment.

The S_u velocities are largely positive considering the convective velocity of the flow moves upward towards the flame, as evidenced by the PDs of S_u in Figure 31. Instances where the convective flow velocity is negative (i.e. defined as vectors pointed away from the flame, $S_u < 0$) are much rarer, lying outside a 1.5 - 2σ confidence interval and may be attributed to an uncertainty on the PIV software in predicting the upward motion of particles at the flamefront. Nevertheless, the PDs of S_u still demonstrate a shift of the expected convective velocity of the flow towards larger values for increasing hydrogen enrichment. This shift is also exemplified by the increased standard deviation and negative skewness of PDs for high-hydrogen content conditions. In general, this behaviour is consistent with a flame stabilizing closer to the nozzle exit where turbulent mean velocities are larger. This phenomenon can also be explained by a flame stabilizing where there is less decay of the turbulent kinetic energy, which seeks to enhance the turbulent FSA (A_T), which in turn increases the turbulent burning rate of the flame.

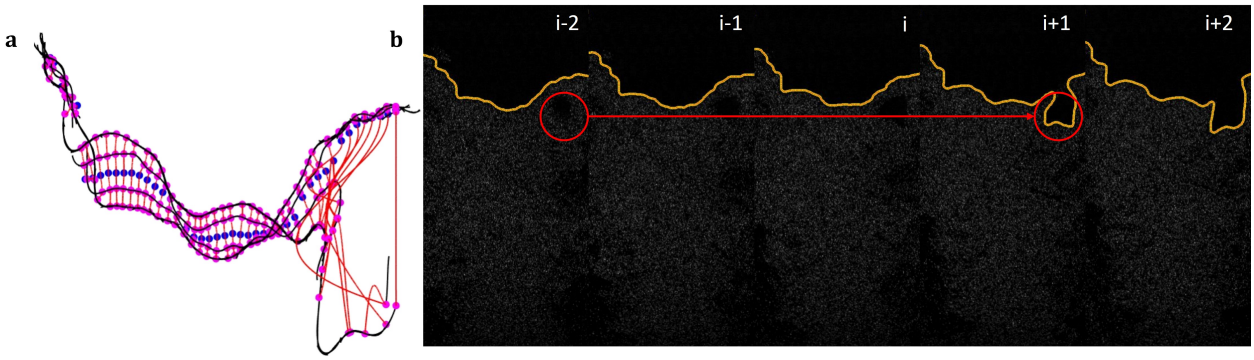

Figure 32: Example of 5 successive flamefronts ($t_{\text{i-2}}$ to $t_{\text{i+2}}$) depicting a) inadequate tracking of flamelet motion due to b) flame "jumping". Example shown is of CH_4-air mixture.

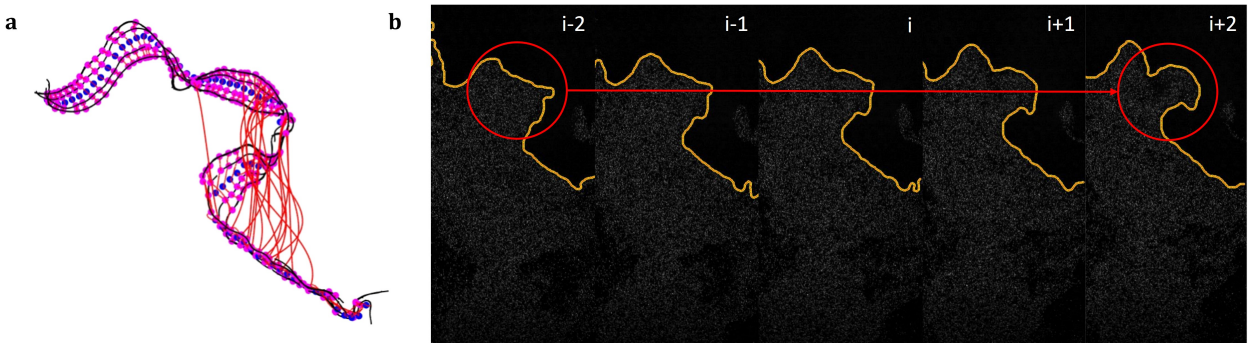

Figure 33: Example of 5 successive flamefronts ($t_{\text{i-2}}$ to $t_{\text{i+2}}$) depicting a) inadequate tracking of flamelet motion due to b) flame "turning". Example shown is of CH_4-air mixture.

From post-processing, a high number of instances have been found where the flamefront exhibits jumping due to the rapid vaporization of atomized oil droplets (see Figure 32) whereas other instances such as turbulence-induced flame turning (see Figure 33) cannot be adequately captured. As a result, it becomes insufficient to track the entirety of the flame front's motion if numerical artefacts persist in the optimization scheme used to correlate flame grid points between successive flame fronts. Therefore, this approach has been modified to evaluate only the leading point of the flame towards resolving the flamelet velocity S_{F} component of the local flame displacement velocity S_{T}.

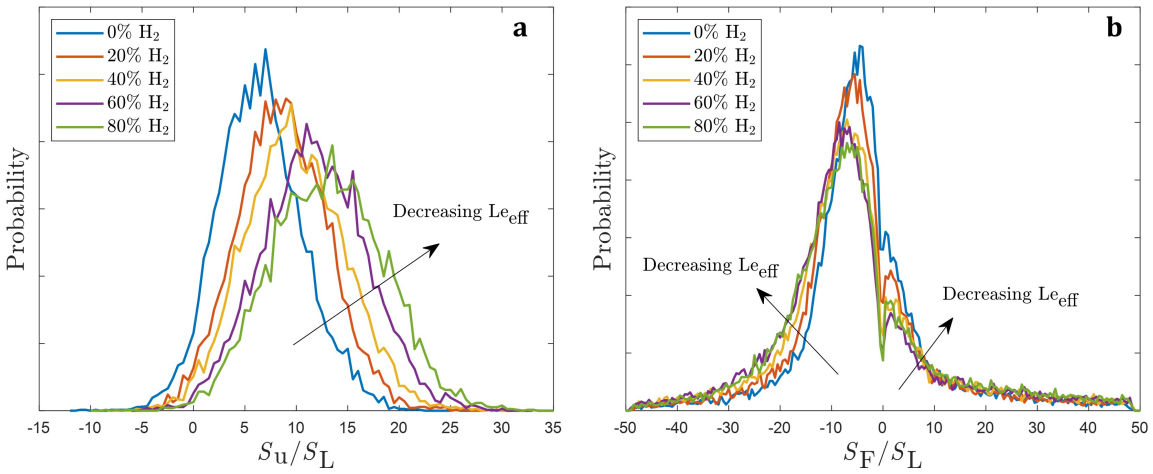

Figure 34: PDs of a) the local convective velocity of the flow S_u and b) flamelet velocity S_u at the leading point of the flame (i.e. closest grid point axially relative to the nozzle exit).

The PDs of S_u and S_F characterizing the local velocities of the flamelet at the leading point are plotted instead in Figure 34. As expected, the PDs of the S_u velocity component along the leading point exhibit the same shift towards larger values as those referenced in Figure 31, which capture the convective velocity along entirety of the flamefront. Conversely, there is not a marked shift of the S_F PDs towards positive velocities, but rather a slightly larger probability of negative S_F values with H_2 enrichment. This phenomenon can be interpreted as the flamelet moving away from the nozzle and rapidly accelerating, as depicted in Figure 35. The enhanced vaporization of the oil droplets could also be due to the out of plane motion of the swirling flow, which becomes stronger as the flame displaces closer to the nozzle exit with hydrogen enrichment. The increasing flamelet motion is also consistent with the flame stabilizing closer to the nozzle exit where higher local turbulence has a larger influence on perturbing the flamefront. In turn, this enhanced perturbation serves to distort and stretch the flame surface further, effectively promoting larger flamelet velocities. This suggests that the flame displacement in response hydrogen enrichment has a dual effect on both components of the local flame displacement speed. The flame "jumping" phenomenon occurs more frequently with hydrogen enrichment, but considering it is an artifact of flamelet motion tracking means that larger positive S_F velocities would not be captured as frequently in the PDs of the S_F velocity component.

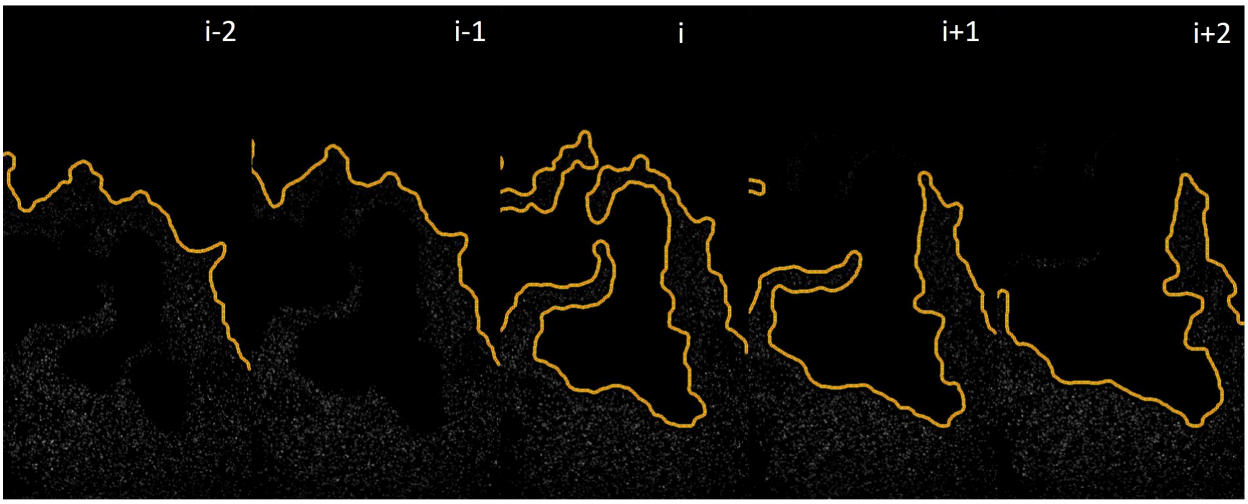

Figure 35: Example of 5 successive flamefronts ($t_{\text{i-2}}$ to $t_{\text{i+2}}$) depicting rapid acceleration of leading point's flamelet motion due to larger vaporization of atomized oil droplets. Example shown is of 80% H_2-20% CH_4-air mixture.

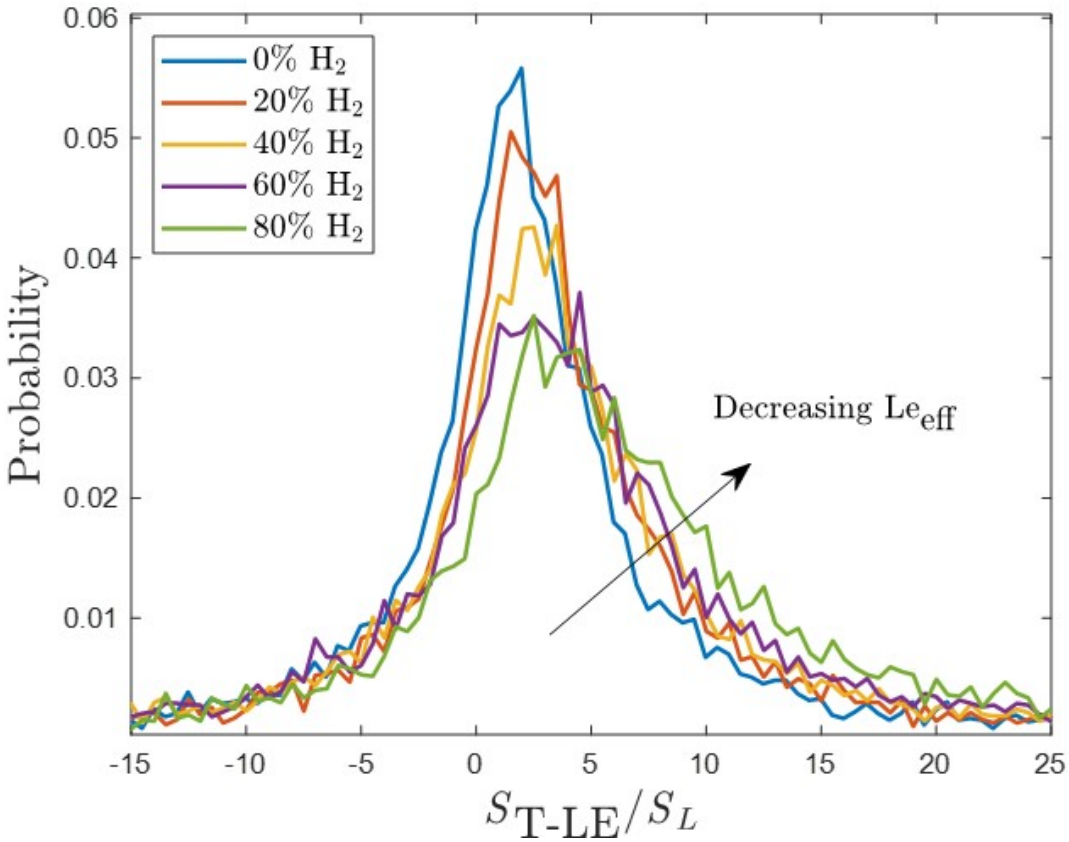

Figure 36: PDs of the local flame displacement speed S_{T} corresponding to the local stretch factor, I_{o} at the leading point.

The summation of the S_u and S_F velocity components at each grid point along the flamefront are represented by the PDs of S_T in Figure 36. In this summation, the directionality of the convective velocity (i.e. positive S_u towards flame, negative S_u if away) and the flamelet velocity (i.e. positive S_F moving towards reactants, negative S_F if away) are considered in the computation of the local flame displacement speed at each flame grid point. From these PDs, it is possible to obtain a "negative" turbulent flame speed if for an instant, flame grid points move locally away from the nozzle and whose motion is larger than the convective velocity at those flame grid points. Nevertheless, the S_T being largely positive demonstrate that any negative flamelet motion is largely dominated by the positive convective velocity S_u coming into the flame. At the $X_{H_2} = 0\%$ condition, the mean value for the local stretch factor $I_o = S_T/S_L$ is approximately 3.24 while the mean I_o for the $X_{H_2} = 80\%$ condition is as much as 7.81. The increase in local stretch factor with hydrogen enrichment is also evident by the shift in mode (i.e. peak) values of S_T/S_L towards larger values. Since Σ and I_o both increase as the hydrogen concentration increases, then the turbulent burning rate $S_{T,LC}$ must increase as well, even while maintaining a constant baseline reactivity and near-constant turbulence intensity with hydrogen enrichment. The considerable increase in local flame displacement speed from 3.24 to 7.81 highlights the degree that differential diffusion affects the turbulent burning rate of hydrogen-enriched mixtures.

3.5 Local strain rate and curvature statistics

While an increase in the local flame displacement speed and the turbulent burning rate can be correlated to differential diffusion effects, further analysis is required on the components of flame stretch responsible for its increase. For instance, the influence of flame stretch can be inferred from Figure 37, which depicts the evolution of the turbulent flame brush thickness δ_T derived from the OH PLIF mean progress variable fields. The turbulent flame brush thickness is computed by calculating the distance of the $\overline{c} = 0.1$ and $\overline{c} = 0.9$ isolines relative to the $\overline{c} = 0.5$ isoline. It is evident both qualitatively and quantitatively that the turbulent flame thickness decreases with hydrogen enrichment. However, prior analysis of mean FSD has demonstrated that Σ enhances with hydrogen enrichment. Therefore, the increased FSA within a smaller flame brush thickness must mean that there is an increase in flamefront curvature κ. The mean of the curvature PD from each dataset is considered in Figure 38.

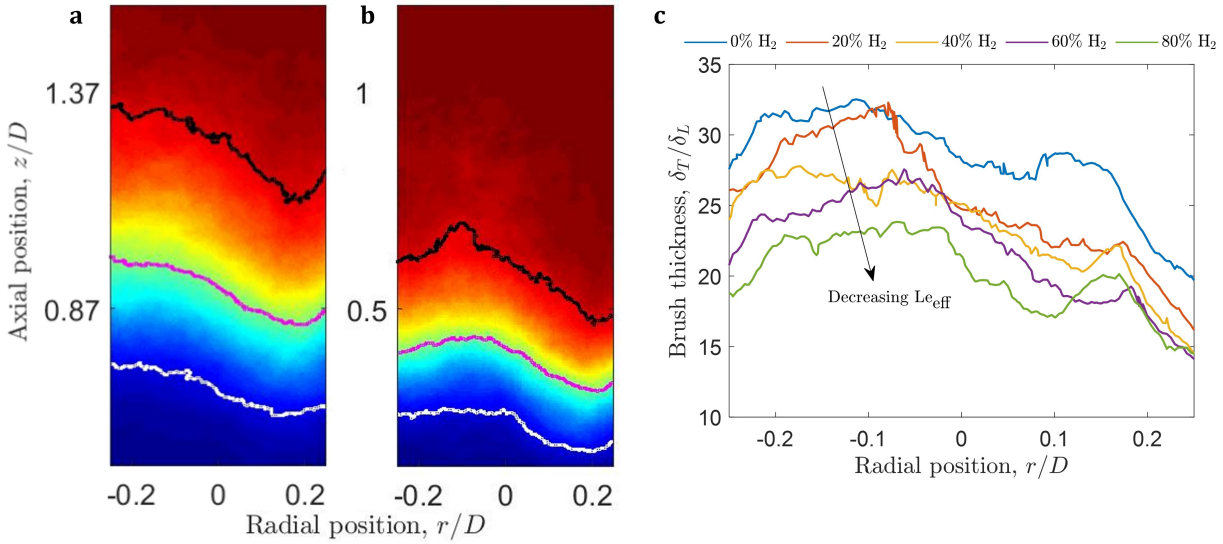

Figure 37: Mean progress variable fields for a) X_{H_2} = 0% and b) X_{H_2} = 80% conditions depicting progress variable isolines at $\overline{c}$ = 0.1 (white), 0.5 (purple) and 0.9 (black). Radial profiles of c) the turbulent flame brush thickness normalized by the laminar flame thickness δ_T/δ_L for all evaluated conditions.

The mean curvature from PDs of κ is plotted against effective Lewis number for each evaluated condition. From the scatter plot, values of mean curvature straddle the $\kappa = 0$ line. This can be interpreted by κ PDs which are symmetric about $\kappa = 0$ and is consistent with findings from Abbasi et al. that DL instabilities do not dominate at higher turbulence intensities [85]. This is also indicative that there are both equally negative and positive curvatures as the flame becomes more stretched. However, the larger standard deviation for lower effective Lewis numbers means that there are higher probabilities for negative and positive local curvatures with hydrogen enrichment. Therefore, an analysis is done instead on the mean positive curvature to indicate if there is a development of positively curved flamelets associated with the leading points hypothesis. From Figure 38, the mean positive curvature increases below an effective Lewis number of 0.7, which corresponds to the X_{H_2} = 40% condition. As hydrogen concentration increases past 50% fuel fraction, differential diffusion effects influence the flame topology such that larger curvatures are more prevalent. As expected, this behaviour of increased curvature is consistent with larger FSA generation within a decreasing flame brush thickness. Therefore, the increased local curvature is responsible for stretching the flame, increasing the local flame displacement speed and increasing the turbulent burning rate. However, the flame stretch rate is comprised of two components which both contribute to corrugation along the flamefront: the curvature κ and the hydrodynamic tangential strain on the flame induced by the bulk flow, $K_{s,t}$. The components

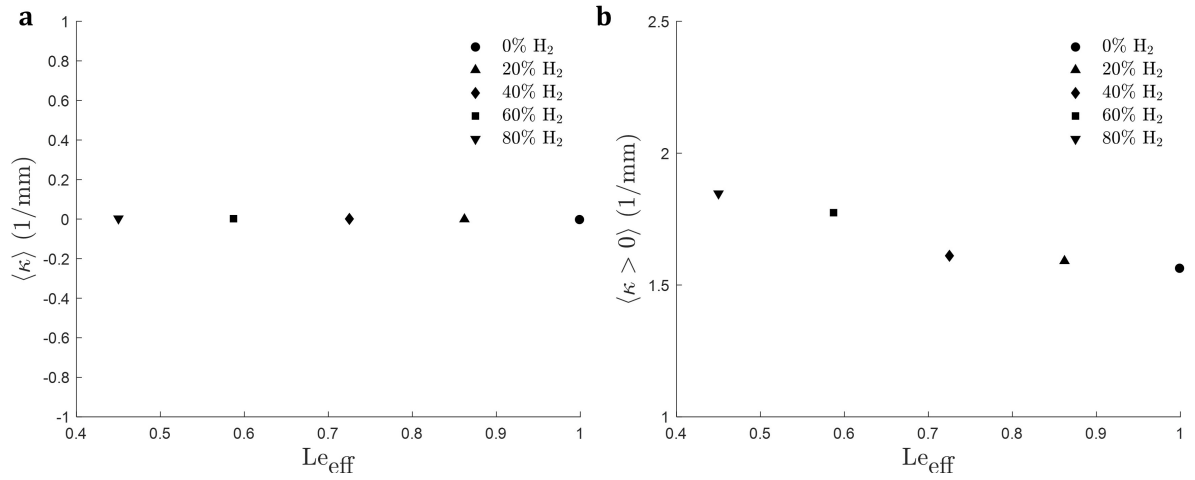

Figure 38: Mean curvature $\langle\kappa\rangle$ (left) and mean positive curvature $\langle\kappa > 0\rangle$ (right) correlated against effective Lewis number $\mathrm{Le}_{\mathrm{eff}}$.

of flame stretch are also extracted locally along the flamefront, where the mean value from PDs of κS_{T} and $K_{\mathrm{s,t}}$ are plotted in Figure 39. From Figure 39, it is important to note the magnitude of the vertical axis from both contributions of flame stretch rate. The combining influence from curvature and the local flame displacement speed is ≈ 7 times larger than that from the hydrodynamic tangential strain experienced by the flow field.

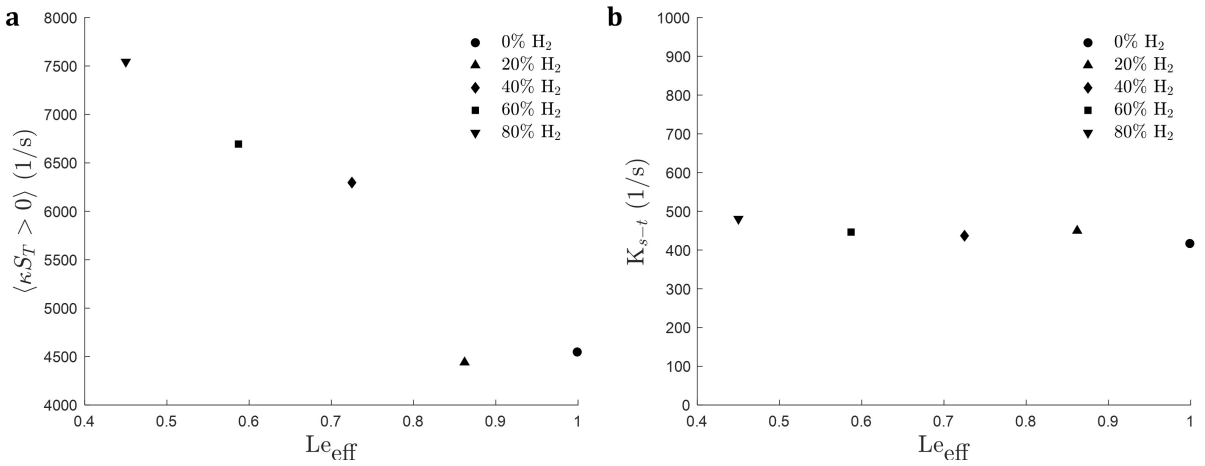

Figure 39: At the leading point, a) mean of the positive curvature component κS_{T} (left) and b) mean of the positive hydrodynamic tangential strain component $K_{\mathrm{s,t}}$ (right) of the flame stretch rate K plotted against effective Lewis number, $\mathrm{Le}_{\mathrm{eff}}$. Note difference in scale on the y-axis of both plots.

The contribution from the curvature component of flame stretch K is expected to increase and agrees with the increasing positive, mean curvature observed at lower Lewis numbers. Meanwhile, the influence from the tangential strain component remains relatively stagnant.

This demonstrates that the turbulent flow field does not significantly alter the stretch behaviour of the flame, particularly because the bulk velocity is kept constant across each condition. Therefore, the increased flame stretch as a result of hydrogen enrichment can be largely explained by increasing curvature towards enhancing the local flame displacement speed.

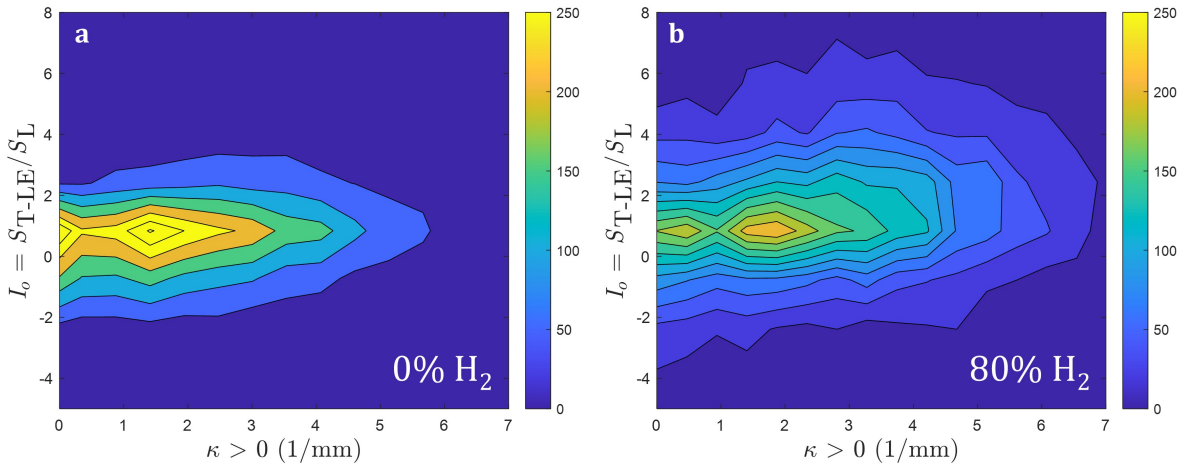

Figure 40: Contour plots of the local flame displacement speed enhancement $I_o = S_T/S_L$ at the leading point correlated against positive curvature at leading point for a) $X_{H_2} = 0\%$ H_2 and b) $X_{H_2} = 80\%$ H_2 conditions.

The correlation between local flame displacement speed and increasing curvature are interrelated since an increase in flame stretch rate will increase S_T. In Figure 40, the contour plots at $X_{H_2} = 0\%$ H_2 and $X_{H_2} = 80\%$ H_2 demonstrate a synergistic increase in local flame displacement speed as a result of larger positive curvatures. Therefore, the increase in curvature as a result of hydrogen addition is the dominating mechanism behind the increase in turbulent flame speed and the turbulent burning rate.

3.6 Turbulent burning rate

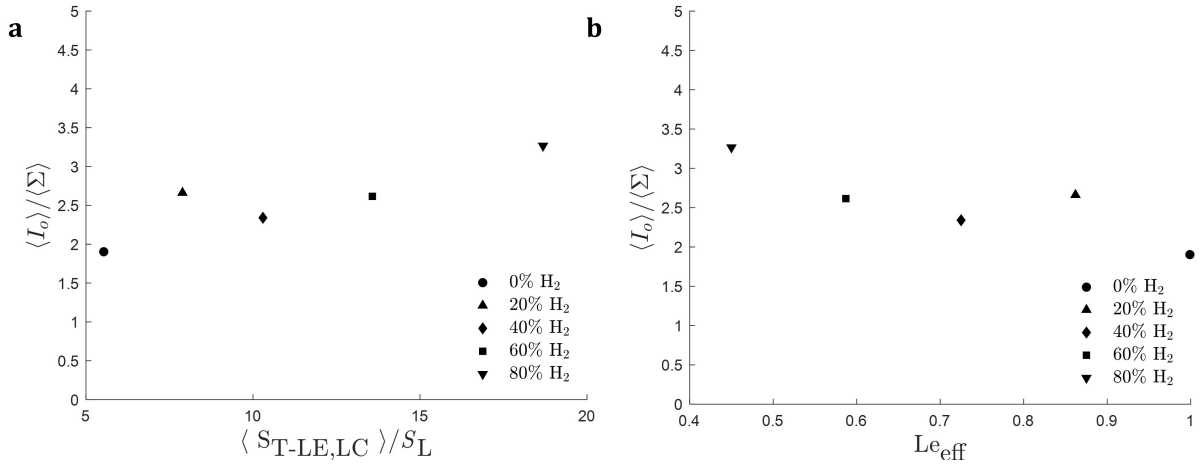

Figure 41: Mean local flame displacement speed enhancement $\langle I_{\text{o}} \rangle = S_{\text{T}}/S_{\text{L}}$ at leading point normalized by mean flame surface area enhancement $\langle \Sigma \rangle = A_{\text{T}}/A_{\text{L}}$, correlated against the mean normalized turbulent burning rate $\langle S_{\text{T,LC}} \rangle / S_{\text{L}}$ (left) and against effective Lewis number Le_{eff} (right).

The turbulent burning rate is estimated as the mean of the PDs of I_{o} and Σ, respectively. In Figure 41, the relative contribution between I_{o} and Σ are weighed against the turbulent burning rate. With hydrogen enrichment and a decreasing effective Lewis number, the average of the relative contribution between I_{o} and Σ is ≈ 2.6. This results in a I_{o} relative contribution of 72% compared to 28% from FSA generation Σ. However, this relative contribution may be skewed towards larger values since only effective Lewis numbers < 1 are considered in this study, where I_{o} is expected to be more prevalent. Similar to experiments designed by Abbasi et al. [85], it is believed that the ratio between I_{o} and Σ may stagnate towards a constant value for mixtures with higher Lewis numbers even in low-swirl combustion. However, it is important to note that the mean ratio $\langle I_{\text{o}} \rangle / \langle \Sigma \rangle$ reported here is still larger than 1 even for a mixture close to unity Lewis number.

4 Conclusion

4.1 Discussion of results

In this thesis, the fuel volume fraction of H_2 relative to CH_4 (i.e. X_{H_2}) was increased in mixtures with constant S_L and constant U_{av} in an effort to isolate differential diffusion effects with hydrogen enrichment. One of the primary impacts of hydrogen addition to fuel-lean methane-air mixtures was the axial displacement of the low-swirl flame closer to the nozzle exit, as observed qualitatively and quantitatively from both experimental campaigns, demonstrating the flame stabilizing in a region with larger convective flow velocities. Given the low-swirl flame stabilizes against an opposed flow where the local flame speed matches the local velocity, the axial displacement must correlate to an increase in the turbulent flame speed, by Equation 15. This behaviour suggests a stronger correlation to fuel composition effects as a result of hydrogen addition even at moderate turbulence intensities. Cheng et al. characterized the turbulent flame speed enhancement in low-swirl flames by introducing an empirical constant to describe the proportionality between S_T/S_L and u_{RMS}/S_L, determined to be $K = 1.73$ in fuel-lean CH_4 mixtures and $K = 3.15$ in fuel-lean H_2 mixtures [77]. From these findings, the difference in empirical constants for fuel-lean-air mixtures at equivalent turbulence intensities is also indicative that S_T enhancement is strongly correlated to the fuel composition (i.e. thermodiffusive effects).

Another impact of hydrogen addition is the increase in flame surface area enhancement A_T/A_L coupled with the decrease in the turbulent flame brush thickness δ_T of the low-swirl flame. This coupling effect serves to concentrate the FSA generation such that FSD increases with hydrogen enrichment. The trend of increasing FSD with hydrogen enrichment, which is also reported in Emadi et al.'s study of low-swirl hydrogen-enriched flames [86], promotes an increase in the turbulent flame speed by means of increasing the burning rate. It is important to recall the evaluated mixtures in this study describe flames within the BPTRZ regime, which suggests turbulent diffusion whose turbulence scale is larger than the laminar flame thickness δ_L wrinkle the flamefront towards increasing the turbulent flame speed. However, the influence of differential diffusion is still prevalent for higher turbulence intensities in the flamelet regime, which corroborates the increase in local flame displacement speed observed in this study and that observed by Wu et al. for larger Reynolds number flows [87].

The larger FSD generation and enhancement of the local flame displacement speed with hydrogen enrichment has prompted an analysis of local flame stretch effects to determine the leading mechanism enhancing the turbulent burning rate. This analysis involves extracting the components of flame stretch rate K (i.e. curvature and hydrodynamic tangential strain

components) locally along the flamefront. The influence of the hydrodynamic tangential strain component, synonymous with the strain induced by the bulk flow, was expected to be similar across for all mixtures considering the equivalent bulk velocity boundary condition. In this case, the product of the curvature and local flame displacement speed component (i.e. κS_{T}) for flame stretch shows a monotonically increasing trend with decreasing Lewis number. The κS_{T} term describes the coupled effect between flame stretch and flame propagation behaviour becoming stronger as thermodiffusive effects become more prevalent with hydrogen addition. DNS studies characterizing thermodiffusive instabilities in fuel-lean, premixed hydrogen flames in a slot burner configuration also demonstrate the synergistic interaction in this term exacerbated by differential diffusion [88]. In their simulation, the κS_{T} term, which is most pronounced in regions of larger positive curvature, correlates strongly to an enhanced local reactivity in thermodiffusively-unstable flames (i.e. $\mathrm{Le}_{\mathrm{eff}} < 1$), leading to larger local burning rates. Nevertheless, the enhancement in local flame displacement speed or I_{o}, does not necessarily occur at the most positively curved regions, or leading points of the flame. Marshall et al.'s study in high-hydrogen content, low-swirl flames have attempted to characterize if the curvature at the leading points are controlling the turbulent burning rate enhancement [89]. Their findings, which illustrate an almost negligible change in leading point curvature with hydrogen addition, suggest it might be a global effect of increasing curvature rather than a local effect at the leading points towards increasing the turbulent burning rate. Further analysis is required to validate the leading points concept towards modelling flame stretch effects in response to differential diffusion.

The local stretch factor I_{o}, defined in this study as $S_{\mathrm{T}}/S_{\mathrm{L}}$ also differs from literature, as mentioned in Driscoll's review paper on turbulent premixed combustion [90]. The definition of the stretch factor is based on the normalized local flamelet consumption speed $S_{\mathrm{F,LC}}/S_{\mathrm{L}}$ instead of the normalized local flame displacement speed $S_{\mathrm{T}}/S_{\mathrm{L}}$. This adopted definition of the stretch factor introduces the turbulent Markstein number Ma_T (I_{o} = 1 - $\mathrm{Ma}_T f(K)$) analogous to the laminar Markstein number Ma_L, which is dependent on Markstein length $\mathcal{L}$. Considering the relationship between Markstein length and number to flame stretch effects, a thermodiffusively stable mixture ($\mathrm{Le} \geq 1$) is expected to result in Markstein numbers near zero for both the laminar and turbulent conditions such that $I_{\mathrm{o}} \approx 1$. However, it is important to note that the definition of I_{o} used in this study based on S_{T} results in $\langle I_o \rangle > 1$ even for near-unity Lewis numbers where mixtures are expected to be thermodiffusively stable. In this respect, it is more amenable to examine the modal (i.e. expected) value of I_{o} extracted from the S_T PDs at $X_{\mathrm{H_2}} = 0\%$. The peak value of the PDs of $S_{\mathrm{T-LE}}/S_{\mathrm{L}}$ occurs at $\approx$ 1-2 and is somewhat close to I_{o} approximations made in the literature.

The development of local extinction spots with hydrogen enrichment is recognized in

this study. Nevertheless, the appearance of such local extinction in regions of large negative curvature, as predicted by DNS studies for fuel-lean hydrogen-air mixtures [50] cannot be adequately captured through developed flame surface tracking techniques from Mie scattering of oil droplets. This phenomenon cannot be captured for two reasons: 1) there is ambiguity from the oil droplet vaporization if a flame is locally extinguishing or not and 2) there is an inherent limitation by the Pavlidis contour tracking algorithm such that it requires a continuous contour to be tracked and cannot resolve regions where the flame locally extinguishes, or cusps. Furthermore, increasingly negative curvatures associated with cusp formation and flame extinction are more prone to being filtered in the curvature analysis, which is limited to a curvature $\kappa = 0.295$ [1/pixel] or $\kappa = 10$ [1/mm] (equivalent to a radius of 3.39 pixels). Therefore, analysis of the flame topology for hydrogen enriched mixtures is better characterized by instantaneous OH-PLIF, which also serves to capture the formation of flame pockets aside from the flamefront.

4.2 Summary of results

The key results of this thesis work on differential diffusion effects in fuel-lean, hydrogen enriched low-swirl flames are summarized by two primary findings:

1) The low-swirl flame experiences a monotonically increasing, mean axial displacement towards the nozzle exit with hydrogen enrichment. The momentum balance characterizing low-swirl flame stability demonstrates the relationship between increasing axial displacement and increasing turbulent flame speed. The increase in turbulent flame speed as a response to hydrogen enrichment is evident even in mixtures at constant reactivity and near-constant turbulence intensity, demonstrating the influence of differential diffusion effects.

2) The ratio between local stretch factor $I_o = S_T/S_L$ and FSA enhancement Σ has been correlated against the mean turbulent burning rate, defined by Driscoll [90] to include stretch sensitivity effects as a result of differential diffusion. The relative contribution between I_o and Σ has been found to be 72% and 28% respectively. This finding, which is in close agreement with Abbasi in their analysis of counter-flow flames [54] suggests there may be a universal relationship to predict the turbulent burning rate in response to differential diffusion effects across various burner geometries for low-Lewis number mixtures.

4.3 Future work

The analyses undertaken in this study are largely made from a 2-D transversal cross section of the low-swirl flame. While the 2D-3C velocity field is resolved using stereo PIV techniques,

the out-of-plane velocity component does not provide sufficient information past the vorticity, $2\times\omega$ in the shear layers and the azimuthal velocity w. However, spatially resolving the flame surface area in all directions using time-resolved 3D PLIF techniques could provide valuable insight on FSA generation Σ and turbulent-flame interactions such as local extinction to validate DNS and LES simulation of low-swirl flames with hydrogen enrichment. An example of this level of analysis has been performed by Trunk et al. using a sophisticated laser diagnostics setup to image OH PLIF in two parallel planes coupled with S-PIV to extract the 3D local flame displacement speed [91].

Conversely, the simultaneous OH and CH_2O PLIF techniques mentioned in this work can be extended to extract and correlate the relative heat release rate (HRR) against curvature along the flamefront. This correlation has been accomplished by Fan et al. on flame wall interactions of fuel-lean hydrogen-air mixtures at the NRC [92]. In the context of characterizing differential diffusion effects, the joint distribution between HRR and positive curvatures would provide further insight into the enhanced reactivity exhibited at the forefront of thermodiffusively-unstable flames, as described by DNS studies from Berger et al. [88]. A comparative analysis on the relative HRR between the turbulent inner axial and high-velocity outer swirling flow of a low-swirl flame can also provide further information on the dynamics of flame stability.

The low-swirl injector (LSI) and turbulence-generating plate (TGP) designed in this study can also be exchanged for different geometries. In this manner, a characterization of differential diffusion effects across different geometries can be done to validate hydrogen enrichment as purely a Lewis number effect and not a geometry effect. The use of different geometries also permits the possibility to examine hydrogen enrichment across different bulk velocities and different turbulence intensities. The characterization of flame structure by PLIF/PIV techniques can be used to further validate premixed combustion regimes in the Borghi diagram. Since only the center core flow was analyzed locally in this study, this work can be extended to characterize local phenomena in the shear layers of the low-swirling flow as well where velocities and turbulence intensities are larger.

Lastly, the dependence of differential diffusion effects on the Lewis number in a low-swirl configuration can be used to predict the behaviour of other fuel blends closer to industrial practice such as syngas (H_2 and CO) for the same configuration. The volume-based effective Lewis number of a syngas mixture can be coupled to a flamelet model generally used in CFD simulations to better predict combustion behaviour of low-swirl flames such as its turbulent flame speed, its heat release rate and its combustion emissions. Given the increasing capabilities of laser diagnostics techniques today, new questions can be posed in regards

to the behaviour of premixed low-swirl turbulent combustion. Experimental work geared towards resolving smaller scales of turbulence remains an important step in the development of thermochemical models able to capture the physics of turbulent-flame interactions, which in turn would improve the design tools for developing fuel-flexible gas turbines.

A Appendices

A.1 Geometric derivation of swirl number

The swirl number for a fixed-vane configuration can be re-derived from Eq. 14. Since the azimuthal velocity (w) is kinematically related to the axial velocity (u) by the vane angle $\tan\alpha = u/w$, the axial flux of linear momentum (G_x) and axial flux of angular momentum (G_ang) can be represented as follows:

$$G_\mathrm{ang} = 2\pi\rho \int_{R_\mathrm{c}}^{R_\mathrm{b}} u_\mathrm{a}(u_\mathrm{a}\tan\alpha) r^2\, dr = 2\pi\rho u_\mathrm{a}^2 \tan\alpha \frac{R_\mathrm{b}^3 - R_\mathrm{c}^3}{3} \tag{25}$$

$$G_\mathrm{x} = 2\pi\rho \int_{R_\mathrm{c}}^{R_\mathrm{b}} u_\mathrm{a}^2 r\, dr + 2\pi\rho \int_{0}^{R_\mathrm{c}} u_\mathrm{c}^2 r\, dr = \pi[\rho u_\mathrm{a}^2(R_\mathrm{b}^2 - R_\mathrm{c}^2) + \rho u_\mathrm{c}^2 R_\mathrm{c}^2] \tag{26}$$

Similar to Eq. 16, R_b represents the radius of the burner from the center to the outer plenum and R_c represents the radius of the inner plenum. Since the azimuthal velocity is a function of the axial velocity by the vane angle, the axial velocity is broken down to two components to distinguish axial velocity through the inner plenum (u_c) and through the annulus in the outer plenum (u_a). The density ρ is assumed constant and is equivalent in both inner axial and outer annulus flows given the same premixed mixture is flowing through both channels. Therefore, the swirl number is taken as the ratio of the momentum fluxes:

$$S = \frac{2\pi\rho u_\mathrm{a}^2 \tan\alpha \frac{R_\mathrm{b}^3 - R_\mathrm{c}^3}{3}}{R_\mathrm{b}\pi[\rho u_\mathrm{a}^2(R_\mathrm{b}^2 - R_\mathrm{c}^2) + \rho u_\mathrm{c}^2 R_\mathrm{c}^2]} \tag{27}$$

From this expression, the density and the constant π cancel each other while the terms R_b and u_a^2 can be factored from the numerator and denominator respectively. This simplifies the formula to the following:

$$S = \frac{\frac{2}{3} u_\mathrm{a}^2 R_\mathrm{b}^3 \tan\alpha (1 - R^3)}{R_\mathrm{b} u_a^2 R_\mathrm{b}^2 [(1 - R^2) + \frac{u_\mathrm{c}^2}{u_\mathrm{a}^2} R^2]} \tag{28}$$

Additional terms u_a^2 and R_b^3 can be cancelled from the numerator and denominator such that R represents the ratio of the burner and centerbody radii ($R_\mathrm{c}/R_\mathrm{b}$). Furthermore, the square of the velocity ratio $u_\mathrm{c}^2/u_\mathrm{a}^2$ can be represented as a function of the mass flux ratio m between the flow in the centerbody and the annulus and the burner to centerbody radii ratio, R. The mass flux ratio is:

$$m = \frac{\rho u_\mathrm{c} A_\mathrm{c}}{\rho u_\mathrm{a} A_\mathrm{a}} = \frac{u_\mathrm{c} A_\mathrm{c}}{u_\mathrm{a} A_\mathrm{a}} \tag{29}$$

Therefore, re-arranging terms and squaring both sides of the equation gives the following expression for the square of the velocity ratio:

$$m^2 \frac{A_a^2}{A_c^2} = \frac{u_c^2}{u_a^2} = m^2 \frac{\pi^2 (R_b^2 - R_c^2)^2}{\pi^2 R_c^4} = m^2 \frac{(1 - R^2)^2}{R^4} = m^2 (1/R^2 - 1)^2 \tag{30}$$

Substituting the above expression into Eq. 28 yields the geometric representation of the swirl number outlined in section 2.1. However, in regards to the controllable swirl burner used in this thesis project, the thickness between the centerbody and the annulus (2 mm) is non-negligible. For the integrals in Eqs. 25-26 used to denote the annular section, the lower and upper limits, R_c and R_b represent the area radially between the inner plenum's *outer* wall to the outer plenum's *inner* wall. However, for the integrals in Eqs. 25-26 used to denote the centerbody section, the upper limit R_c represents the area radially between the center of the burner to the inner plenum's *inner* wall. In brief, the geometric areas of the inner and outer plenum are 0.00008229 m^2 and 0.00020719 m^2 respectively, while the nozzle exit area is 0.000366 m^2. The plenum areas do not equal the nozzle exit area because of the area attributed to wall thickness.

A.2 Swirl burner design details

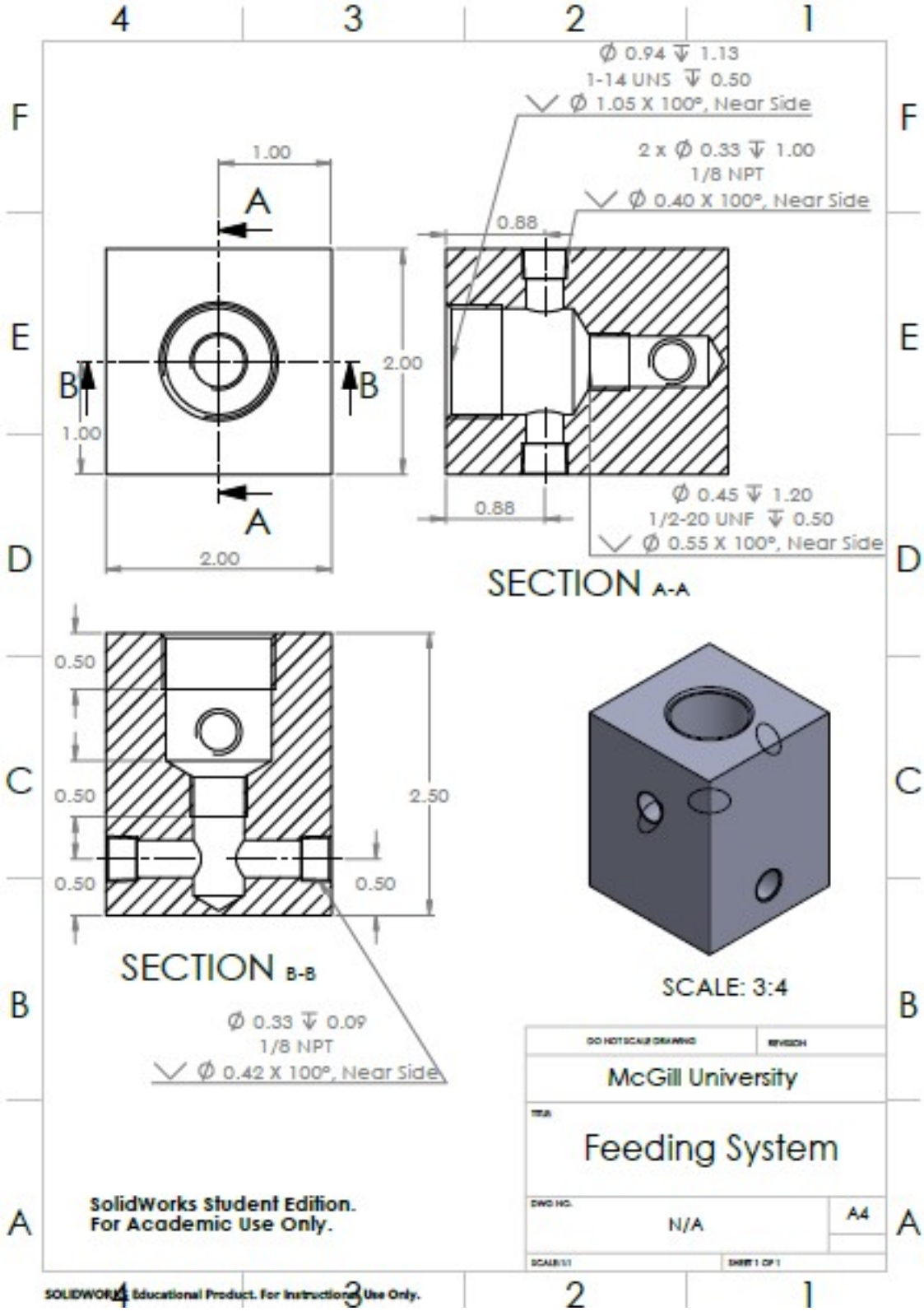

Figure 42: Design drawing of feeding system with tangential inlets.

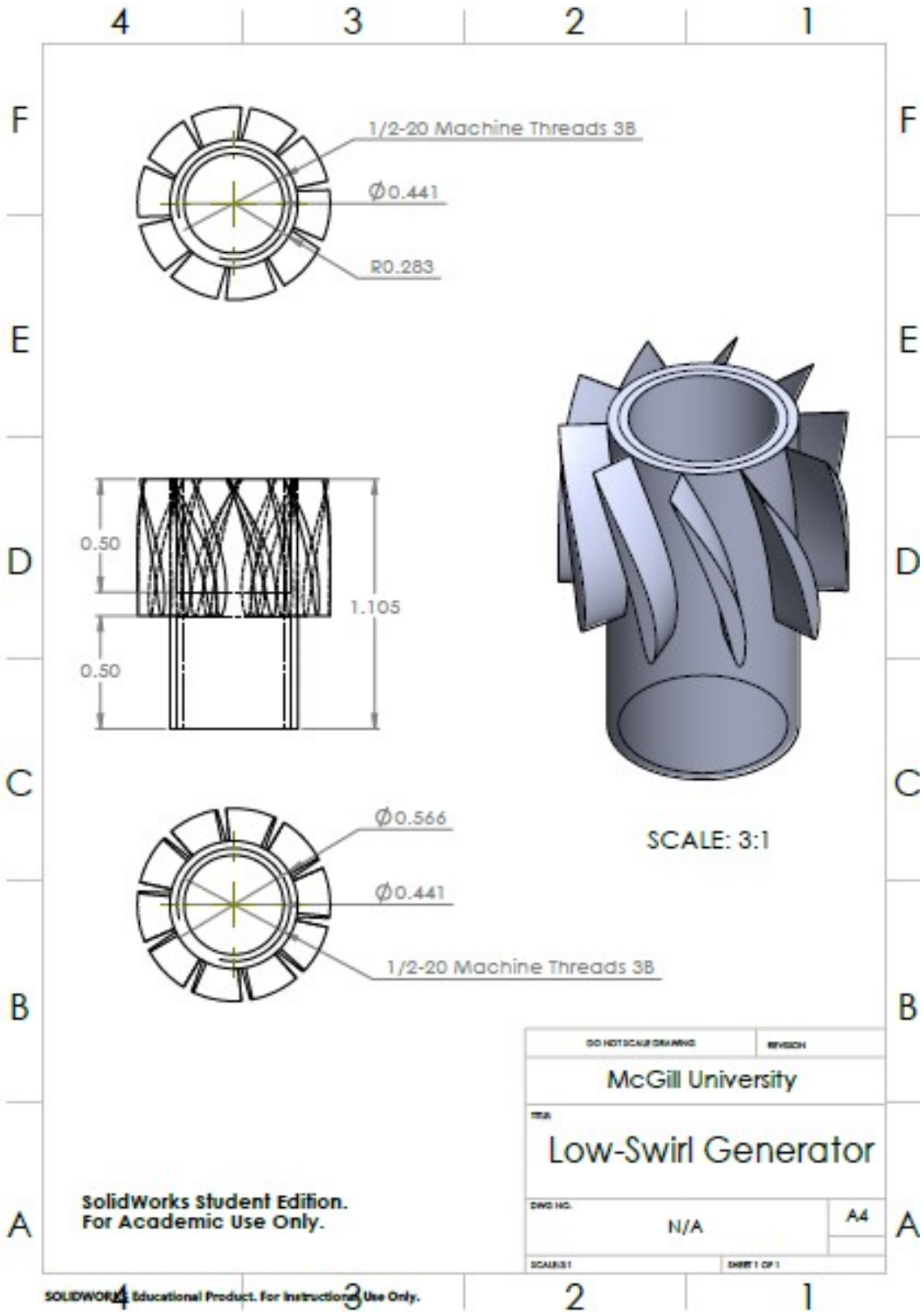

Figure 43: Design drawing of low-swirl injector.

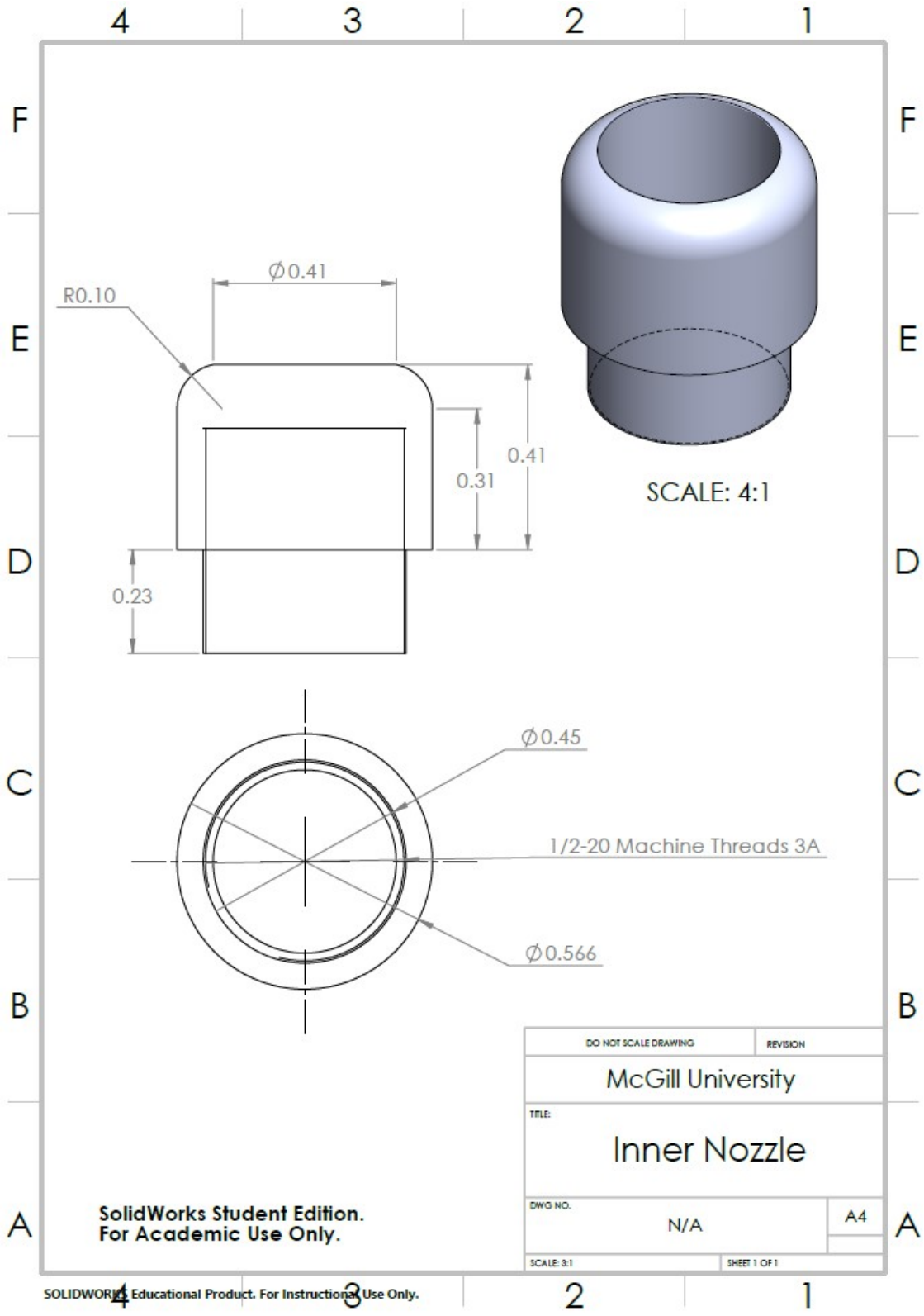

Figure 44: Design drawing of top modular piece to inner plenum. Piece fastens on top of low-swirl injector.

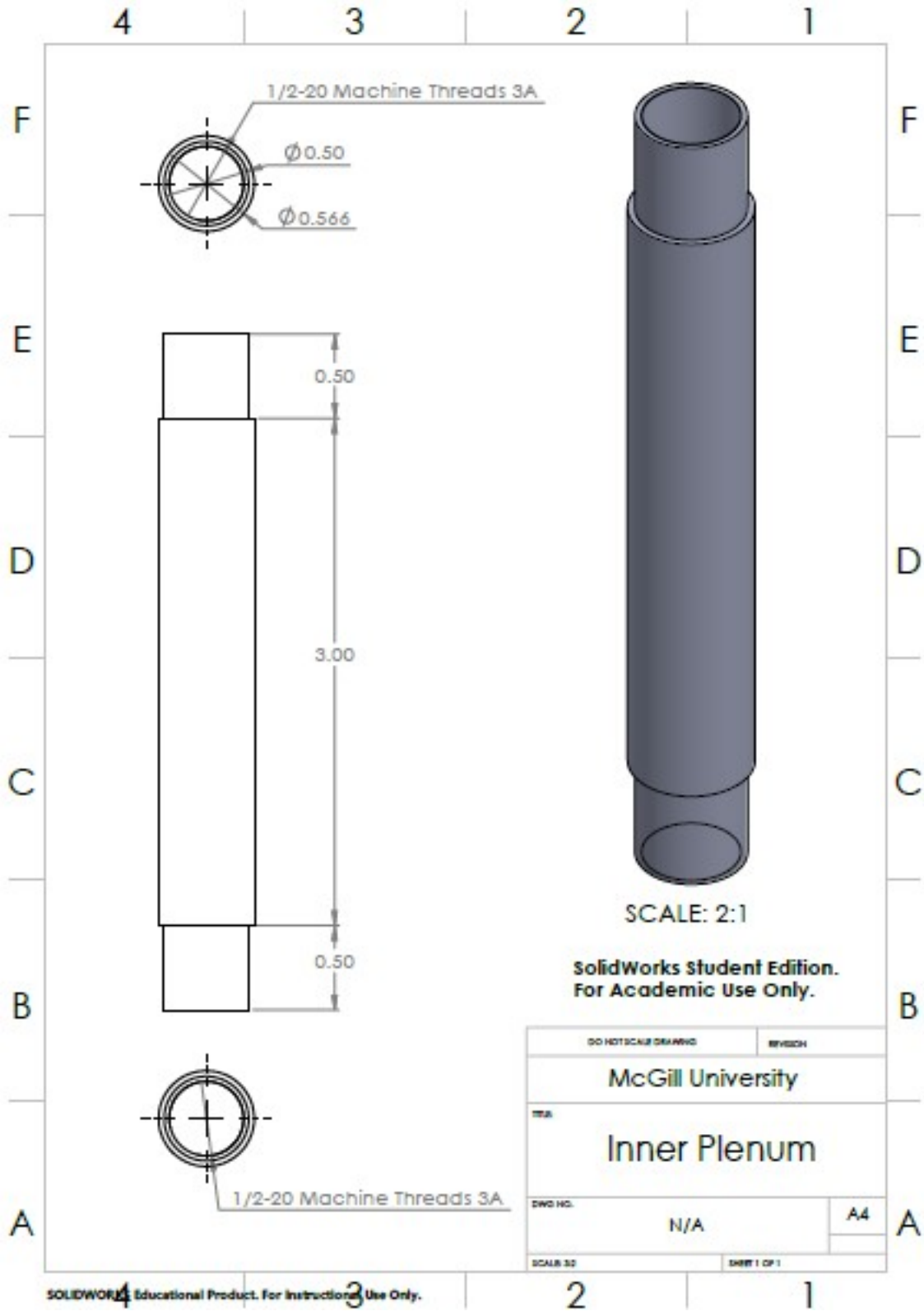

Figure 45: Design drawing of bottom modular piece to inner plenum. Piece fastens under low-swirl injector.

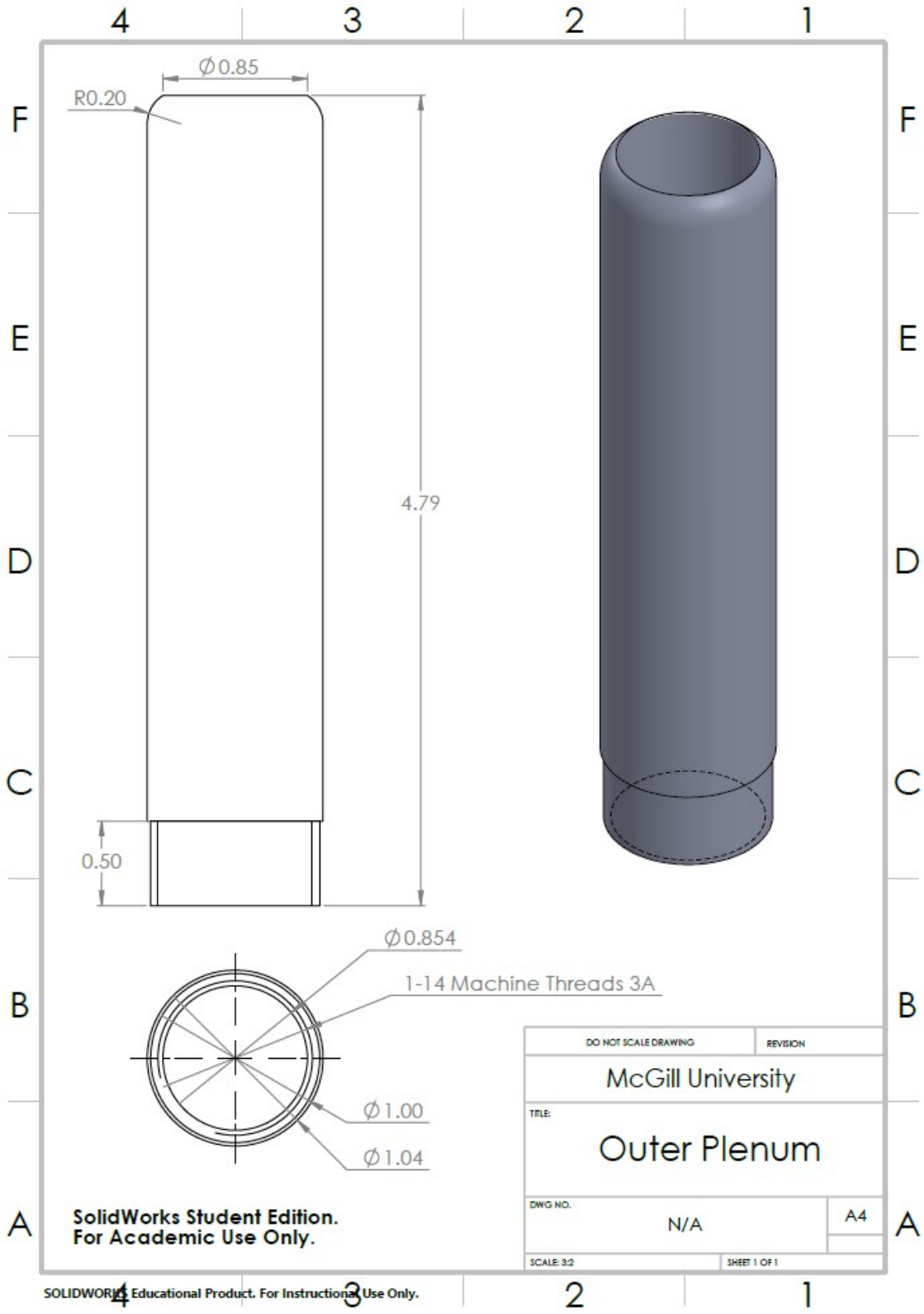

Figure 46: Design drawing of outer plenum.

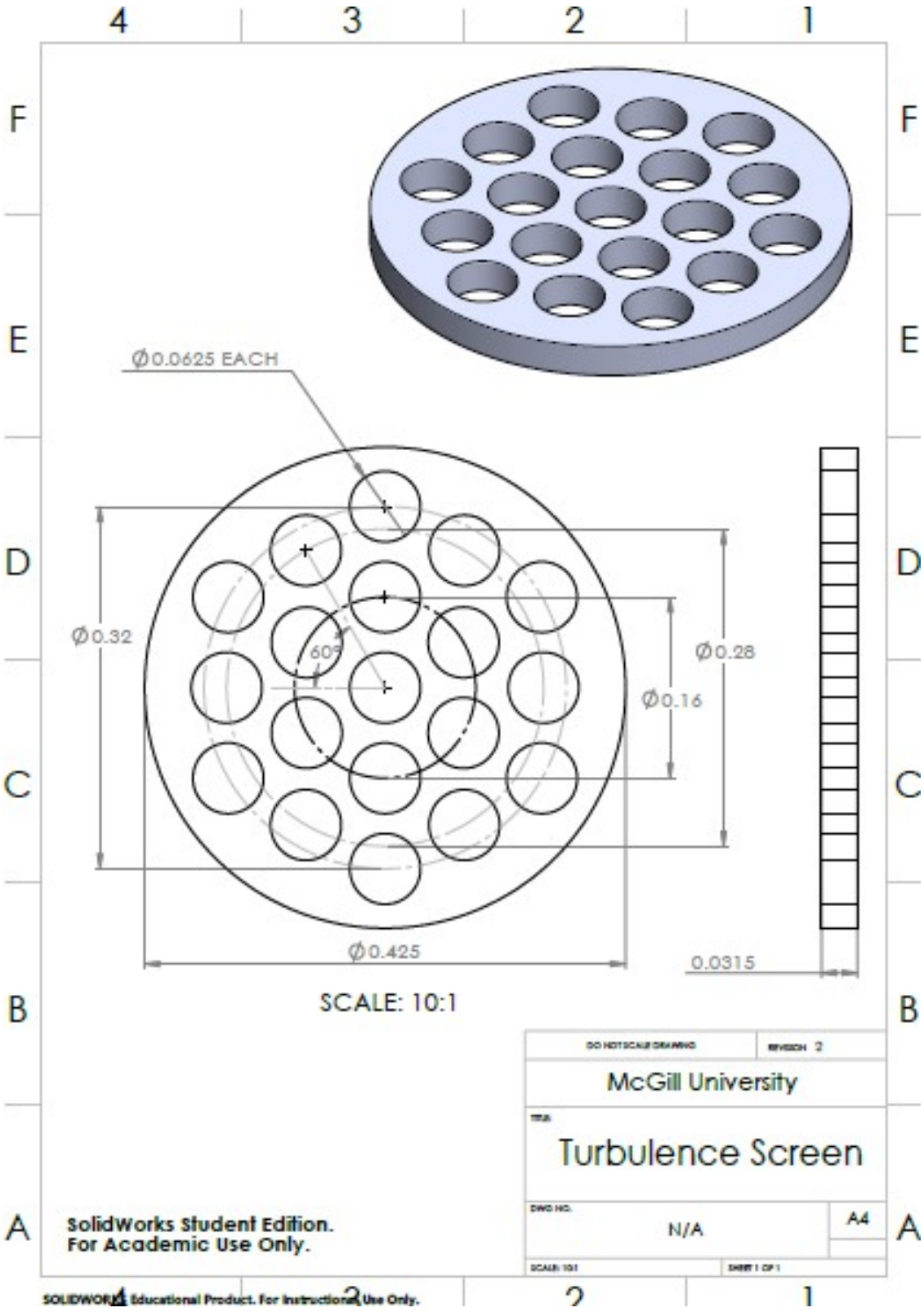

Figure 47: Design drawing of turbulence generating plate.

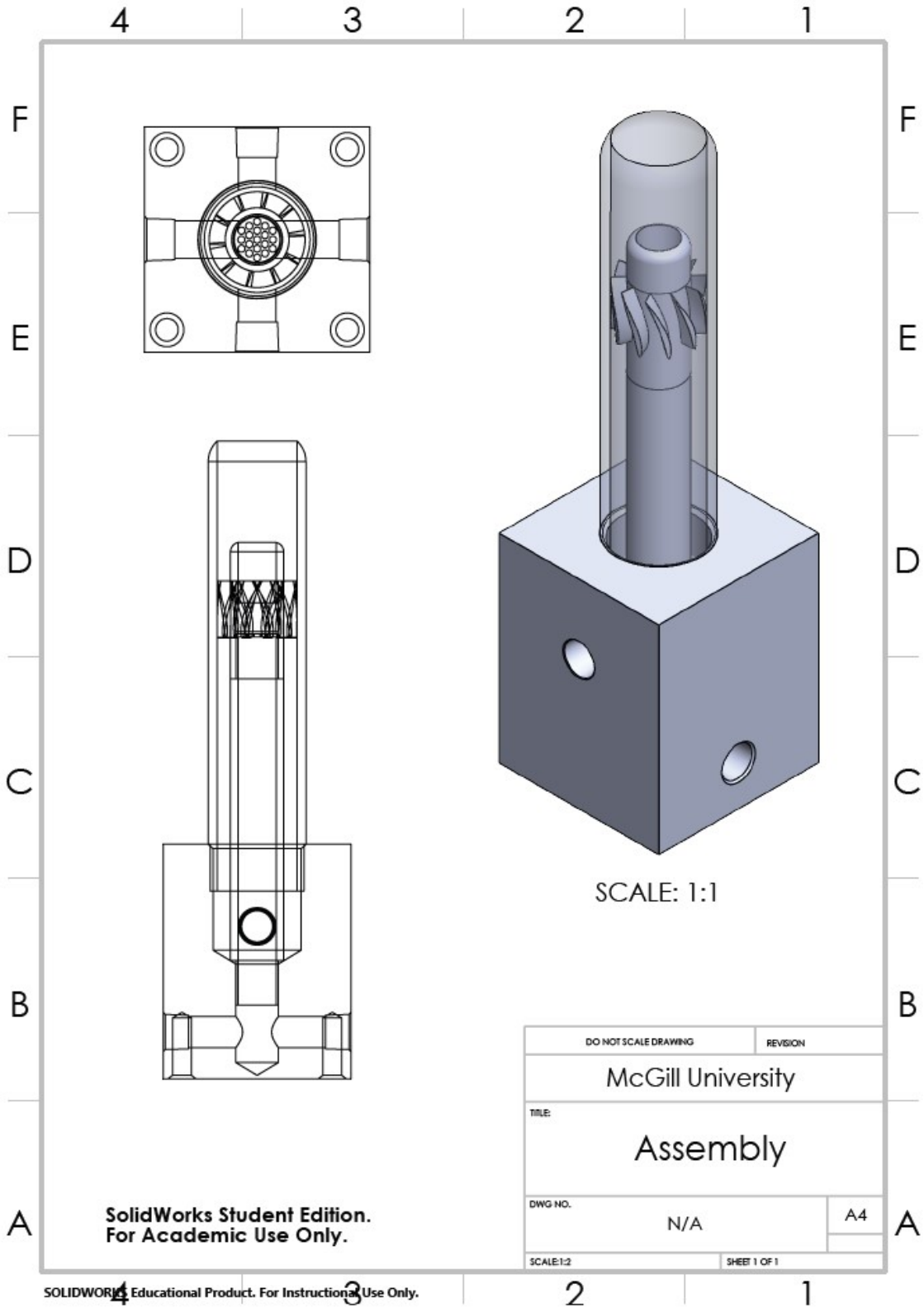

Figure 48: Assembly drawing of fully-controllable low-swirl burner.

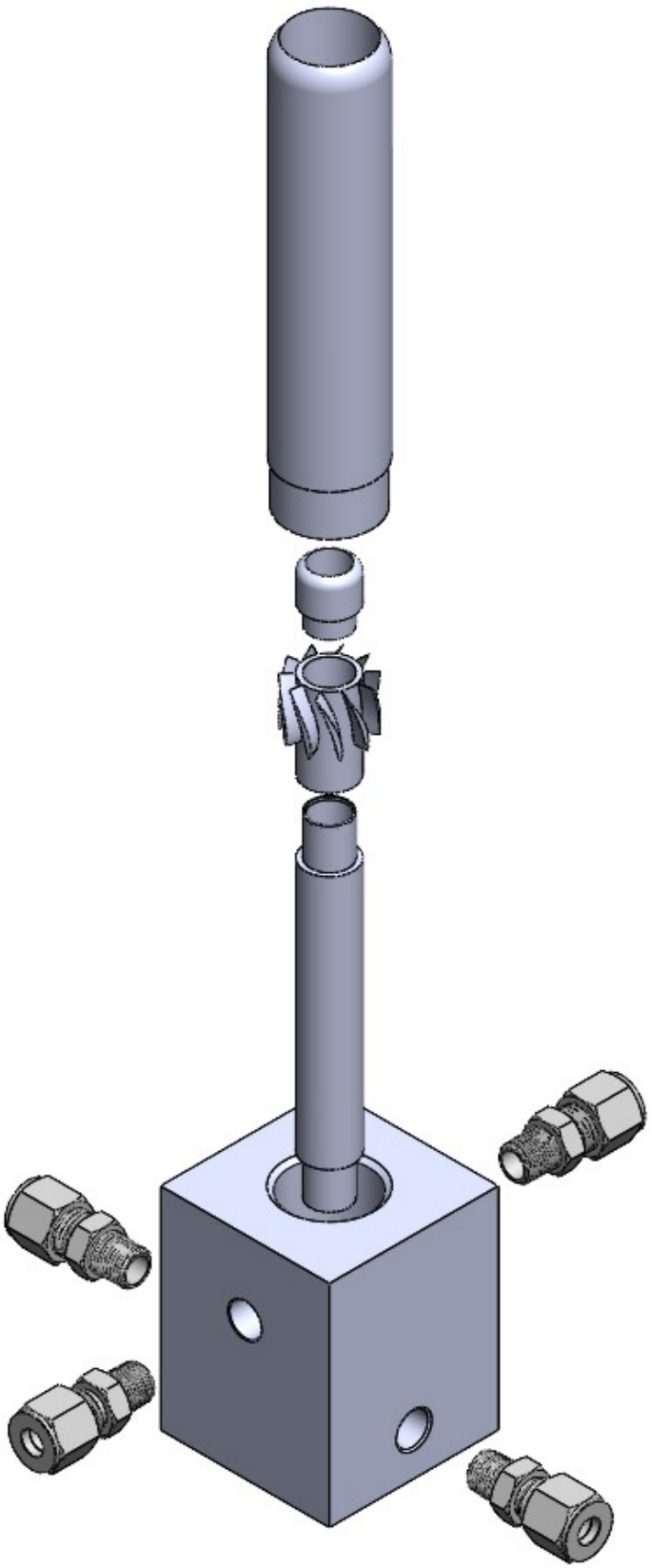

Figure 49: Exploded view of all components of low-swirl burner.

A.3 Uncertainty in PIV and flow measurements

Atomized canola oil droplets are used as the seeding medium for particle image velocimetry because of their ability to simultaneously resolve the velocity field and the instantaneous flamefront location. Ideally, the seeding particle, which is approximately 1-2 μm [93], follows the fluid's streamlines uniformly such that $u_\mathrm{p} = u_\mathrm{f}$, where u_p is the particle velocity and u_f is the fluid velocity. Particle sizes are often chosen for their scattering efficiency, but particles which are too large do not adequately follow flow streamlines due to slip which occurs along the particle boundary. The forces exerted on the particle are considered to estimate the uncertainty between tracked flow velocity and actual velocity. The inertia of the seeding particle, which can be modeled as a perfect sphere, is described according to Newton's Second Law:

$$\Sigma \mathbf{F} = m_\mathrm{p} \mathbf{a}_\mathrm{p} = \rho_\mathrm{p} \frac{\pi d_\mathrm{p}^3}{6} \frac{d\mathbf{u}}{dt} \tag{31}$$

Here, ρ_p describes the canola oil's density multiplied by the volume of a sphere. The acceleration a of the particle by the flame is assumed to be uniform. The forces acting on a particle include:

$$\rho_\mathrm{p} \frac{\pi d_\mathrm{p}^3}{6} \frac{d\mathbf{u}}{dt} = \mathbf{F}_\mathrm{SD} + \mathbf{F}_\mathrm{G} + \mathbf{F}_\mathrm{TP} + \mathbf{F}_\mathrm{other} \tag{32}$$

The summation of forces acting on a particle include Stokes drag $\mathbf{F}_\mathrm{SD}$ attributed to the viscosity between the particle and the fluid, the gravitational force $\mathbf{F}_\mathrm{G}$, the thermophoretic force $\mathbf{F}_\mathrm{TP}$ observed in high-temperature gradients and additional forces $\mathbf{F}_\mathrm{other}$ due to added mass by an accelerating body in a fluid, pressure gradients in vicinity of particle and buoyancy-driven forces. Since particle Reynolds numbers Re_p are $\approx O(1)$, the flow around the particle can be described as potential flow in which case the force due to added mass can be neglected. Furthermore, the density of the gaseous mixture ρ_f is several magnitudes lower than the density of the particle ρ_p. Therefore, forces due to buoyancy, gravity and near-vicinity pressure gradients can be considered negligible with respect to Stokes drag and thermophoretic forces. Lastly, the vaporization point of the oil droplets occurs at temperatures < 576 K which is assumed to be within the low temperature-gradient zone of the flame. In this case, the primary force acting on the particle which would skew its tracking efficiency is the Stokes viscous drag. The Stokes drag is characterized by the following expression with an additional correction factor to account for slip along the particle boundary layer:

$$\rho_\mathrm{p} \frac{\pi d_\mathrm{p}^3}{6} \frac{d\mathbf{u}}{dt} = \rho_\mathrm{p} \frac{\pi d_\mathrm{p}^3}{6} \sigma u_\mathrm{p} = \frac{3\pi \mu d_\mathrm{p} (u_\mathrm{f} - u_\mathrm{p})}{\mathrm{C}_\mathrm{KW}} \tag{33}$$

The Knudsen-Weber slip correction factor C_{KW} is calculated by estimating the Knudsen number from the mean free path of the particle, as detailed by Bergthorson et al. [94]. The uniform velocity gradient σ (1/m) of the particle assumed to be equivalent to the velocity gradient of the fluid, is estimated by normalizing the turbulent RMS fluctuation of the flow by the characteristic integral length scale Λ such that $\sigma \approx u_{RMS}/\Lambda$. Therefore, an expression to determine the relative velocity tracking uncertainty between the particle and the fluid is derived below:

$$\frac{u_p}{u_g} = \frac{1}{1 + C_{KW}\tau_s\sigma} \tag{34}$$

From equation 6, if the Stokes time $\tau_s = \rho_p d_p^2/18\mu$ normalized by the flow time (often associated with the Kolmogorov time scale τ_η), also known as the Stokes number St, is less than 0.05, then the particles adequately capture the flow. In these experiments, the Kolmogorov time scale is on the order of $O(10^{-4})$, in which case St is ≈ 0.03. The uncertainty in particle tracking is captured in Table 3 depicting thermodynamic and transport properties of the gaseous mixture used to compute the slip correction factor. In these experiments, the maximum uncertainty in particle tracking is estimated to be below 1.2%.

Table 3: Thermodynamic and transport properties corresponding to PIV uncertainty calculation according to slip correction factor, C_{KW}.

X_{H_2} (%)	$MW_{mix.}$ (kg/kmol)	$\mu_{mix.}$ (Pa-s)	$R_{mix.}$ (J/kg·K)	C_{KW}	$\tau_s\sigma_u \cdot 10^3$	Uncert. (%)
0	27.83	1.7776E-05	298.7424	1.108	9.84	1.08
20	27.52	1.7782E-05	302.1076	1.108	9.50	1.04
40	27.10	1.7782E-05	306.7897	1.109	9.67	1.06
60	26.56	1.7779E-05	313.0860	1.110	9.75	1.07
80	25.79	1.7773E-05	322.3230	1.112	10.20	1.12

Flowrates for H_2, CH_4 and air are controlled by 4 Brooks Elastomer Sealed Thermal Mass Flow controllers (2 for air, 2 for CH_4 fuel) and 2 Bronkhorst EL-FLOW Select Mass Flow controllers (MFC) (2 for H_2 fuel). A total of six MFCs were used to independently deliver reactant flow through the inner and outer plena of the burner in units of standard liters per minute (SLPM). For both plena, identical conditions in ϕ and mixture composition were delivered where the fuel streams for H_2 and CH_4 were first premixed prior to further premixing with air (oxidizer). In the case of the inner plenum, a micrometer valve was installed to create an air bypass which was delivered to the TSI atomizer. The bypass ratio (i.e. effectively the seeding density) was controlled by installing the micrometer valve downstream such that closing the valve forces more flow through the atomizer instead. The

addition of two 0.5-micron Swagelok filters downstream of fuel-air premixing and four Poppet Swagelok check valves downstream of the fuel MFCs were added as a safety precaution to arrest the flame in case of flashback. The MFCs were calibrated on site using a Bios DryCal ML-800-44 to reduce uncertainty between the flow rate at the setpoint (SP) and the actual flow rate. MFC properties are listed in Table 4 and whose setup corresponds to the diagram in Figure 50:

Table 4: Mass flow controllers used during experimentation. Uncertainties on MFCs reported within 20-100% full scale (FS).

MFC	Manufacturer Uncertainty (%)
Brooks SLA5800 (10 SLPM)	± 0.9% SP
Brooks SLA5800 (30 SLPM)	± 0.9% SP
Brooks SLA5800 (100 SLPM)	± 0.9% SP
Brooks SLA5800 (300 SLPM)	± 0.9% SP
Bronkhorst EL-FLOW (20 SLPM)	± 0.5% SP ± 0.1% FS
Bronkhorst EL-FLOW (50 SLPM)	± 0.5% SP ± 0.1% FS

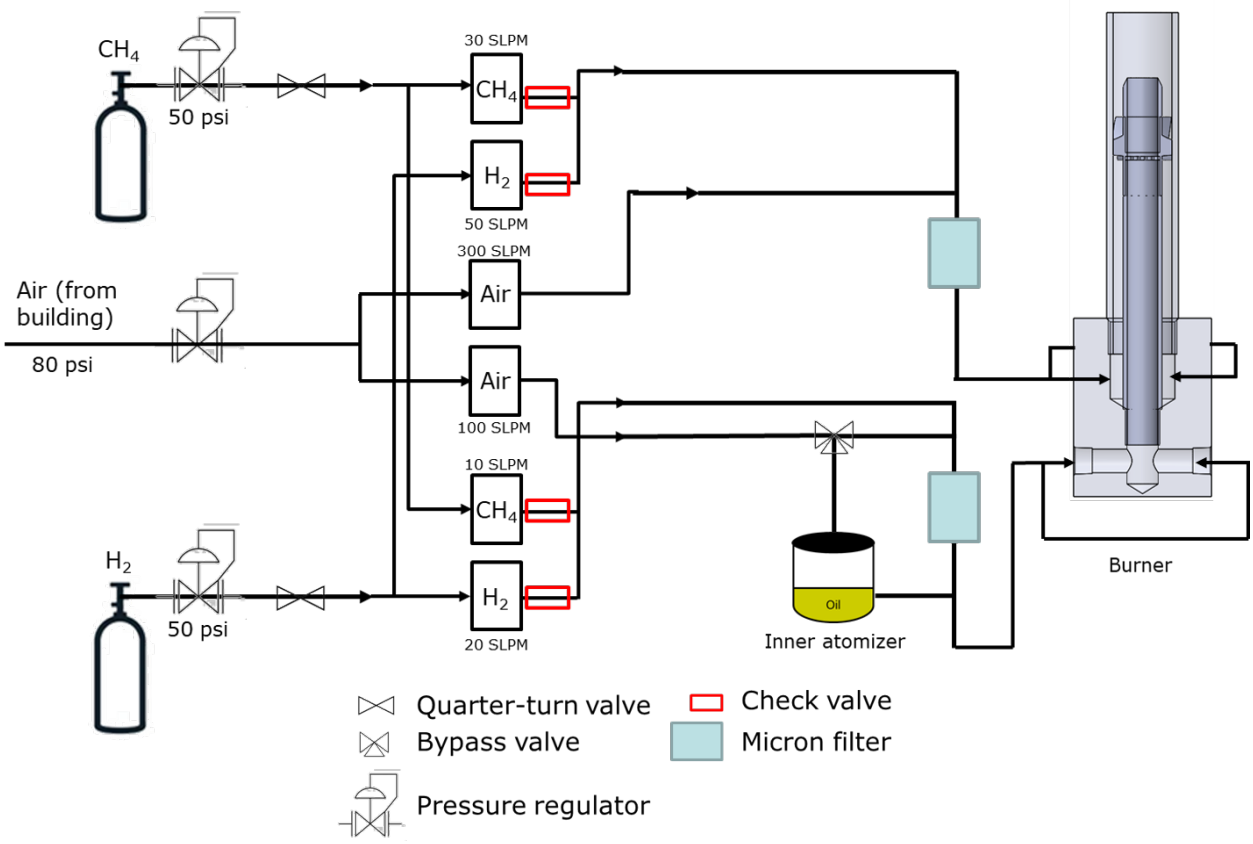

Figure 50: Schematic of swirl burner setup with six (6) mass flow controllers.

Considering the bulk velocity is kept constant in this study, an estimation of the mass flow through the center channel (-0.25$D_{\text{nozzle}} \leq r \leq 0.25D_{\text{nozzle}}$) at the nozzle exit is calculated by computing the bulk flow rate of the mixture. The bulk flow rate is estimated by radially integrating the mean axial velocity profile obtained from high-speed PIV and assumes the flowfield is axisymmetrical.

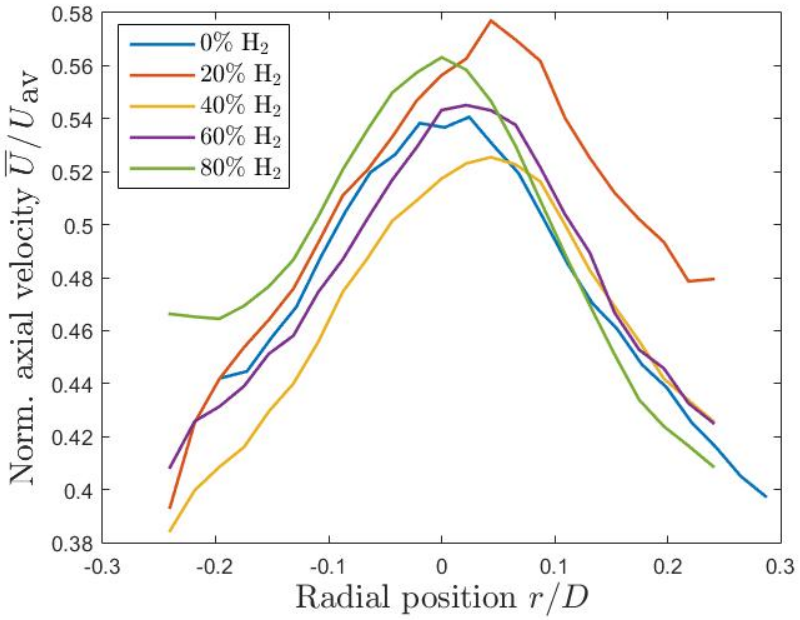

Figure 51: Radial profiles of normalized mean axial velocity collected at nozzle exit (McGill experimental campaign).

In order to compute the constant bulk velocity at the nozzle exit, the interrogation window in DaVis is changed from 32×32 to 64×64 to sufficiently capture the faster particle motion. The measured bulk velocities in the center core are listed in Table 5. The average inner velocity from all mixtures is 12.11 m/s with a standard deviation of 0.38 m/s with an error of 19.7% to the theoretical value of $u = 10.12$ m/s through the center channel (i.e. center core velocity required for a bulk velocity $U_{\text{av}} = 13$ m/s).

Table 5: Average flow velocity calculated in domain corresponding to center channel at nozzle exit. Density of each mixture computed in Cantera using GRI30 thermochemical mechanism and corresponds to density of unburned reactants.

X_{H_2}	$\rho_{\text{mix.}}$	$u_{\text{meas.}}$ (m/s)
0	1.14	11.96
20	1.13	12.69
40	1.11	11.68
60	1.09	11.99
80	1.06	12.23

A.4 Uncertainty in flamefront tracking

The degree with which the MATLAB tracking algorithm predicts the flamefront location is subject to inherent uncertainties in post-processing, as detailed by Abbasi et al. [54]. Several sources of uncertainty between the predicted flamefront and the actual flamefront include the mean tracer particle distance l_{p}, the evaporation distance l_{evap} as a result of the oil droplet lifetime and uncertainties in distance due to median filtering l_{Filt} and size of the oil droplets captured by the CMOS camera l_{I}. The mean tracer particle distance, which coincides with the seeding density, is calculated from the binarized Mie scattered image relative to its equivalent saturated image such that l_{p} characterizes the average distance between particles. This average measurement is performed for 2000 PIV images for all conditions evaluated. The oil evaporation distance l_{evap} is calculated from the multiplication of its lifetime τ_{evap} and the maximum flamelet velocity $S_{\text{F,max}}$ measured in post-processing. The oil lifetime is expressed as $\tau_{\text{evap}} = d_{\text{p}}^2/E$, where d_{p} is estimated to be at most $\approx 2\mu$m and E is the evaporation constant, as described in [95]:

$$E = \frac{8\lambda}{\rho c_p} \ln\left(1 + \frac{c_p(T_\infty - T_s)}{h_v}\right) \tag{35}$$

Here, λ is the thermal conductivity of the mixture, ρ and c_{p} are the density and specific heat capacity of the canola oil, T_∞ is estimated as the average temperature between the adiabatic temperature and the ambient room temperature: $T_\infty = (T_{\text{ad}} - T_{\text{amb.}})/2$, T_{s} is the flash point of the oil at ≈ 576 K and h_v is the latent heat of vaporization of the oil. The distance uncertainty due to non-linear median filtering of the Mie scattered image with a 5x5 window is estimated as $l_{\text{Filt}} \approx 2.5$ pixels. Lastly, the distance related to the pixel width of the imaged particle on the CMOS array is estimated as $l_{\text{I}} \approx 2$ pixels. The uncertainties on l_{Filt} and l_{I} are converted to physical units through the spatial resolution coefficient, C. All uncertainty contributions to flamefront tracking are outlined in Table 6.

Table 6: Uncertainties in flamefront tracking dependent on mean particle distance l_p, evaporation distance $l_{\mathrm{evap}.}$ and distances due to filtering $l_{\mathrm{Filt}.}$ and imaging l_I of seed particles.

$X_{\mathrm{H_2}}$	l_I/δ_L	$l_{\mathrm{Filt}.}/\delta_L$	l_p/δ_L	$l_{\mathrm{evap}.}/\delta_L$	$l_{\mathrm{Tot}.}/\delta_L$
0	0.189	0.236	0.589	0.041	0.663
20	0.190	0.237	0.472	0.042	0.563
40	0.191	0.238	0.442	0.043	0.539
60	0.192	0.240	0.387	0.046	0.496
80	0.193	0.241	0.335	0.049	0.458

Therefore, the total uncertainty due to flamefront tracking, which is calculated by the root of the sum of squares from all uncertainty components (i.e. $l_{\mathrm{Tot}.} = \sqrt{l_\mathrm{I}^2 + l_{\mathrm{Filt}.}^2 + l_\mathrm{p}^2 + l_{\mathrm{evap}.}^2}$) is estimated to be within 0.7 times the diffusive laminar flame thickness of the hydrogen-enriched mixture ($\leq 0.7\delta_\mathrm{L}$).

B References

[1] H. Ritchie, M. Roser, P. Rosado, Energy, https://ourworldindata.org/energy (2022).

[2] V. S. Ediger, An integrated review and analysis of multi-energy transition from fossil fuels to renewables, Energy Procedia 156 (2019) 2–6.

[3] Z. Liu, Z. Deng, S. J. Davis, C. Giron, P. Ciais, Monitoring global carbon emissions in 2021, Nature Reviews Earth & Environment 3 (2022) 217–219.

[4] P. Julien, J. M. Bergthorson, Enabling the metal fuel economy: green recycling of metal fuels, Sustainable Energy & Fuels 1 (2017) 615–625.

[5] J. M. Bergthorson, Y. Yavor, J. Palecka, W. Georges, M. Soo, J. Vickery, S. Goroshin, D. L. Frost, A. J. Higgins, Metal-water combustion for clean propulsion and power generation, Applied Energy 186 (2017) 13–27.

[6] J. M. Bergthorson, Recyclable metal fuels for clean and compact zero-carbon power, Progress in Energy and Combustion Science 68 (2018) 169–196.

[7] W. He, M. King, X. Luo, M. Dooner, D. Li, J. Wang, Technologies and economics of electric energy storages in power systems: Review and perspective, Advances in Applied Energy 4 (2021) 100060.

[8] V. S. Arutyunov, G. V. Lisichkin, Energy resources of the 21st century: problems and forecasts. Can renewable energy sources replace fossil fuels?, Russian Chemical Reviews 86 (2017) 777.

[9] G. R. Timilsina, Are renewable energy technologies cost competitive for electricity generation?, Renewable Energy 180 (2021) 658–672.

[10] L. Delannoy, P.-Y. Longaretti, D. J. Murphy, E. Prados, Peak oil and the low-carbon energy transition: A net-energy perspective, Applied Energy 304 (2021) 117843.

[11] D. Noble, D. Wu, B. Emerson, S. Sheppard, T. Lieuwen, L. Angello, Assessment of current capabilities and near-term availability of hydrogen-fired gas turbines considering a low-carbon future, Journal of Engineering for Gas Turbines and Power 143 (2020) V006T09A007.

[12] T. Bexten, M. Wirsum, B. Roscher, R. Schelenz, G. Jacobs, Model-based analysis of a combined heat and power system featuring a hydrogen-fired gas turbine with on-sitehydrogen production and storage, Journal of Engineering for Gas Turbines and Power 143 (2021) 081018.

[13] T. Bexten, S. Jörg, N. Petersen, M. Wirsum, P. Liu, Z. Li, Model-based thermodynamic analysis of a hydrogen-fired gas turbine with external exhaust gas recirculation, Journal of Engineering for Gas Turbines and Power 143 (2020) V005T06A023.

[14] P. P. Edwards, V. L. Kuznetsov, W. I. David, N. Brandon, Hydrogen and fuel cells: Towards a sustainable energy future, Energy Policy 36 (2008) 4356–4362.

[15] H. Zhao, J. Wang, X. Cai, H. Dai, Z. Bian, Z. Huang, Flame structure, turbulent burning velocity and its unified scaling for lean syngas/air turbulent expanding flames, International Journal of Hydrogen Energy 46 (2021) 25699–25711.

[16] P. Venkateswaran, A. Marshall, D. H. Shin, D. Noble, J. Seitzman, T. Lieuwen, Measurements and analysis of turbulent consumption speeds of h_2-co mixtures, Combustion and Flame 158 (2011) 1602–1614.

[17] M. Hermesmann, T. E. Müller, Green, turquoise, blue, or grey? environmentally friendly hydrogen production in transforming energy systems, Progress in Energy and Combustion Science 90 (2022) 100996.

[18] H. M. Barthélémy, M. Weber, F. Barbier, Hydrogen storage: Recent improvements and industrial perspectives, International Journal of Hydrogen Energy 42 (2017) 7254–7262.

[19] K. A. Trowell, S. Goroshin, D. L. Frost, J. M. Bergthorson, The use of supercritical water for the catalyst-free oxidation of coarse aluminum for hydrogen production, Sustainable Energy Fuels 4 (2020) 5628–5635.

[20] A. Clerici, S. Furfari, Challenges for green hydrogen development, 2021 AEIT International Annual Conference (AEIT) (2021) 1–6.

[21] C. B. Agaton, K. I. T. Batac, E. M. R. Jr., Prospects and challenges for green hydrogen production and utilization in the philippines, International Journal on Hydrogen Energy 47 (2022) 17859–17870.

[22] F. Hampp, K. H. Goh, R. Lindstedt, The reactivity of hydrogen enriched turbulent flames, Process Safety and Environmental Protection 143 (2020) 66–75.

[23] X. Duan, Y. Li, Y. Liu, S. Zhang, J. Guan, M.-C. Lai, J. Liu, Dilution gas and hydrogen enrichment on the laminar flame speed and flame structure of the methane/air mixture, Fuel 281 (2020) 118794.

[24] M. Brower, E. L. Petersen, W. Metcalfe, M. F. Henry J. Curran, G. Bourque, N. Aluri, F. Güthe, Ignition delay time and laminar flame speed calculations for natural gas/hydrogen blends at elevated pressures, Journal of Engineering for Gas Turbines and Power 135 (2013) 021504.

[25] J. D. Willis, I. J. Toona, T. Schweiger, D. A. Owen, Industrial RB211 dry low emission combustion, Turbo Expo: Power for Land, Sea, and Air 78927 (1993) V03CT17A052.

[26] G. Leonard, J. Stegmaier, Development of an aeroderivative gas turbine dry low emissions combustion system, Turbo Expo: Power for Land, Sea, and Air 116 (1994) 542–546.

[27] L. A. Bulysova, V. D. Vasil'ev, A. L. Berne, Low-emission combustion of fuel in aeroderivative gas turbines, Thermal Engineering 64 (2017) 891–897.

[28] N. K. Rizk, H. C. Mongia, Ultra-low NO_x rich-lean combustion, Turbo Expo: Power for Land, Sea, and Air 79061 (1990) V003T06A022.

[29] C. K. Law, Combustion Physics, Cambridge University Press, New York, 2006.

[30] A. Durocher, P. Versailles, G. Bourque, J. Bergthorson, Impact of kinetic uncertainties on accurate prediction of no concentrations in premixed alkane-air flames, Combustion Science and Technology 192 (6) (2020) 959–985.

[31] O. Tuncer, The effect of hydrogen enrichment of methane fuels on flame stability and emissions, International Conference on Renewable Energy Research and Applications (ICRERA) (2013) 103–108.

[32] F. Coppens, J. D. Ruyck, A. Konnov, Effects of hydrogen enrichment on adiabatic burning velocity and NO formation in methane + air flames, Experimental Thermal and Fluid Science 31 (2007) 437–444.

[33] T. Lieuwen, V. McDonell, E. Petersen, D. Santavicca, Fuel flexibility influences on premixed combustor blowout, flashback, autoignition, and stability, Journal of Engineering for Gas Turbines and Power 130 (2008) 011506.

[34] C.-H. Sohn, Unsteady analysis of acoustic pressure response in N_2 diluted H_2 and air diffusion flame, Combustion and Flame 128 (1) (2002) 111–120.

[35] G. A. Richards, M. M. McMillian, R. S. Gemmen, W. A. Rogers, S. R. Cully, Issues for low-emission, fuel-flexible power systems, Progress in Energy and Combustion Science 27 (2001) 141–169.

[36] G. Troiani, F. Creta, M. Matalon, Experimental investigation of darrieus–landau instability effects on turbulent premixed flames, Proceedings of the Combustion Institute 35 (2015) 1451–1459.

[37] W.-W. Kim, S. Menon, Numerical modeling of turbulent premixed flames in the thin-reaction-zones regime, Combustion Science and Technology 160 (2000) 119–150.

[38] V. Chakravarthy, S. Menon, Large-eddy simulation of turbulent premixed flames in the flamelet regime, Combustion Science and Technology 162 (2001) 175–222.

[39] T. Dunstan, Y. Minamoto, N. Chakraborty, N. Swaminathan, Scalar dissipation rate modelling for large-eddy simulation of turbulent premixed flames, Proceedings of the Combustion Institute 34 (2013) 1193–1201.

[40] W. M. Deen, Analysis of Transport Phenomena, Oxford University Press, New York, 2012.

[41] H. Tennekes, J. L. Lumley, A First Course in Turbulence, The MIT Press, England, 1972.

[42] N. Peters, Turbulent combustion, Cambridge University Press, New York, 2000.

[43] A. W. Skiba, T. M. Wabel, C. D. Carter, S. D. Hammack, J. E. Temme, J. F. Driscoll, Premixed flames subjected to extreme levels of turbulence part i: Flame structure and a new measured regime diagram, Combustion and Flame 189 (2017) 407–432.

[44] I. G. Shepherd, R. K. Cheng, The burning rate of premixed flames in moderate and intense turbulence, Combustion and Flame 127 (2001) 2066–2075.

[45] B. E. Rapp, Microfluidics: Modelling, Mechanics and Mathematics, 2017.

[46] V. Karpov, A. Lipatnikov, V. Zimont, Flame curvature as a determinant of preferential diffusion effects in premixed turbulent combustion, Advances in Combustion Science (Progress in Astronautics and Aeronautics) 173 (1997) 235–250.

[47] P. Venkateswaran, A. Marshall, J. Seitzman, T. Lieuwen, Scaling turbulent flame speeds of negative markstein length fuel blends using leading points concepts, Combustion and Flame 162 (2015) 375–387.

[48] G. Damköhler, The influence of turbulence on the flame speed in gas mixtures (der einfluss der turbulenz auf die flammengeschwindigkeit in gasgemischen), Zeitschrift fur Elektrochemie und angewante physikalische Chemie 46 (1940) 601–626.

[49] P. Venkateswaran, A. Marshall, D. H. Shin, D. Noble, J. Seitzman, T. Lieuwen, Measurements and analysis of turbulent consumption speeds of H_2/CO mixtures, Combustion and Flame 158 (2011) 1602–1614.

[50] J. B. Bell, R. K. Cheng, M. S. Day, I. G. Shepherd, Numerical simulation of lewis number effects on lean premixed turbulent flames, Proceedings of the Combustion Institute 31 (2007) 1309–1317.

[51] S. A. Filatyev, J. F. Driscoll, C. D. Carter, J. M. Donbar, Measured properties of turbulent premixed flames for model assessment, including burning velocities, stretch rates, and surface densities, Combustion and Flame (2005) 1–21.

[52] D. Bradley, How fast can we burn?, Symposium (International) on Combustion 24 (1992) 247–262.

[53] M. An, S. Pope, Calculations of premixed turbulent flames by pdf methods, Combustion and Flame 67 (2) (1987) 127–142.

[54] E. Abbasi-Atibeh, The effects of differential diffusion in counter-flow premixed flames with dilution and hydrogen enrichment, Ph.D. thesis, McGill University (2019).

[55] R. K. Cheng, Low-swirl combustion, The Gas Turbine Handbook (2006) 241–255.

[56] D. M. Markovich, S. S. Abdurakipov, L. M. Chikishev, V. M. Dulin, K. Hanjalić, Comparative analysis of low- and high-swirl confined flames and jets by proper orthogonal and dynamic mode decompositions, Physics of Fluids 26 (2014) 065109.

[57] M. R. Johnson, D. Littlejohn, W. A. Nazeer, K. O. Smith, R. K. Cheng, A comparison of the flowfields and emissions of high-swirl injectors and low-swirl injectors for lean premixed gas turbines, Proceedings of the Combustion Institute 30 (2005) 2867–2874.

[58] R. K. Cheng, S. A. Fable, D. Schmidt, L. Arellano, K. O. Smith, Development of a low swirl injector concept for gas turbines, United States Department of Energy (2000) 785290.

[59] Q. An, S. Kheirkhah, J. Bergthorson, S. Yun, J. Hwang, W. J. Lee, M. K. Kim, J. H. Cho, H. S. Kim, P. Vena, Flame stabilization mechanisms and shape transitions in a

3D printed, hydrogen enriched, methane/air low-swirl burner, International Journal of Hydrogen Energy 46 (2021) 14764–14779.

[60] P. L. Therkelsen, D. Littlejohn, R. K. Cheng, Parametric study of low-swirl injector geometry on its operability, Turbo Expo: Power for Land, Sea and Air 2 (2013) 309–318.

[61] A. Marshall, P. Venkateswaran, D. Noble, J. Seitzman, T. Lieuwen, Development and characterization of a variable turbulence generation system, Experiments in Fluids 51 (2011) 611–620.

[62] G. Coppola, A. Gomez, Experimental investigation on a turbulence generation system with high-blockage plates, Experimental Thermal and Fluid Science 33 (2009) 1037–1048.

[63] N. Syreed, J. M. Béer, Combustion in swirling flows: A review, Combustion and Flame 23 (2) (1974) 143–201.

[64] G. E. Ballachey, M. R. Johnson, Prediction of blowoff in a fully controllable low-swirl burner burning alternative fuels: Effects of burner geometry, swirl, and fuel composition, Proceedings of the Combustion Institute 34 (2013) 3193–3201.

[65] M. Feyz, J. Esfahani, I. Pishbin, S. M. Razavi, Effect of recess length on the flame parameters and combustion performance of a low swirl burner, Applied Thermal Engineering 89 (2015) 609–617.

[66] N. Bouvet, F. Halter, C. Chauveau, Y. Yoon, On the effective lewis number formulations for lean hydrogen/hydrocarbon/air mixtures, International Journal on Hydrogen Energy 38 (2013) 5949–5960.

[67] University of California at San Diego, Chemical-kinetic mechanisms for combustion applications, `http://combustion.ucsd.edu`, san Diego Mechanism web page, Mechanical and Aerospace Engineering (Combustion Research) (2016).

[68] X. Chen, Y. Wang, T. Zirwes, F. Zhang, H. Bockhorn, Z. Chen, Heat release rate markers for highly stretched premixed CH_4/air and CH_4/H_2/air flames, Energy and Fuels 35 (16) (2021) 13349–13359.

[69] M. Dunn, A. Masri, A comprehensive model for the quantification of linear and nonlinear regime laser-induced fluorescence of OH under $A_2\Sigma+\leftarrow X_2\Pi(1,0)$ excitation, Applied Physics 101 (2010) 445–463.

[70] N. T. Clemens, Flow imaging, Encyclopedia of imaging science and technology, 2002.

[71] A. Prasad, Stereoscopic particle image velocimetry, Experiments in Fluids 29 (2000) 103–116.

[72] M. Raffel, C. E. Willert, F. Scarano, C. J. Kähler, S. T. Wereley, J. Kompenhans, Particle Image Velocimetry: A Practical Guide, 3rd Edition, Springer International Publishing, Switzerland, 2018.

[73] T. Pavlidis, Algorithms for graphics and image processing, Springer Science & Business Media, 2012.

[74] K. L. Kreider, Applied Numerical Methods II, 2019, https://www.math.uakron.edu/ kreider/num2/CD4.pdf.

[75] R. Cheng, D. Littlejohn, Laboratory study of premixed H_2-air and H_2–N_2-air flames in a low-swirl injector for ultra-low emissions gas turbines, Journal of Engineering for Gas Turbines and Power 130 (2008) 031503.

[76] R. Cheng, D. Littlejohn, W. Nazeer, K. Smith, Laboratory studies of the flow field characteristics of low-swirl injectors for adaptation to fuel-flexible turbines, Journal of Engineering for Gas Turbines and Power 130 (2008) 021501.

[77] R. K. Cheng, D. Littlejohn, P. Strakey, T. Sidwell, Laboratory investigations of a low-swirl injector with H_2 and CH_4 at gas turbine conditions, Proceedings of the Combustion Institute 32 (2009) 3001–3009.

[78] S. D. Salusbury, E. Abbasi-Atibeh, J. M. Bergthorson, The effect of lewis number on instantaneous flamelet speed and position statistics in counter-flow flames with increasing turbulence, Proceedings of ASME Turbo Expo (2017) V003T03A009.

[79] E. Abbasi-Atibeh, J. M. Bergthorson, Differential diffusion effects in counter-flow premixed hydrogen-enriched methane and propane flames, Proceedings of the Combustion Institute 37 (2019) 2399–2406.

[80] I. G. Shepherd, Flame surface density and burning rate in premixed turbulent flames, Symposium (International) on Combustion 26 (1996) 373–379.

[81] J. Hult, S. Gashi, N. Chakraborty, M. Klein, K. W. Jenkins, S. Cant, C. F. Kaminski, Measurement of flame surface density for turbulent premixed flames using PLIF and DNS, Proceedings of the Combustion Institute 31 (2007) 1319–1326.

[82] P. Vena, B. Deschamps, G. Smallwood, M. Johnson, Equivalence ratio gradient effects on flame front topology in a stratified iso-octane/air turbulent v-flame, Proceedings of the Combustion Institute 33 (2011) 1551–1558.

[83] A. Trouvé, T. Poinsot, The evolution equation for the flame surface density in turbulent premixed combustion, Journal of Fluid Mechanics 278 (1994) 1–31.

[84] N. Chakraborty, R. Cant, Effects of lewis number on flame surface density transport in turbulent premixed combustion, Combustion and Flame 158 (2011) 1768–1787.

[85] E. Abbasi-Atibeh, J. M. Bergthorson, The effects of differential diffusion in counter-flow premixed flames with dilution and hydrogen enrichment, Combustion and Flame 209 (2019) 337–352.

[86] M. Emadi, D. Karkow, T. Salameh, A. Gohil, A. Ratner, Flame structure changes resulting from hydrogen-enrichment and pressurization for low-swirl premixed methane-air flames, International Journal on Hydrogen Energy 37 (2012) 10397–10404.

[87] M. Wu, S. Kwon, J. Driscoll, G. Faeth, Turbulent premixed hydrogen/air flames at high Reynolds numbers, Combustion Science and Technology 73 (1990) 327–350.

[88] L. Berger, A. Attili, H. Pitsch, Synergistic interactions of thermodiffusive instabilities and turbulence in lean hydrogen flames, Combustion and Flame 244 (2022) 112254.

[89] A. Marshall, J. Lundrigan, P. Venkateswaran, J. Seitzman, T. Lieuwen, Fuel effects on leading point curvature statistics of high hydrogen content fuels, Proceedings of the Combustion Institute 35 (2015) 1417–1424.

[90] J. F. Driscoll, Turbulent premixed combustion: Flamelet structure and its effect on turbulent burning velocities, Progress in Energy and Combustion Science 34 (2008) 91–134.

[91] P. Trunk, I. Boxx, C. Heeger, W. Meier, B. Bohm, A. Dreizler, Premixed flame propagation in turbulent flow by means of stereoscopic PIV and dual-plane OH-PLIF at sustained khz repetition rates, Proceedings of the Combustion Institute 34 (2013) 3565–3572.

[92] L. Fan, B. Savard, S. Carlyle, M. Nozari, R. Naaman, B. Fond, P. Vena, Simultaneous stereo-PIV and OH×CH_2O PLIF measurements in turbulent ultra lean CH_4/H_2 swirling wall-impinging flames, Proceedings of the Combustion Institute (2022) 1–10.

[93] TSI, TSI Particle Technology: Particle instruments, https://tsi.com/getmedia/b35e42d2-5045-47b1-9522-c0b094d85dbb/Particle_Catalog_Web?ext=.pdf.

[94] J. M. Bergthorson, P. E. Dimotakis, Particle velocimetry in high-gradient/high-curvature flows, Experiments in Fluids 41 (2006) 255–263.

[95] A. A. Boateng, Rotary Kilns: Transport Phenomena and Transport Processes, Elsevier, 2016.